SURFACE EXCHANGE OF ENERGY AND WATER BUDGETS IN

URBAN CANOPIES

Zhihua Wang

A DISSERTATION

PRESENTED TO THE FACULTY

OF PRINCETON UNIVERSITY

IN CANDIDACY FOR THE DEGREE

OF DOCTOR OF PHILOSOPHY

RECOMMENDED FOR ACCEPTANCE

BY THE DEPARTMENT OF

CIVIL AND ENVIRONMENTAL ENGINEERING

Advisers: Elie Bou-Zeid and James Smith

September 2011

Abstract

The world is undergoing a rapid urbanization process unprecedented in human history: more than half of the global population is now living in urban areas. The associated change of surface landuse types has imposed significant impacts and stresses on environmental systems, prominent examples including heat island formation, modification of the ecohydrological system and degradation of air and water quality. The last few decades have seen increasing efforts to capture and characterize the physics of flow and surface transport processes in the lower urban atmosphere, in order to provide solutions to many urban environmental problems. In this work, we developed a new set of parameterization schemes for surface exchange of energy and water in urban canopies. The new model features: (1) explicit resolution of sub-facet heterogeneity, (2) a spatially-analytical algorithm for computation of urban surface temperatures and soil fluxes, and (3) incorporation of hydrological models for both natural and engineered urban facets. In addition, we analyzed model sensitivity to uncertainties in the parameter space using advanced statistical simulations. Intensive field measurements have also been carried out through a large network of sensors deployed over the campus of Princeton University. Data collected from the sensor network are used to provide input parameters as well as to validate the new exchange schemes. The new model has been tested extensively under ideal and realistic case studies and was shown to be adequate in reproducing a large array of surface parameters, including skin temperatures, net radiation, turbulent fluxes and soil water content. The new model can also be readily extended for practical applications such as assessment of various mitigation strategies of urban heat islands.

Acknowledgement

First of all, I would like to thank my advisers Professor Elie Bou-Zeid and Professor James Smith, for giving me the opportunity to work in their motivating and enthusiastic groups. They encouraged me to work on the urban environmental problems and generously supported me for participating numerous conferences, workshops and other academic activities which greatly enlightened and enriched my research experience. This work would not be accomplished without their invaluable guidance and support.

I would also like to thank Prof. Maria Garlock, Prof. George Scherer, Prof. Jean Prévost, late Prof. Oliver Coussy, Prof. Sankaran Sundaresan, Dr. Mary Lynn Baeck, Dr. Scott Sanborn, Dr. Charles Talbot, and Dr. Gabriele Villarini for their help and advices at different stages of my Ph.D. work. I owed much gratitude to Dr. Ben Young and Dr. Kang-Hai Tan for their guidance to my embarking on research career and their continuous support through the path. I am also indebted to Dr. Siu-Kui Au, from whom I benefited tremendously through insightful discussions and fruitful collaborations.

The field experiments would not be successful without the help from staff members of Sensorscope, the manufacturers of the wireless sensor stations. I would like to thank François Ingelrest, Guillermo Barrenetxea and Davis Daidie for their technical assistance in station communication and data management.

My sincere thanks also go to all the administrative staff of the Department of Civil and Environmental Engineering at Princeton University including Jennifer Poacelli, Jane Soohoo, Linda Patel, Islam Elnaggar, Tiffany Sirois, Melinda Matlack, and Joseph

Vocaturo. Their help and support made my work in the department of CEE tremendously easier and more enjoyable.

My special thanks go to my family members and my friends, especially my wife Xin Wang. They encouraged me to persevere during the adversities and shared my happiness of every little success. Xin even helped me carry instruments to the field and set up many of the wireless stations around the campus. Getting through the winding road that leads me here would be unimaginable without their unreserved support.

Table of contents

List of Tables

List of Figures

The light dove cleaving in free air

whose resistance it feels

might imagine that her movement would be

far more free and rapid in airless space

– Immanuel Kant, *Critique of Pure Reason*

Chapter 1

Introduction

Urban areas, home to more than half of the world's population today, are humanity's engines of creativity, wealth production and economic growth. On the other hand, expansion of urban areas is associated with change of land cover, i.e. by replacing natural terrains with engineered materials (e.g. concrete, asphalt, brick, *etc.*), and intensive human activities. The induced "anthropogenic stressors" (Fernando, 2010) due to rapid urbanization, albeit a relatively new global issue, has emerged as sources of numerous adverse environmental impacts including urban heat island (UHI) formation, emissions of greenhouse gases and pollutions, and transmission of diseases.

Due to the continuous increase of urban surface fraction and its importance in modifying Earth's natural environment, there is an urgent need for integrated, quantitative, and predictive scientific tools to study the dynamics, growth and global sustainability of urban systems, together with its social and environmental impacts (Bettencourt and West, 2010). The last few decades have seen rapidly increasing research efforts in addressing urban environmental issues, ranging from local to global scales, that includes: urban meteorology and climatology (Arnfield, 2003; Kanda, 2007; Martilli, 2007), greenhouse gas induced urban warming (Grimmond, 2007; McCarthy *et al.*, 2010), urban water demand (House-Peters and Chang, 2011), urban ecohydrology (Pataki *et al.*, 2011) and global climate change (Kalnay and Cai, 2003).

It has been found that understanding and resolution of urban environmental problems is complicated by the tightly coupled relationship between human and natural system in urban areas (House-Peters and Chang, 2011) and is highly sensitive to further change of climate (Pataki *et al.*, 2011). Characterizing and capturing of urban land surface processes, such as transport of energy, water, trace gases and pollutants, is key to address these challenges,. Figure 1.1 shows main features of the urban canopy effect, i.e. effect of urbanization on land-atmosphere interactions, including: (1) anthropogenic stressors (sources of heat/moisture and emissions of pollutant/green house gases directly by human activities), (2) modified thermal properties due to usage of engineered materials and heating, ventilation and air conditioning (HVAC) systems, (3) modified flow and turbulence structures due to presence of buildings, and (4) radiative trapping inside street canyons. It has been proved that accurate parameterizations of urban surface exchange schemes can substantially improve the performance of mesoscale numerical models (Cuenca *et al.*, 1996; Masson, 2006; Baklanov *et al.*, 2008; Champollion *et al.*, 2009; Hamdi *et al.*, 2010; Flagg and Taylor, 2011).
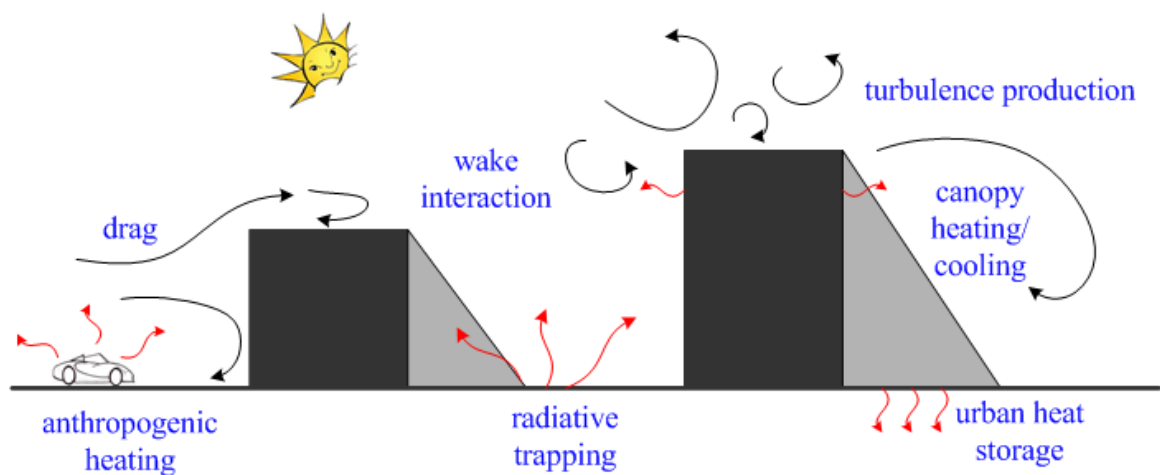
Figure 1.1: Schematic of the urban canopy effect on land-atmosphere interactions

The interaction between the atmosphere and urban land surfaces involves complex physics emanating from a wide range of scales and processes, such as the complexity of built terrains, the variability of the flow and turbulence fields, and the strong heterogeneity of the urban environment. Following Oke (1982), the energy balance equation inside the urban canopy layer is given by:

$$R_n + H_F = H + LE + G \tag{1.1}$$

where $R_n = S^\downarrow + L^\downarrow - S^\uparrow - L^\uparrow$ is the net radiation with S and L denoting shortwave and longwave radiative budgets respectively; downward and upward arrows denote the downwelling and upwelling components respectively; H, LE and G are the sensible, latent and storage (conductive) heat fluxes respectively; and H_F is the anthropogenic heat flux. Sources of anthropogenic heat include human metabolism, vehicles, HVAC systems in buildings, emissions from industry and power plants. Methods for estimating anthropogenic heat and moisture in the urban environment are far from mature and yet to be standardized (Sailor, 2011). In addition, it has been theoretically verified that as far as numerical modeling is concerned, the energy balance equation (1.1) at each urban facet is strictly observed (Wang and Bou-Zeid, 2011).

Classical approaches for coupling urban surfaces with climate models represent urban areas as "flat" surfaces with high roughness length and modified surface properties. These operational models do not explicitly resolve the urban geometry and are computationally inexpensive (Grimmond and Oke, 2002). However their applicability relies heavily on parameterization of the real physics occurring in urban canyons, including aerodynamic properties (roughness length and zero-plane displacement,

Grimmond and Oke, 1999), heat storage (Grimmond *et al.*, 1991; Roberts *et al.*, 2006), and effective albedos (Sailor and Fan, 2002; Fortuniak, 2008) which in turn depends on the specific site.

Alternatively, numerical models have been developed to directly resolve the physics of urban land surface processes, including direct numerical simulations (Coceal *et al.*, 2006), large eddy simulations (Bou-Zeid *et al.*, 2009) of urban areas and of flow and heat transport simulations over cube matrices (Niceno *et al.*, 2002), or Reynolds-averaged numerical simulations of similar problems (Defraeye *et al.*, 2010). At local scales, building-averaged models were also developed to study the urban surface energy budgets, the big "canyon" model (Nunez and Oke, 1977; Johnson *et al.*, 1991) being a prominent example. The gap between the mesoscale atmospheric models and microscale (building, neighborhood, and city scales) land surface models remained wide till the emergence of the physically-based urban canopy models (UCM) (e.g. Masson, 2000; Kusaka *et al.*, 2001; Martilli *et al.*, 2002).

1.1. Urban canopy models

In the last decade, numerous urban canopy models have been developed to simulate the surface energy transport or the flow dynamics in the lower urban atmosphere. Whereas direct simulations of urban land-atmosphere interaction are computationally costly, physically-based parameterization schemes gained popularity and became a new paradigm for modeling urban surface exchange processes. The reduced computational cost of UCM (compared to full flow-resolving models), while preserving the essential

physics, allows the coupling of land surface models to mesoscale meteorological models such as Weather Research and Forecasting (WRF). The complexity of energy transport and flow physics inside urban canopies is usually captured by representing the urban area as big "canyons" (Nunez and Oke, 1977; Johnson *et al.*, 1991; Oke *et al.,* 1991) in UCM. Existing urban canopy schemes can be broadly categorized into two main categories, i.e. the single-layer (Masson, 2000; Kusaka *et al.*, 2001; Lee and Park, 2008; Chen *at al.*, 2011) and the multi-layer schemes (Martilli *et al.,* 2002; Dupont *et al.*, 2004; Kondo *et al.*, 2005). The former group of UCM usually focuses on parameterization of surface energy budgets, whereas the latter ones attempt to also better represent the flow dynamics induced in urban canopies using a drag approach. Despite their apparent differences, these schemes share some common features in their constructions, including that (1) all schemes have separate energy budgets for urban facets (roofs, walls and ground surfaces), and (2) radiative trapping inside urban canyons is explicitly resolved. Comprehensive reviews of the development of urban canopy models in the last decade can be found in Masson (2006), Martilli (2007), Porson *et al.* (2009) and Grimmond *et al.* (2010; 2011).

1.1.1. Single and multi-layer UCM

The first and simplest single-layer UCM is the Town Energy Balance (TEB) model developed by Masson (2000). Since then, various versions of TEB model have emerged to improve the original schemes. Kusaka and co-workers (2001; 2004) developed a very similar UCM but with explicit treatment of canyon orientation, which was later incorporated into the WRF model and tested extensively by Chen *et al.* (2010).

Lee and Park (2008) and Lee (2011), on the other hand, included the presence of urban vegetation inside the street canyon, which participated and interacted with other urban facets and thus affected the energy balance in the urban canopy particularly the latent heat budget.
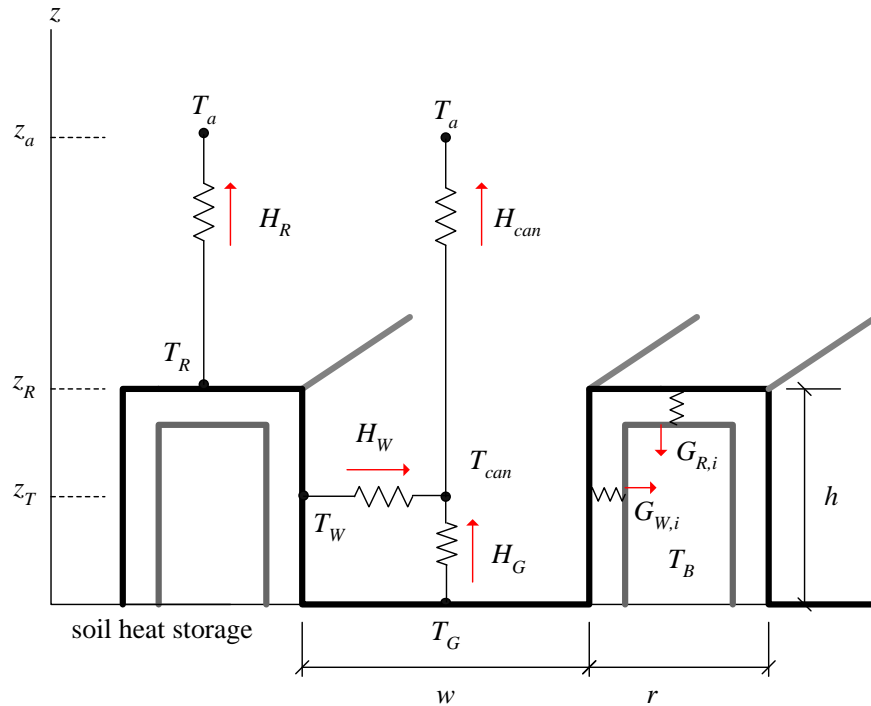
Figure 1.2: Schematic of the resistance network of energy transport in the single-layer urban canopy model: z_a is the reference height in the atmospheric layer; z_R is the height of the building; z_T is the representative height inside the street canyon; w, r and h denote the normalized canyon width, roof width and building height respectively

In the single-layer models, the exchange between the urban surface and the atmosphere only occurred at the canopy top. Inside the canyon, the canopy air is parameterized with representative canyon temperature and humidity, which are assumed to be uniform. Energy and water transport from walls and ground surfaces to the canyon

air are parameterized using an aerodynamic resistance network, as shown in Figure 1.2, where subscripts 'a', 'R', 'W', 'G' and 'can' represent the atmosphere, roof, wall, ground and canyon respectively throughout this dissertation. Also inside the canyon, the UCM computes surface temperatures averaged over the sunlit and the shaded fractions. Heat conduction through building enclosures (roofs and walls) is determined using an imposed interior building temperature T_B. An adiabatic boundary is assumed for heat conduction through ground surfaces at a sufficiently large depth. The UCM is driven by atmospheric forcing including air temperature, pressure, humidity, wind speed, and downwelling shortwave/longwave radiation, provided by direct measurements or by coupling to an atmospheric model. Logarithmic wind profile is assumed between the canyon top and the first layer of the atmospheric model, whereas it varies exponentially inside the canyon.

When urban canopy parameterizations are coupled to the mesoscale atmospheric models, it is necessary not only to resolve the transport of scalars (energy and water) from urban areas but also to include the momentum flux and the wind drag induced by building arrays (Harman and Belcher, 2006). Multi-layer urban canopy models make use of the drag approach (Brown and Williams, 1998) and explicitly resolve the dynamics and momentum fluxes arising from urban areas. These models are capable of capturing the turbulent flow in the canyon and in the roughness sublayer. The cost of these models is considerably higher than the single-layer models induced by the refinement of the vertical resolution and the direct interaction with the atmospheric layer. Martilli *et al.* (2002) presented detailed schemes of the multi-layer model, allowing variation in the building height. In their later versions, a building energy model (Salamanca *et al.*, 2010) and coupling to Reynolds-averaged numerical simulations (Santiago and Martilli, 2010)

were also included. Models of the same kind were also developed by Kondo *et al.* (2005) and Dupont and Mestayer (2006). In Kondo *et al.* (2005), representation of urban areas as rectangular building blocks instead of street canyons were adopted, whereas the urban parameterization schemes were coupled with soil models in Dupont and Mestayer (2006).

Besides the commonly used one-dimensional (1D) big canyon model for the representation of urban areas, two-dimensional (2D) rectangular building arrays have also adopted for urban configurations (Kanda *et al.*, 2005; Kondo *et al.* 2005). The alternative representation with added dimensionality is straightforward to implement, which mainly involves altering the urban area indices and the view factors for radiative trapping inside the canyon. As compared to field measurements in real cities, both representations have comparable model accuracy (Grimmond *et al.*, 2010; 2012). Thus the 1D canyon model is usually preferred due to its simplicity.

It is noteworthy that in all the existing UCM, each urban facet, be it the roof, the wall or the ground, is represented by a single homogenous surface (c.f. Figure 1.2) and only one set of surface parameters (e.g. surface albedo, emissivity, thermal conductivity, *etc*.) can be assigned. This over-simplifies the complex urban surface configurations, for example, in real urban areas, vegetation covers and impervious pavements are both commonly found ground surface types. In particular, Grimmond *et al*. (2011) recently reported that incorporation of vegetation cover in UCM has significant impact in model performance. Therefore it is essential to include sub-facet heterogeneity into the model construction.

1.1.2. Parameterization of heat storage and surface temperature

Among all the energy budgets in Eq. (1.1), parameterization of the heat storage term G is of particular importance to close the energy balance equation (Liebethal *et al.*, 2005; Foken 2008; Wang and Bou-Zeid, 2011). Computation of G is usually accomplished by solving the heat diffusion equations in the underlying soil formation. Over built surfaces, the solution of the heat conduction through solid media (walls, roofs, ground pavements, *etc.*) is further complicated by the high surface and thermal structure heterogeneity, including complex localized flow patterns inside street canyons (Bou-Zeid *et al.*, 2009), radiative trapping (Harman *et al.*, 2004), engineered materials (Yaghoobian *et al.*, 2010), as well as the anthropogenic heat releases (Taha, 1997).

Parameterization of heat storage for urban surfaces was first investigated by Doll *et al.* (1985) using the net radiation. With the complexity of urban surfaces and anthropogenic effects, the relation between the heat storage and net radiation exhibits a hysteresis loop, instead of direct proportionality, as reported by Oke and Cleugh (1987) and Grimmond *et al.* (1991). It is therefore sensitive to environmental conditions (Anandakumar, 1999). Recent developments in prediction of heat storage resorted to known surface temperatures, either by measurement (Wang and Bras, 1999) or by numerical modeling (Nunez *et al.*, 2010).

Explicit solutions of prognostic equations for surface temperature and subsurface heat flux, in practice, were not included in atmospheric models until 1970s. Some early predictive models attempted to parameterize the conductive heat flux as a (constant) fraction of the sensible heat flux (Kasahara and Washington, 1971) or the net radiative

flux (Nickerson and Smiley, 1975), and deduce the soil surface temperature. In these models, the details of conductive heat fluxes and subsurface temperature fields are ignored and surface temperatures are controlled by meteorological forcing in the atmospheric surface layer. Corby *et al.* (1972) proposed a parameterization of the subsurface flux to compute the surface temperature using the following prognostic equation:

$$\frac{\partial G}{\partial t} = \rho_s c_s \frac{\partial T_s}{\partial t} = -\pi^{1/2} \frac{H + LE - R_n}{d_1} \tag{1.2}$$

where ρ and c are the density and the specific heat respectively, T the temperature, $d_1 = \sqrt{\alpha_s \tau_1}$ the depth reached by the diurnal temperature cycle, τ_1 a period of 1 day and subscript 's' denotes the soil. The rate of heat storage change in Eq. (1.2) includes the soil heat capacity but conduction below the ground surface is neglected, i.e. the soil is assumed to be a lumped heat reservoir with a constant temperature equal to T_s. To improve upon this simplified model, Bhumralkar (1975) proposed a force-restore rate equation:

$$\frac{\partial T_s}{\partial t} = -2\pi^{1/2} \frac{H + LE - R_n}{\rho_s c_s d_1} - \frac{2\pi}{\tau_1} (T_s - T_2) \tag{1.3}$$

where T_2 is a deep soil temperature. Note that in Eq. (1.3), a restoring term was added in addition to the forcing term $H + LE - R_n$, incorporating the conduction into deep soil. A comprehensive review of the force-restore method can be found in Arya (2001).

It is noteworthy that the methods presented above involve first-order differential equations for surface temperature and are inevitably simplifications of the exact heat

diffusion equation. At best, these solutions converge to the finite difference solution of the second-order diffusion equation (Deardorff, 1978). Using the second-order diffusion equitation, Best (1998) developed a portable model for predicting surface temperatures for various surface types. Approaches for the determination of surface and sub-surface temperatures in built terrain based on three-dimensional energy balance models were also proposed (Krayenhoff and Voogt, 2007). All the existing urban canopy schemes (Masson, 2000; Kusaka *et al.*, 2001; Martilli *et al.*, 2002; Lee and Park, 2008; Chen *et al.*, 2011) solved the second-order heat diffusion equation for surface temperature and heat storage using fully (spatially and temporally) discrete numerical methods, usually the finite difference approach.

There are a few major disadvantages associated with the finite difference approach for the solution of the second order diffusion equation: (1) temperature and heat flux inside the solid media are discontinuous; (2) for complex solid formation with heterogeneous material properties, fine spatial discretization may be required to resolve the spatial temperature distribution (at least 6 layers, according to Deardorff, 1978), which is computationally expensive; (3) solid layers cannot be too thick for numerical solution to capture the temperature gradient, nor can they be too thin to prevent spurious oscillation of conductive heat flux (Roache, 1998); and (4) a finite domain has to be used for conduction in the semi-infinite ground soil, in which a zero flux (adiabatic) boundary condition needs to be assumed at a sufficiently deep level (which occurs at infinite depth, theoretically) .

On the other hand, analytical schemes for canonical problems of heat diffusion through solid layers have been derived and widely used (Carslaw and Jaeger, 1959).

Pioneering work has been done using the second law of thermodynamics (Strub *et al.*, 2005) to study periodic heat conduction through finite walls, albeit restricted to the Dirichlet problem (temperatures are specified at the boundaries). The disadvantage associated with fully discrete methods motivated us to develop an analytically tractable model under general problem setting of second order heat diffusion and apply to urban parameterizations (Wang *et al.*, 2011a).

1.2. Uncertainty and sensitivity analysis of UCM

From the comparison of UCM predictions against measurements in real cities, the performance of urban canopy parameterizations was found to depend largely on the accuracy in specifying input parameters (Grimmond *et al.*, 2011). Among the input parameters of the UCM, the atmospheric forcing, i.e. temperature, pressure, humidity, wind speed, and solar radiation, can be readily measured in the atmospheric surface layer or they could be provided by the atmospheric component of a coupled model (normally at the first grid node above the surface in a mesoscale model). In contrast, the surface parameters of the UCM (see Tables 2.1 and 2.2), including thermal properties of walls, roofs and ground soils, (normalized) dimensions of canyon geometry, and internal building temperatures, are rarely measured at urban scales. Although thermal properties can be selected for common engineered (concrete, asphalt, gravel, *etc.*) or natural (bare soils, grass, trees, *etc.*) materials and calibrated for a particular case study, these results are usually site-specific and limited in applicability (Hamdi and Schayes, 2007).

The uncertainty in the surface parameters of the UCM for any particular study is therefore ubiquitous and is the norm rather than the exception. This uncertainty can reduce the quality of the model output although these models realistically capture most of the physical processes occurring in urban areas. Grimmond *et al.* (2010; 2011), for example, in an intercomparison study featuring numerous UCM and several bulk schemes, did not observe any significant improvement in the performance when sophisticated models were compared rather than much simpler models. In contrast, they observed that the outcome of simpler UCM exhibited improvements with more input information, whereas the more complex ones did not (Grimmond *et al.*, 2011). While the community is, in general, expecting that more complex UCM will have more potential for future improvement, there is an urgent need to quantify the uncertainty in model input such that we can have a better understanding of the model physics. Moreover, with the increasing number of applications of UCM with various model complexities, it is critical to assess the model fitness for choice of appropriate parameterization schemes, by analyzing the model sensitivity (Loridan *et al.*, 2011).

Modeling of parameter uncertainty through error propagation analysis, stochastic methods or similar approaches is common in weather forecasting (Panofsky and Brier, 1958; Molders and Kramm, 2009) and environmental studies (Refsgaard *et al.*, 2007; Liu *et al.*, 2010). To evaluate the sensitivity of the surface exchange schemes using UCM, the conventional (and the most direct) approach would be setting up a "control" case with a set of base parameters. The sensitivity of the model prediction to an individual parameter is then investigated by changing the values of that particular parameter while keeping the remaining parameters fixed. This approach, when the number of uncertain parameters

13

gets large, becomes computationally expensive and statistically problematic. By fixing the parameter space but allowing one parameter to change at a time, the resulting statistical correlations between the uncertain parameters can be an artifact of the base scenario choices. Recently, Loridan *et al.* (2010) applied a more advanced statistical procedure to assess the skill of the offline WRF-UCM. Their analyses started with a default set of urban surface parameters. By calibrating the parameters for the UCM to reproduce targeted net radiation and turbulent heat budgets, model sensitivity to these uncertain parameters can also be evaluated. It is therefore a "local" sensitivity analysis, in the sense that uncertain parameters were fine-tuned to yield the optimal performance of the UCM as compared against measurement at specific sites, and the permissible variation of a specific parameter largely depends on tuning of the rest of the parameter space. A more general "global" sensitivity analysis is still needed, in the sense that the uncertain parameter space should cover the entire range of physically-possible values, weighted by density distribution functions and not limited to any specific urban morphology or climate (Wang *et al.*, 2011b).

1.3. Urban hydrological model

The performance of existing urban canopy schemes were generally good in reproducing surface temperatures and sensible heat budgets (Hamdi and Schayes, 2007; Lemonsu *et al.*, 2009; Grimmond *et al.*, 2010; 2012). However, they are inevitably inadequate in capturing the dynamics of the urban water budget and the latent heat due to the lack of urban hydrological models and the oversimplification of the representation of

hydrological processes (Grimmond *et al.*, 2010). While the importance of linking the transport of water and energy is increasingly recognized for urban studies (Berdient and Huber, 1992; Mitchell *et al.*, 2008), the modeling practice is still lagging behind, partially due to the complexity of the physics of water transport, particularly for unsaturated soils. Lee and Park (2008) and Lee (2011) proposed a model, in which vegetation (tall trees and grass) was incorporated into the UCM, but the hydrological model was relatively crude and their study lacked validation for water transport in soil.

An additional dimension of complexity in urban hydrological models is the characterization of the hydraulic properties of soils and vegetations in urban areas. Field and laboratory measurements of urban soil properties, such as those of lawns and parks, are rarely found in the literature. On the other hand, all hydrological models rely heavily on accurate characterization of soil properties such as water diffusivity and hydraulic conductivity, particularly for the unsaturated soils (Hanks, 1992; Chen and Dudhia, 2001; Loosvelt *et al.*, 2011). For example, evaporation from bare soil surfaces is more strongly influenced by the soil water content and subsoil physics than by atmospheric demand when the soils are unsaturated, which is very commonly the case (De Bruin and Holtslag, 1982; Schlunder, 1988; Chen *et al.*, 1996; Shokri *et al.*, 2008). Parameterization of urban vegetation further complicates numerical models, by introducing heterogeneous quantities such as roughness length and stomatal resistance (Niyogi and Raman, 1997; Vercauteren *et al.*, 2009). Sensitivity studies showed that accurate description of urban vegetation fraction is of great importance for model performance (Lee and Park, 2008; Loridan *et al.*, 2010).

Unlike its conventional counterparts (bare soils or vegetation), hydrological models for urban pavements should be capable of resolving the water-holding capacity of impervious media, which regulates the drainage and evaporation processes for the major fraction of urban surfaces (Yamanaka *et al.*, 1997; Andersen *et al.*, 1999; Hagishima *et al*., 2005; Borselli and Torri, 2010; Nakayama and Fujita, 2010; Abahri *et al.*, 2011). Therefore, urban hydrological models need to incorporate the unique feature of evaporation arising from surfaces with engineered materials. Despite the existence of numerous hydrological models for natural terrains, it remains a challenge to develop an adequate but relatively simple hydrological model for built terrains. The difficulty also lies with the coupling of a hydrological model with the energy transport model that captures all the essential physics of urban canopies.

This dissertation, which aims to address some of the open challenges outlined above, is organized as follows. Chapter 2 presents a spatially-analytical algorithm for heat condition in solid materials and its application to UCM for more accurate prediction of urban surface temperatures and soil heat fluxes (published in Wang *et al.*, 2011a). In Chapter 3, we discuss the model sensitivity to uncertainties inherent in input parameter space (published in Wang *et al.*, 2011b). This enables us to more efficiently calibrate the model parameters when it is set up for study of different urban areas. Chapter 4 contains a comprehensive description of the detailed parameterization schemes for coupled heat and moisture transport in urban canopies. The performance of the new UCM is validated against the field measurements obtained through the Sensor Network over Princeton (SNOP) project. Finally we discuss some of the important implication of the current work and outline a few challenges in the future development of the UCM in Chapter 5.

Chapter 2

Spatially-analytical scheme for heat conduction

As discussed in Chapter 1, current urban canopy schemes make use of fully discrete methods, usually the Forward-Time Central-Space (FTCS) finite difference scheme, for solving the 1D heat equation and computation of surface temperatures and conductive heat fluxes. In this chapter, we present a spatially-analytical scheme for soil temperature and conductive heat fluxes using the Green's function solution for the second order diffusion equation. The proposed method is incorporated into the offline version of the urban canopy model adopted in WRF (Chen *et al.*, 2011). The new UCM is then compared to the convectional discrete method in canonical test problems and in real-world cases, of varying complexity, where surface temperature data were collected in an urban canopy layer using a wireless sensor network.

2.1. Mathematical model

Heat conduction in dry and homogeneous solid media is governed by the second order diffusion equation

$$\rho c \frac{\partial T}{\partial t} = \nabla \cdot k \left(\nabla T \right) \qquad (2.1)$$

17

where k is the thermal conductivity. For materials with isotropic thermal conductivity, we have $\alpha \nabla^2 T = \partial T / \partial t$, where $\alpha = k / \rho c$ is the thermal diffusivity. With temporally discrete boundary conditions, e.g. field measured diurnal heating/cooling cycles, solutions of general initial-boundary value problem (IBVP) require numerical discretization schemes (at least in time). In the following sections, two solution methods are presented: one with full spatial and temporal discretization (the one typically used in existing UCM), and the other, which we propose here, with temporal discretization but with analytical spatial solutions.

2.1.1. Finite difference method

In current urban energy balance models (Masson, 2000; Kusaka *et al.*, 2001; Chen *et al.*, 2011), solid media (walls, roofs and ground soil) are divided into N discrete layers, each with a thickness d_j and a thermal conductivity k_j, $j = 1, 2, \ldots, N$. A schematic discrete model is shown in Figure 2.1(a). The effective (mean) thermal conductivity for computation of fluxes through layers j and $j + 1$ is

$$\bar{k}_{j,j+1} = \frac{d_j + d_{j+1}}{\left(d_j / k_j \right) + \left(d_{j+1} / k_{j+1} \right)} \qquad (2.2)$$

For wall, roof and ground, $j = 1$ is the layer of solid in contact with the ambient air. It is assumed that the first layer is thin enough such that the layer-averaged temperature is approximately equal to the surface temperature. The evolution of the surface temperatures is therefore computed as

$$c_1 \frac{\partial T_1}{\partial t} = \frac{1}{d_1}\left(R_n - H - LE - G_{1\to2}\right) \qquad (2.3)$$

where $G_{1\to2}$ is the conductive heat flux transferred from the 1st to the 2nd solid layer. The conductive heat flux between layers j and $j+1$ ($k < N$) is calculated in a layer-averaged temperature gradient sense, as

$$G_{j\to j+1} = \bar{k}_{j,j+1}\frac{2\left(T_j - T_{j+1}\right)}{d_j + d_{j+1}} \qquad (2.4)$$

Note that in Eq. (2.3), the surface temperatures are coupled to the net radiative exchanges and to the turbulent sensible and latent heat fluxes. As such, the solution of the heat fluxes in the solid layers and in the adjacent air layers are also coupled. Iterations are hence required to compute these temperatures. We perform these iterations in this study until the discrepancy between subsequent solutions of surface temperatures decreases below a specified relative tolerance, here defined as 10^{-4}.

Dirichlet conditions are used for the inner boundaries of the roof, wall and ground where the inner wall (or ceiling) temperature is set equal to the indoor temperature T_B. This is the standard treatment of the inner boundary condition by UCM users. As tested by Wang *et al.* (2005), the discrepancy caused by using Dirichlet boundary is insignificant as compared to using more complicated mixed (Robin) boundary condition. The various fluxes from the different parts of the building envelope are then computed following:

$$G_{R,N\to N+1} = k_{R,N}\frac{2\left(T_{R,N} - T_B\right)}{d_{R,N}} \qquad (2.5)$$

$$G_{W,N\to N+1} = k_{W,N} \frac{2\left(T_{W,N} - T_B\right)}{d_{W,N}} \qquad (2.6)$$

$$G_{G,N\to N+1} = 0 \qquad (2.7)$$

This formulation assumes the air inside the building to be a lumped mass with uniform temperature T_B, which is identical to the temperature of the inner walls.
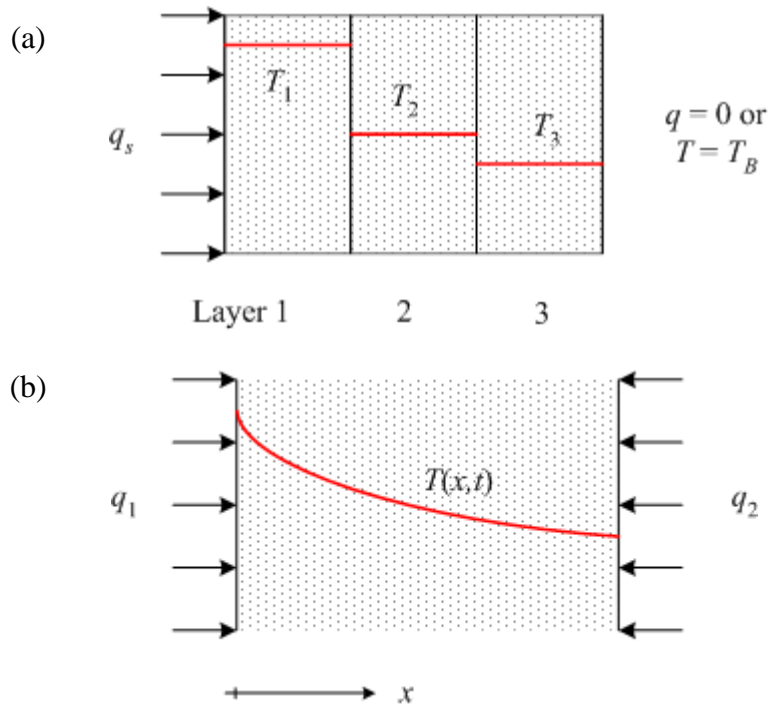
Figure 2.1: Schematics of heat conduction inside solid media: (a) discrete model and (b) continuous analytical model

2.1.2. Spatially-analytical model using Green's function approach

For 1D heat conduction through solid media, it is convenient to consider a model with continuous temperature variation in the domain $x \in [0, d]$, where d is the depth of

entire solid layer (see Figure 2.1(b), for the ground, $d_G \to \infty$). In a general setting of the

problem, the initial conditions are given by

$$T(x,0) = T_0 \qquad (2.8)$$

and the boundary conditions are given by the surface forcing (note that $x = 0$ corresponds

to the outer surface and $x = d$ to the inner surface)

$$-k\frac{\partial}{\partial x}T(0,t) = q_1(t); \quad -k\frac{\partial}{\partial x}T(d,t) = q_2(t) \qquad (2.9)$$
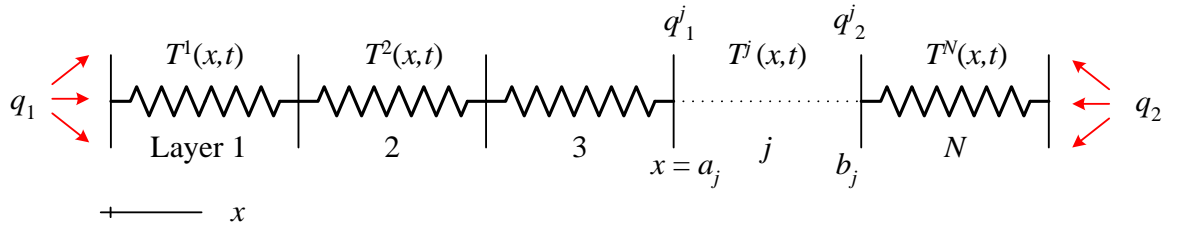
Figure 2.2: Heat conduction in composite solid media with multiple layers

We then consider the Green's function solution $g_i(x,t)$ to the following IBVP:

$$\alpha\nabla^2 g_i - \frac{\partial g_i}{\partial t} = 0; \qquad g_i(x,0) = 0; \qquad (2.10)$$

$$-k\frac{\partial}{\partial x}g_i(x_i,t) = H(t); \qquad -k\frac{\partial}{\partial x}g_i(d-x_i,t) = 0 \qquad (2.11)$$

where $H(t)$ is the Heaviside function, $i = 1$ or 2 is the boundary index corresponding to

$x = 0$ or $x = d$, respectively. As the diffusion operator is self-adjoint in x, the reciprocal

relation holds, i.e. $g_1(x,t) = -g_2(d-x,t)$. For a homogeneous solid layer, the general

solution of Eqs. (2.10) and (2.11) is given by the convolution (Stieltjes) integral (Carslaw and Jaeger, 1959)

$$T(x,t) = T_0 + \int_0^t q_1(t-\tau) dg_1(x,\tau) + \int_0^t q_2(t-\tau) dg_2(x,\tau) \qquad (2.12)$$

Accordingly, the conductive heat flux inside the solid layer is given by

$$G(x,t) = -k\frac{\partial T}{\partial x} = -k\left[\int_0^t q_1(t-\tau) dg_1'(x,\tau) + \int_0^t q_2(t-\tau) dg_2'(x,\tau)\right] \qquad (2.13)$$

where $g' = \partial g / \partial x$ is defined as the spatial derivative of Green's functions.

Now consider a more general case with a heterogeneous multi-layer solid medium, where each layer has different material thermal properties, as shown in Figure 2.2. For the j-th layer, $1 \le j \le N$, let $T^j(x,t)$ denote the temperature field within $a_j \le x \le b_j$, and $q_i^j(t), i = 1$ or 2 the interface index. At the interfaces between two layers, we have the contact conditions that temperatures and fluxes are continuous at the interfaces, i.e.

$$T^{j-1}(b_{j-1},t) = T^j(a_j,t) \qquad (2.14)$$

$$q_2^{j-1}(t) = q_1^j(t) \qquad (2.15)$$

Furthermore, we also have the generic mixed boundary conditions at the domain limits (outer and inner surfaces of the wall or roof),

$$-k^1\frac{\partial T^1(a_1,t)}{\partial x} + h^1\left[T^1(a_1,t) - T_a^1\right] = q_1^1(t) \qquad (2.16)$$

$$-k^N\frac{\partial T^N(b_N,t)}{\partial x} + h^N\left[T^N(b_1,t) - T_a^N\right] = q_2^N(t) \qquad (2.17)$$

where h is the convective coefficient between an interface and the adjacent fluid, $q_1^1(t)$ and $q_2^N(t)$ the prescribed heat fluxes at the outermost and innermost surfaces respectively, and T_a^1 and T_a^N the outdoor and indoor air temperature, respectively. Note that by setting $k = 0$, we recover the Dirichlet boundary conditions and by letting $h = 0$, we recover the Neumann boundary conditions.

For a solid medium consisting of N layers, we have $2(N+1) - 2 = 2N$ unknowns representing the surface and interfacial temperatures and fluxes (which are quantities of most interest). On the other hand, by applying Eq. (2.12) to both surfaces of each layer, there are in total $2N$ equations. Therefore, we have a closed system for heat conduction in a heterogeneous solid medium consisting of N layers in general. Note that since the boundary conditions are often available as discrete functions in time, or not necessarily readily integrable analytically, the time advancement of the system of equations is discretized and performed numerically.

2.1.3. Application to urban canopy model

For heat conduction through the roof and ground, temperature gradients can be very high, in particular near the outer and inner surfaces of the building envelope during summer daytime hours. Thus for spatially discrete schemes, the roof and ground have to be divided into fine layers near the surface, even for homogeneous materials, in order to capture the strong temperature gradients. The spatially-analytical method proposed here does not suffer from this numerical constraint since the spatial variation of the temperature is analytically tractable.
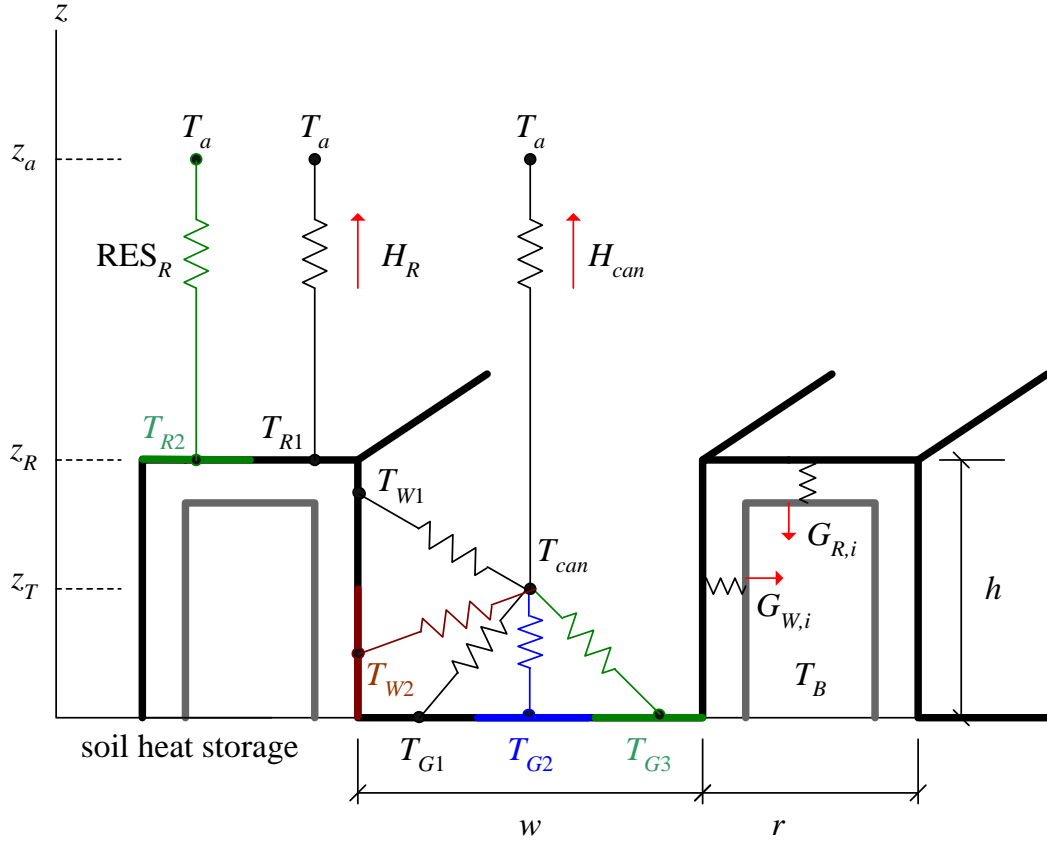
Figure 2.3: Schematic of the new UCM developed in this study, following the same symbols in Figure 1.2. Numeric subscripts denote numbering of heterogeneous sub-facets

Consider the urban canopy model shown in Figure 2.3. Here our new UCM adopts the infinite canyon representation for an urban area, same as the ones developed by Masson (2000) and Kusaka *et al.* (2001), and later implemented in WRF (Chen *et al.*, 2011). Note however as compared to Figure 1.2, that in the new model, each urban facet (the roof, the wall or the ground surface) is sub-divided into different types to incorporate the surface heterogeneity. For example, roofs can be a mixture of conventionally-paved roofs, or green roofs with planted vegetation, or other roof types; ground surfaces consist of different fractions of asphalt, concrete pavements, and lawns; wall materials can be

combination of brick or glass. Also note that this is the first UCM that explicitly represents sub-facet heterogeneity, thus allowing for example direct investigation of the fraction of green roofs on the UHI intensity. UCM with sub-facet heterogeneity also better simulates the energy transport in the urban canopy layer especially over low intensity built (suburban type) terrains that include a significant fraction of vegetated surfaces. In addition, the number of sub-facets is not fixed but rather flexible to include as many variations as possible for representing realistic urban surface configurations.

The Green's function solution of Eqs. (2.10) and (2.11) for a finite solid domain $0 \leq x \leq d$ with heat flux of unit strength at the surface can be obtained using the procedure called "method of image" (Courant and Hilbert, 1989)

$$g_1(x,t) = \frac{2(\alpha t / \pi)^{1/2}}{k} \sum_{n=-\infty}^{\infty} \exp\left[-\frac{(x-2nd)^2}{4\alpha t}\right] - \frac{1}{k} \sum_{n=-\infty}^{\infty} |x-2nd| \, \mathrm{erfc}\left[\frac{x}{2(\alpha t)^{1/2}}\right] \quad (2.18)$$

for small dimensionless time (Fourier number) $\bar{t} = \alpha t / d^2$, where $\mathrm{erfc}(\cdot)$ is the complementary error function. For large Fourier number, the following series solution can be obtained based on eigenfunction analysis (Cole *et al.*, 2011)

$$g_1(x,t) = \frac{\alpha t}{kd} + \frac{d}{6k}\left[3\left(1-\frac{x}{d}\right)^2 - 1\right] - \frac{2d}{\pi^2 k} \sum_{n=1}^{\infty} \frac{1}{n^2} \cos\left(\frac{n\pi x}{d}\right) \exp\left[-\alpha t \left(\frac{n\pi}{d}\right)^2\right] \quad (2.19)$$

Note that Eqs. (2.18) and (2.19) are different series representations of a unique solution. They become identical as the index of summation tends to infinity. The difference lies in that Eq. (2.18) converges more rapidly for small Fourier numbers, while Eq. (2.19) converges faster when the Fourier number is large (Wang *et al.*, 2005). It is therefore

desirable to apply them at different time, i.e. the so-called time partitioning method (Cole *et al.*, 2011), for rapid convergence of the series solutions.

As for conduction through the ground soil of the street canyon, the problem domain can be treated as semi-infinite $0 \leq x < \infty$, where the Green's function solution takes the simple form (Carslaw and Jaeger, 1959)

$$g_1(x,t) = \frac{2(\alpha t / \pi)^{1/2}}{k} \exp\left(-\frac{x^2}{4\alpha t}\right) - \frac{x}{k} \mathrm{erfc}\left[\frac{x}{2(\alpha t)^{1/2}}\right] \qquad (2.20)$$

The boundary conditions for conduction through walls, roofs and ground surfaces are:

$$-k_R \frac{\partial}{\partial x} T_R(0,t) = Q_R^*; \; -k_W \frac{\partial}{\partial x} T_W(0,t) = Q_W^*; \; -k_G \frac{\partial}{\partial x} T_G(0,t) = Q_G^* \qquad (2.21)$$

$$T_R(d_R,t) = T_B; \qquad T_W(d_W,t) = T_B; \qquad -k_G \frac{\partial}{\partial x} T_G(\infty,t) = 0 \qquad (2.22)$$

where $Q^* = R_n - H - LE$ is the heat flux input at the exterior surface. By substituting the Green's function solutions (2.18) to (2.20) into Eq. (2.12) and using the boundary conditions in Eqs. (2.21) and (2.22), the surface temperatures and fluxes of roofs, walls and canyon ground surfaces can be readily obtained using discrete numerical integration in time. The numerical procedure using the spatially-analytical method is outlined in Appendix A, to facilitate the implementation of the model by interested readers. More detail on the numerical procedures can be found in Wang *et al.* (2005).

2.2. Validation of the new algorithm

2.2.1. 1D solid plate subjected to sinusoidal flux

We first investigate an ideal case of a 1D homogeneous wall with one surface fixed at constant temperature (Dirichlet boundary at the interior of the wall) and the other surface exposed to an input of sinusoidal flux (Neumann boundary at the exterior of the wall). The initial/boundary conditions are

$$T(x,0) = T_0 \tag{2.23}$$

$$q_1 = -k \left.\frac{\partial T}{\partial x}\right|_{x=0} = A\cos\left(\frac{2\pi t}{t_d}\right) \tag{2.24}$$

$$T(d,t) = T_2 \tag{2.25}$$

where t_d is the period of the heating/cooling cycle. This ideal case closely mimics the scenario of a building wall with internal temperature-controlled space while the outer surface is subjected to a diurnal heating/cooling during a clear day. The parameters used in this example are: $d = 0.3$ m, $c = 1125$ J kg^{-1} K^{-1}, $\rho = 2400$ kg m^{-3}, $k = 1.2$ W m^{-1} K^{-1}, $A = -100$ W m^{-2}, $t_d = 1$ day and $T_0 = T_2 = 25$ ^{o}C. For the fully discrete model, the solid wall is divided uniformly into 3, 6 or 15 layers to investigate the effect of the sub-layer thickness on the accuracy of predictions.
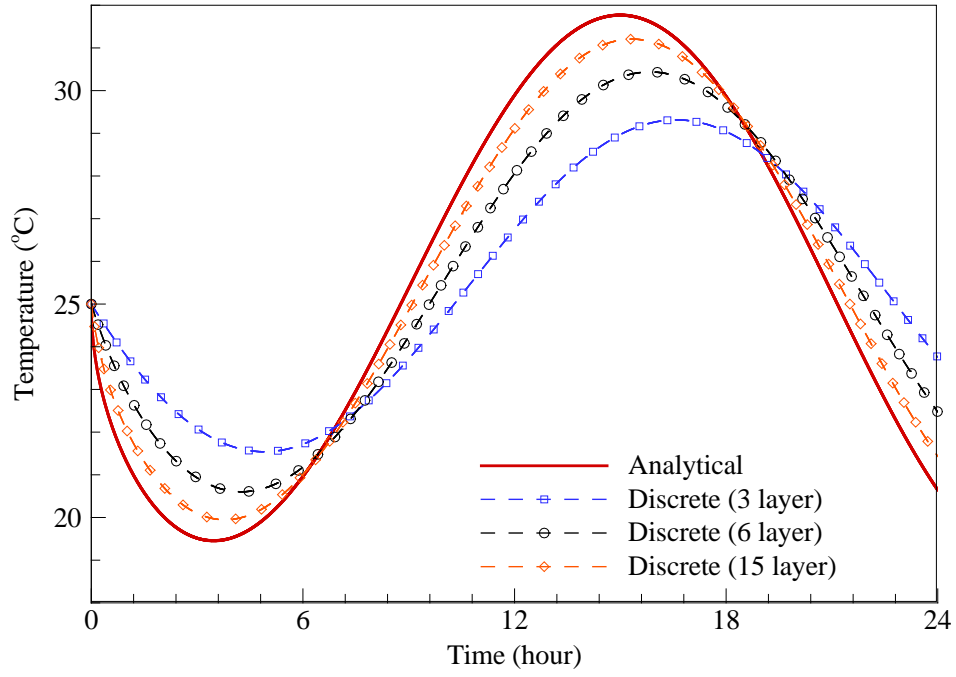
Figure 2.4: Surface temperature time history at the outer surface exposed to ambient flux
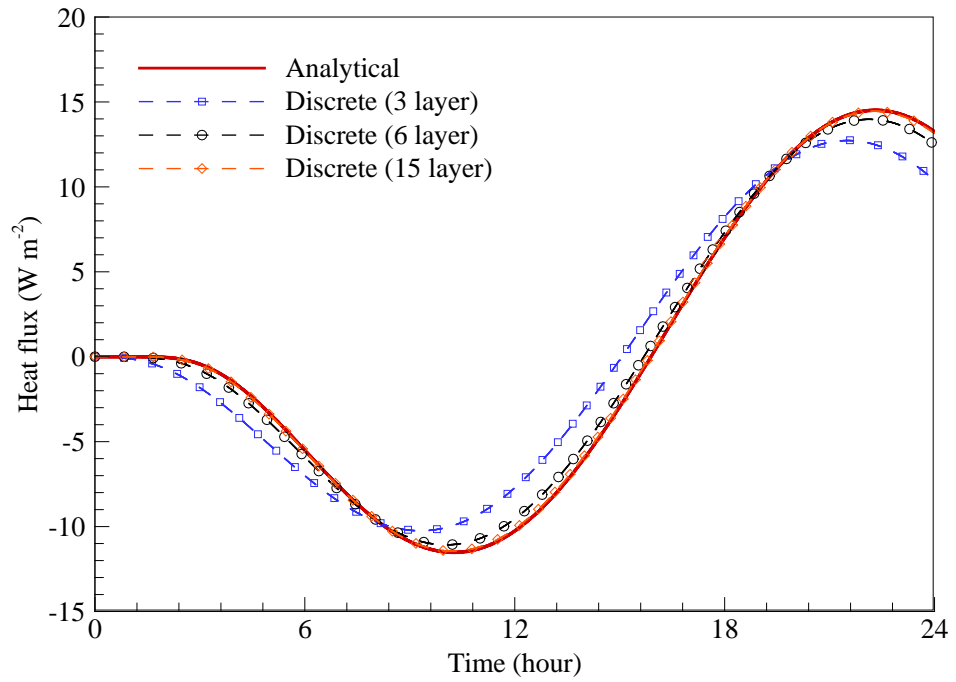
Figure 2.5: Flux time history at the inner surface with constant temperature
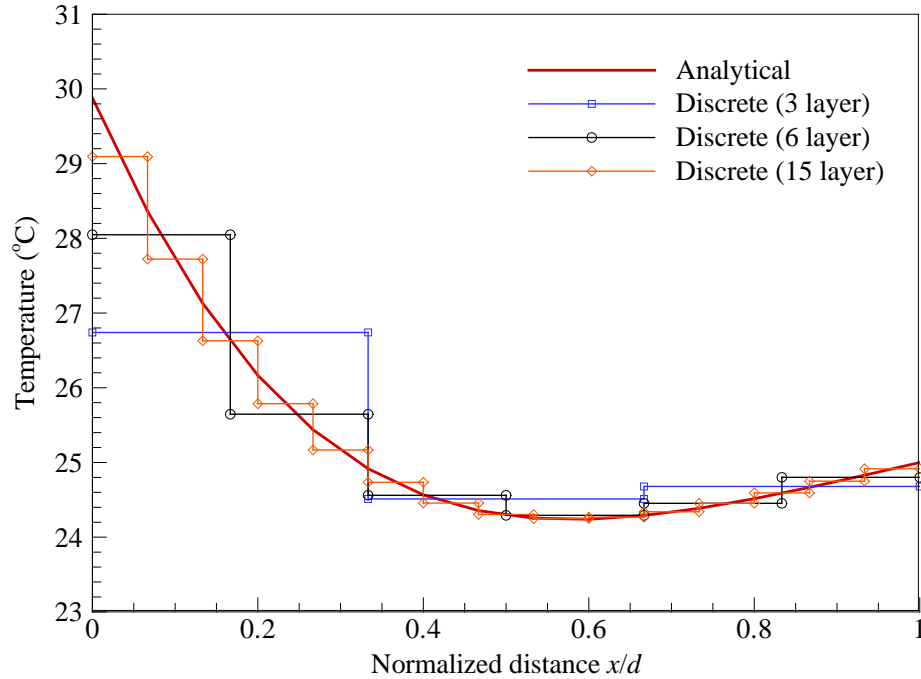
Figure 2.6: Temperature distribution inside the solid wall at time $t = t_d/2$

The time histories of the temperature at the Neumann boundary and the flux at the

Dirichlet boundary are shown in Figures 2.4 and 2.5 respectively. Note in Figure 2.5, the

conductive flux of the proposed method is computed exactly at the surface $x = d$, while

for the discrete model, the flux is calculated from layer $N - 1$ to N. Figure 2.6 illustrates

the spatial distribution (normalized by wall thickness d) of the temperature inside the wall

at noon ($t = t_d/2$). Clearly, as the number of sublayer increases, the numerical results

predicted by the discrete model asymptotically approaches the "exact" analytical

solutions. The 3 sublayer model clearly fails to capture both the spatial distribution and

the temporal evolution of temperatures and heat fluxes. On the other hand, the discrete

model with 15 sublayers can predict both flux evolution and spatial temperature

distribution with a reasonably good agreement compared the analytical model. However,

note that even with 15 layers we observe errors up to 0.8 °C in the outer surface

temperature (the maximum error is at that surface). This will have a significant impact on the actual heat exchanges between the building and the atmosphere. Moreover, recall that in the discrete model, the surface (skin) temperature of the solid medium is approximated using the layer-averaged temperature in the 1st layer adjacent to the exposed surface, it is clear from Figure 2.4 that the layer-averaged temperature has a persistent lag in response to the external forcing as compared to the true surface temperature given by the analytical solution, even with 15 sublayers. This is due to the presence of large temperature gradients near the surface exposed to the ambient forcing, as shown in Figure 2.6. The layer-averaged temperatures always have a phase lag in receiving the forcing signal from the surface.

While seemingly a finer spatial discretization tends to give more accurate prediction of the temperature and flux field, it is not always possible to divide the solid medium with finer sublayers without causing numerical difficulties. For FTCS finite difference scheme, the numerical stability requires that $s = \alpha \Delta t/(\Delta x)^2 \leq 0.5$. In this case, with $\alpha = 4.44 \times 10^{-7}$ m^2 s^{-1} and $\Delta t = 30$ s, a discrete model with 60 sublayers (or sublayers with thickness less than 5 mm) is unstable. This is also verified by numerical experiments: we observe wild spurious oscillation in numerical solutions using a fully discrete model with 60 sublayers (not shown here). Physically, this is due to the fact that the fully discrete model is not able to resolve finite temperature differences between two sublayers with infinitesimal distance. As a result, an excessively large virtual flux is induced due the temperature discontinuity at the interface of two sublayers. This numerical difficulty manifests itself particularly when high temperature gradients are encountered, i.e.

adjacent to a surface with a strong change in forcing signals. In contrast, the spatially-analytical model is unconditionally stable (Wang *et al.*, 2005).

2.2.2. A night cooling episode

In this section, the UCM is tested for a nocturnal cooling event in the Grand-view district of Vancouver, measured by Nunez and Oke (1976). The view factors between canyon facets are computed using street canyon dimensions. The thermal conductivities and heat capacities of the wall and the road are: $(\rho c)_{\text{wall}} = 10^6$ J K^{-1} m^{-3}, $k_{\text{wall}} = 0.81$ W m^{-1} K^{-1}, $(\rho c)_{\text{road}} = 1.94 \times 10^6$ J K^{-1} m^{-3}, $k_{\text{road}} = 1.01$ W m^{-1} K^{-1}. The initial downward radiative flux is $L^{\downarrow} = 339$ W m^{-2}. The short wave radiation, sensible and latent heat budgets are neglected in measurement and modelling. If these assumptions are valid, this would be a relatively easy case for the UCM; nevertheless, we are interested in this scenario since it has been simulated by many authors to test UCM performance (Johnson *et al.*, 1991; Masson 2000; Kusaka *et al.*, 2001).

Surface temperatures and the net longwave radiation predicted by the spatially-analytical method are compared with the measured data, shown in Figure 2.7. The surface temperature differences between the simulations and the measurements are less than 1 $^{\text{o}}$C. The net long wave radiation budget however is over-estimated for walls and slightly under-estimated for road, with a general discrepancy of about 10 W m^{-2}, or equivalent to 50% of the measurement value. The mixed results for the model performance are probably related to the various assumptions, particularly the neglect of sensible heat fluxes, rather than the inadequacy of the model *per se*. Runs with the fully discrete model

gave very similar results (not shown). The slowly varying heat fluxes and temperatures in this case are not particularly challenging for the discrete model.

(a)

(b)

(c)
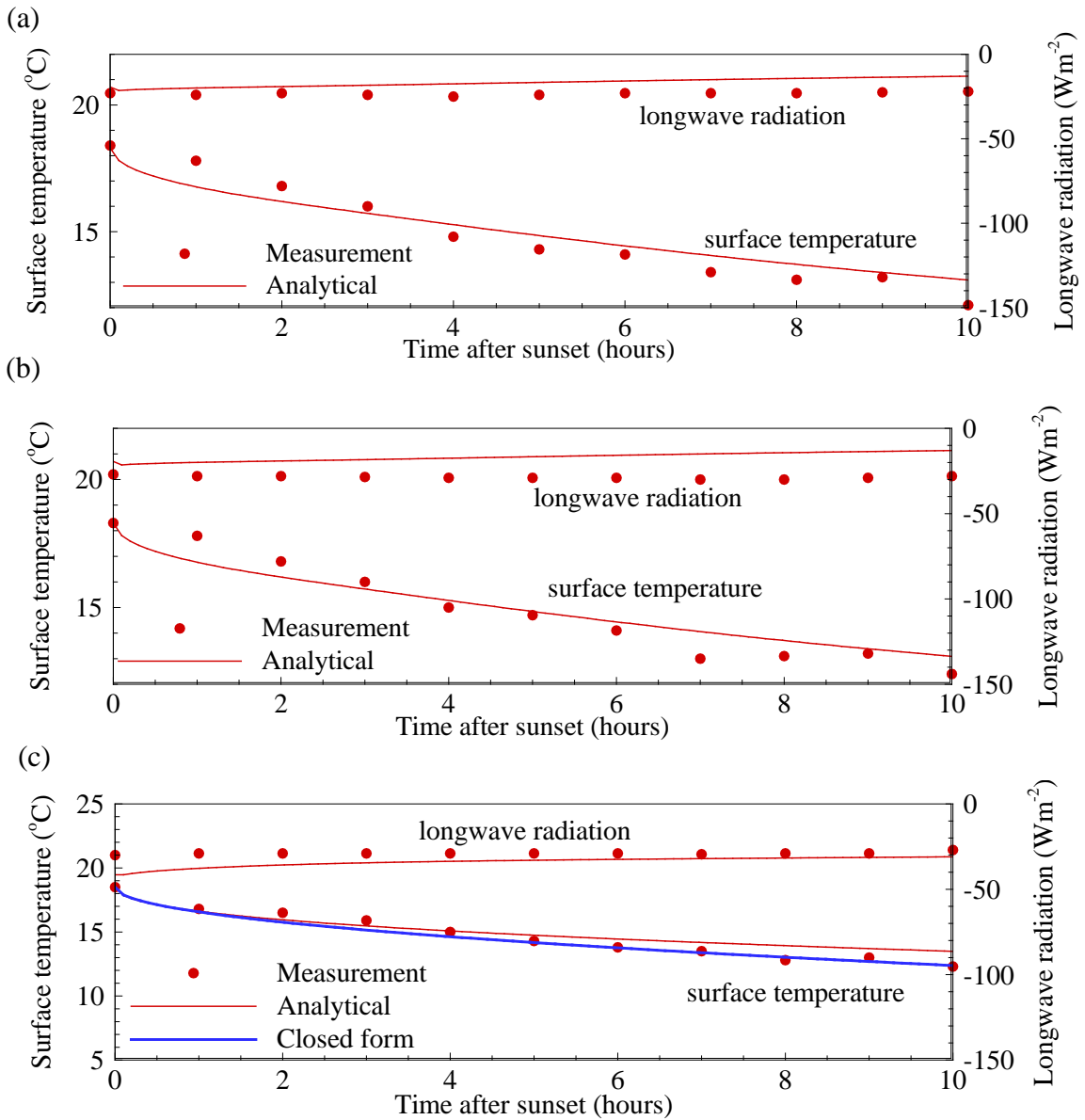
Figure 2.7: Comparison of predicted and measured surface temperatures and longwave radiation budget for (a) western wall, (b) eastern wall, and (c) road

Nevertheless, in this particular episode, we note that downwelling longwave radiation is roughly invariant with time and hence the surface fluxes do not have to be

imposed as temporally discrete boundary conditions. The convolution integral in Eq.

(2.12) can therefore be evaluated analytically without recourse to numerical integration in

time. For example, for semi-infinite ground soil, the temperature field can be written in a

closed-form, as

$$T_R\left(x,t\right) = T_{R,0} + L^{\downarrow}\left\{\frac{2\left(\alpha_R t / \pi\right)^{1/2}}{k_R}\exp\left(-\frac{x^2}{4\alpha_R t}\right) - \frac{x}{k_R}\operatorname{erfc}\left[\frac{x}{2\left(\alpha_R t\right)^{1/2}}\right]\right\} \quad (2.26)$$

In particular, at road surface $x = 0$, the skin temperature evolution is simply given by

$$T_{R,s}\left(t\right) = T_{R,0} + L^{\downarrow}\frac{2\left(\alpha_R t / \pi\right)^{1/2}}{k_R} \quad (2.27)$$

This closed form solution for road surface temperature prediction assuming constant $L^{\downarrow}$,

is also plotted in Figure 2.7(c). Note that it yields surface temperature profile with

reasonably good accuracy and the least computational cost. However, constant surface

heat fluxes that would allow the use of this closed form solution are the exception rather

than the rule and we recommend implementing and using the general form of the solution

with temporal discretization as described above.

2.2.3. Diurnal variation of surface temperatures

The analytical scheme (and its simplified forms in the specific cases) has thus far

been compared against the fully discrete model and validated against field measurements

in relatively simple settings where most of the components of the UCM are not used.

Here we further proceed to use the analytical model in the UCM to predict the diurnal

variation of the surface temperatures, measured using a network of wireless and conventional sensor nodes deployed over the campus of Princeton University under the Sensor Network Over Princeton (SNOP) project (Wang *et al.*, 2010).

The SNOP project includes various environmental sensing systems deployed over the Princeton campus. The sensing instruments of relevance in this study include: (1) a wireless network consisting of 11 sensorscope® stations (nodes) (see Nadeau *et al.*, 2009 for full description of the stations and for an application to the measurements of bulk heat fluxes over built terrain; the Princeton deployment is shown in Figure 2.8); and (2) a conventional eddy-covariance (EC) station deployed on the roof of a building. A typical sensorscope station includes: a cup anemometer (Davis) measuring wind velocity, a tipping bucket (Davis) collecting and measuring rain precipitation, a TNX infrared thermometer (ZyTemp) measuring air and surface temperatures, an EC-TM probe (Decagon) measuring volumetric water contents and temperatures of soil, and a solar radiation sensor (Davis). The EC station contains a Campbell Scientific three-dimensional sonic anemometer (CSAT3), an open path infrared gas analyzer (LI-7500 from Licor Biogeosciences), a temperature and relative humidity probe (HMP45C from Vaisala), an infrared surface temperature (IRR-P from Apogee instrument), a wind monitor (05305 R.M. Young from Campbell), and a 4-component radiometer (NR01 from Hukseflux). The EC measurements of sensible and latent heat fluxes are computed using an averaging time of 30 minutes, in which yaw and pitch angle corrections and the Webb correction are applied. The sonic anemometer is facing north-west to capture a footprint of heat and moisture sources from the downtown Princeton area.
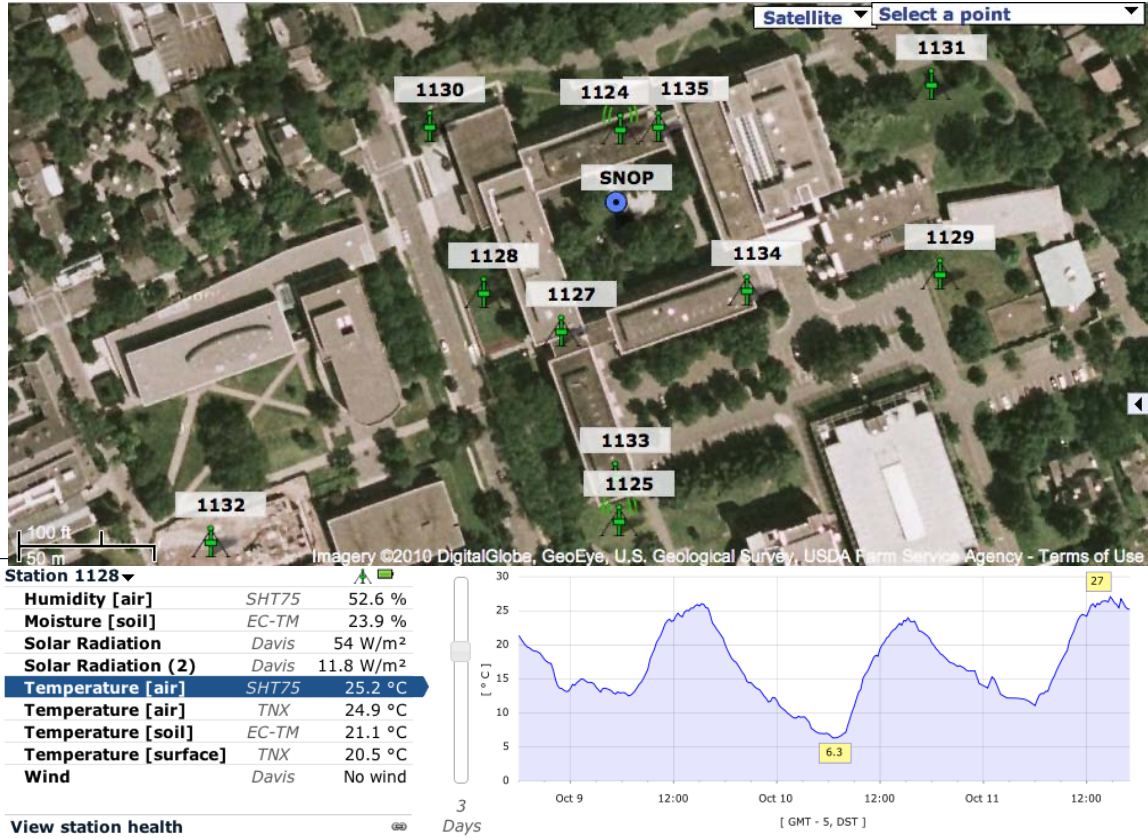
Figure 2.8: Deployment of the sensorscope stations over Princeton campus covering the study area. The lower part of the graph demonstrates the user interface for browsing the real time measurement data (see http://www.climaps.com)

The input surface and thermal parameters for the numerical model are listed in Tables 2.1 and 2.2, respectively. The surface parameters in Table 2.1 are carefully determined or estimated for the study area on the Princeton campus (Figure 2.8) and not tuned for model calibration. All thermal properties are assumed to be constant, with a reasonable range of values obtained from the literature (e.g. ASHRAE, 2009; Brutsaert, 2005). These parameters are then slightly tuned, within the realistic physical ranges expected for the building in the modelling domain, to optimize the model results. Model sensitivity to uncertainties in these surface parameters are assessed in the next chapter.
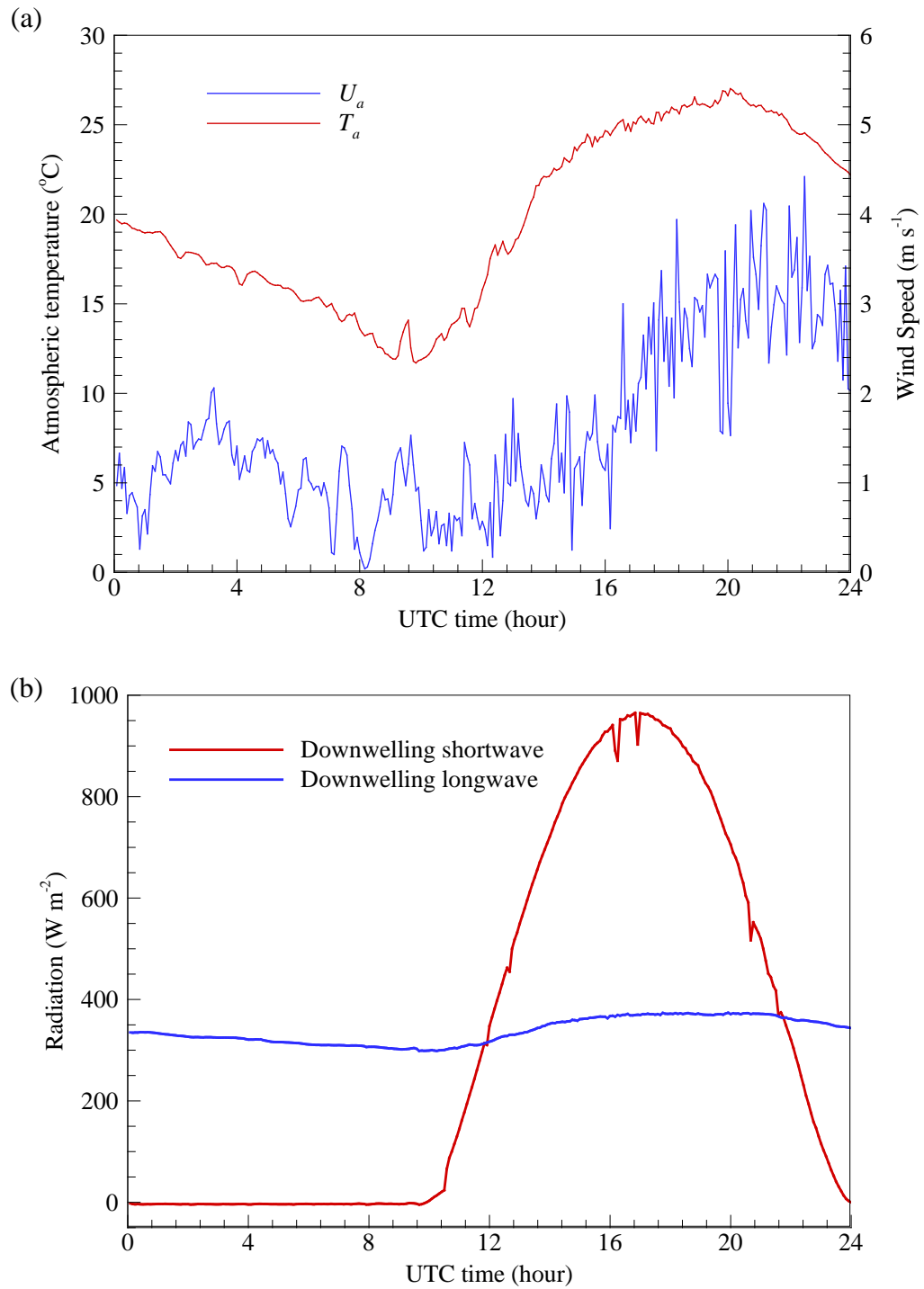
Figure 2.9: Atmospheric forcing from SNOP as input for the offline urban canopy model: (a) atmospheric temperature and wind speed; (b) downwelling radiation on 05 May 2010

The atmospheric forcing (representing air properties above the canopy) measured by the EC station during a diurnal cycle is plotted in Figure 2.9. The weather of the selected day (on 05 May 2010) is clear with low average winds (< 3 m s^{-1}). The footprint of temperature measurements by infrared thermometers is 1 m $\times 1$ m (maximum). Measurements of the conductive fluxes are not available through SNOP and are in general very difficult to perform. As such, we will focus on the comparison of the surface temperatures between the model and the experiment; this is a very good proxy that should give us insight into the model's performance.

Table 2.1: Input canyon dimension and surface parameters

Parameter	Symbol	Value
Roof level (building height) (m)	z_R	18.9
Reference height (m)	z_a	23.23
Normalized building height (-)	h	0.3
Normalized roof width (-)	r	0.4
Normalized road width (-)	w	0.6
Thickness of roof (m)	d_R	0.5
Thickness of wall (m)	d_W	0.3
Fraction of asphalt pavement on ground (-)	f_{asp}	0.5
Fraction of concrete pavement on ground (-)	f_{con}	0.2
Fraction of vegetation on ground (-)	f_{veg}	0.3
Roughness length for momentum above roof (m)	$z_{m,R}$	0.01
Roughness length for heat above roof (m)	$z_{h,R}$	0.001
Roughness length of momentum above canyon (m)	$z_{m,can}$	0.05
Roughness length of heat above canyon (m)	$z_{h,can}$	0.005
Street canyon orientation (rad)	θ_{can}	$\pi/4$
Latitude (positive North) (rad)	ϕ	0.7043
Longitude(positive West) (rad)	λ	1.3029

Table 2.2: Input material thermal/hydraulic properties

Parameter	Symbol	Value
Roof surface albedo	a_R	0.30
Wall surface albedo	a_W	0.25
Albedo of asphalt, concrete, vegetated (A,C,V) ground	a_G	0.15; 0.40; 0.15
Roof surface emissivity	ε_R	0.95
Wall surface emissivity	ε_W	0.95
Emissivity of (A,C,V) ground	ε_G	0.95; 0.98; 0.93
Thermal conductivity of roof (W K^{-1} m^{-1})	k_R	1.00
Thermal conductivity of wall (W K^{-1} m^{-1})	k_W	1.30
Thermal conductivity of (A,C,V) ground (W K^{-1} m^{-1})	k_G	1.20; 1.80; 2.00
Heat capacity of roof (MJ K^{-1} m^{-3})	C_R	2.00
Heat capacity of wall (MJ K^{-1} m^{-3})	C_W	1.20
Heat capacity of (A,C,V) ground (MJ K^{-1} m^{-3})	C_G	1.00; 2.40; 1.30
Volumetric water content at saturation (m^3 m^{-3})	θ_s	0.47
Saturation soil suction (m)	ψ_s	0.355
Fitting exponent for unsaturated soil (-)	b	5.33
Hydraulic conductivity at saturation (m s^{-1})	K_s	3.38E-06
Reference soil water content (m^3 m^{-3})	θ_r	0.15
Porosity of roof gravel (-)	ϕ_{eng}	0.3

A comparison of the roof temperature between the proposed model, the fully discrete model and the measurement is shown in Figure 2.10. The discrepancy between the proposed model prediction and the measurements is comparable to the discrepancy between the two measurements. Since the UCM represents the urban surface in an average sense, the comparison of model output to single-point measurements will be inconclusive due to the expected spatial variability of the real surface temperature fields (due for example to hot/cool spot induced by surface inhomogeneity, shading, *etc*.). To

overcome this possible shortcoming, the surface temperature measurements should be conducted at multiple points and the average value compared to the UCM simulations.
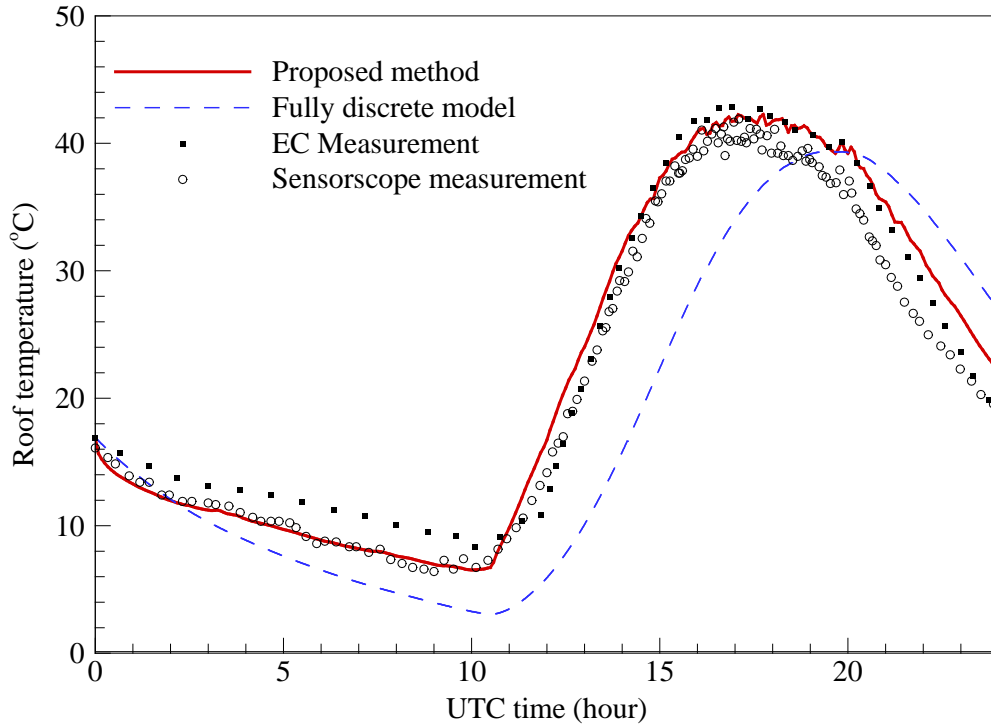
Figure 2.10: Comparison of model predictions and field measurement (EC station and sensorscope station 1124) of roof surface temperature

Measurements of ground surface temperature are available for three types of ground surfaces through SNOP, namely asphalt, concrete and vegetated surfaces. In this particular case, the vegetated surface refers to the short grass field that is most commonly found and dominant in the study area. We compared the diurnal variation of the surface temperature for all three types of surfaces (Figure 2.11(a)). In general, the rate of measured temperature change is larger than that of the prediction at night. During daytime, the largest temperature differences are caused by the shading effect at the measurement locations. The location of measurement of asphalt temperature is shaded in

the late afternoon (after 21:32 UTC) while the measurement point for concrete is shaded during the morning (before 13:40 UTC). Therefore there is a noticeable delay in the rise of the measured concrete surface temperature during the morning, while there is a rapid drop in asphalt temperature before sunset. Around noon, when both locations are not shaded, the model predicts the peak temperature quite accurately. As for the vegetated surface, we have in total four sensorscope stations (1125, 1128, 1131 and 1132) measuring the surface temperature. By averaging over experimental data over four different locations, the measurement incorporates the sunlit/shading effect in a similar (averaged) manner to the UCM and is more representative of real canyon ground. Consequently, as shown in Figure 2.11(a), the model prediction and the measurement data for the vegetated surface is in good agreement. These observations clearly suggest that for ground (as well as for wall) temperature, it is important to conduct the measurement at multiple (at least 2, one to each side of the canyon) points, in order to take into account the shading effect inside the canyon. Note that the model predicts the surface temperature in an average sense in terms of energy balance and radiation: shading of the surfaces inside the canyon is taken into account and the model prediction is the average of the shaded and sunlit areas for each surface type.

Model predictions using the fully discrete approach, with identical set of input parameters and 8 sublayers, are also plotted (Figure 2.10 and 2.11(b)). Temperature predictions in these cases, exhibit a phase lag compared to both the proposed method and the measurement. The phase lag is most significant for the prediction of the vegetated surface temperature. The existence of phase lag is consistent with the simple case study in Figure 2.4, and decreases as the spatial discretization gets finer (but never completely

disappears). Moreover, the discrete model underestimates the magnitude of the surface temperature, particularly the peaks of the diurnal variation.

Due to the strong coupling between surface temperatures and heat budgets (longwave radiation, turbulent and conductive heat fluxes), a finer spatial discretization does not necessarily improve the surface temperature prediction. For example, a 15-layer discrete model further underestimates the surface (all types) temperature before sunrise (not shown here). This could be due to the use of stability functions (Mascart *et al.*, 1995) that significantly reduce turbulent heat transfer before sunrise (in the stable surface layer), which makes large surface temperature differences between the atmosphere and the urban surfaces sustainable.

It could be argued that the material thermal properties can be adjusted to reduce the phase lag between the discrete model and the measurement, by reducing the heat capacities of roof and ground surfaces (the correlation and sensitivity of UCM to input parameters is being investigated in a separate study using stochastic method). Similarly, the temperature values could be improved by decreasing the thermal conductivities. However, as demonstrated in Section 2.2.1, for an ideal 1D heat transfer model, using the same set of thermal parameter, the solution using the fully discrete model should converge to the one using the proposed semi-analytical model with finer discretization. As for this case study, the discrepancy in the fully discrete model underlines an inherent weakness in the discrete model coupled into the UCM, for prediction of complicated scenarios (diurnal variation of urban surface temperatures). Uncertainties in parameter space, such as in material thermal properties, nevertheless amount to an important potential source of error in numerical predictions (see e.g. Loridan *et al.*, 2010).
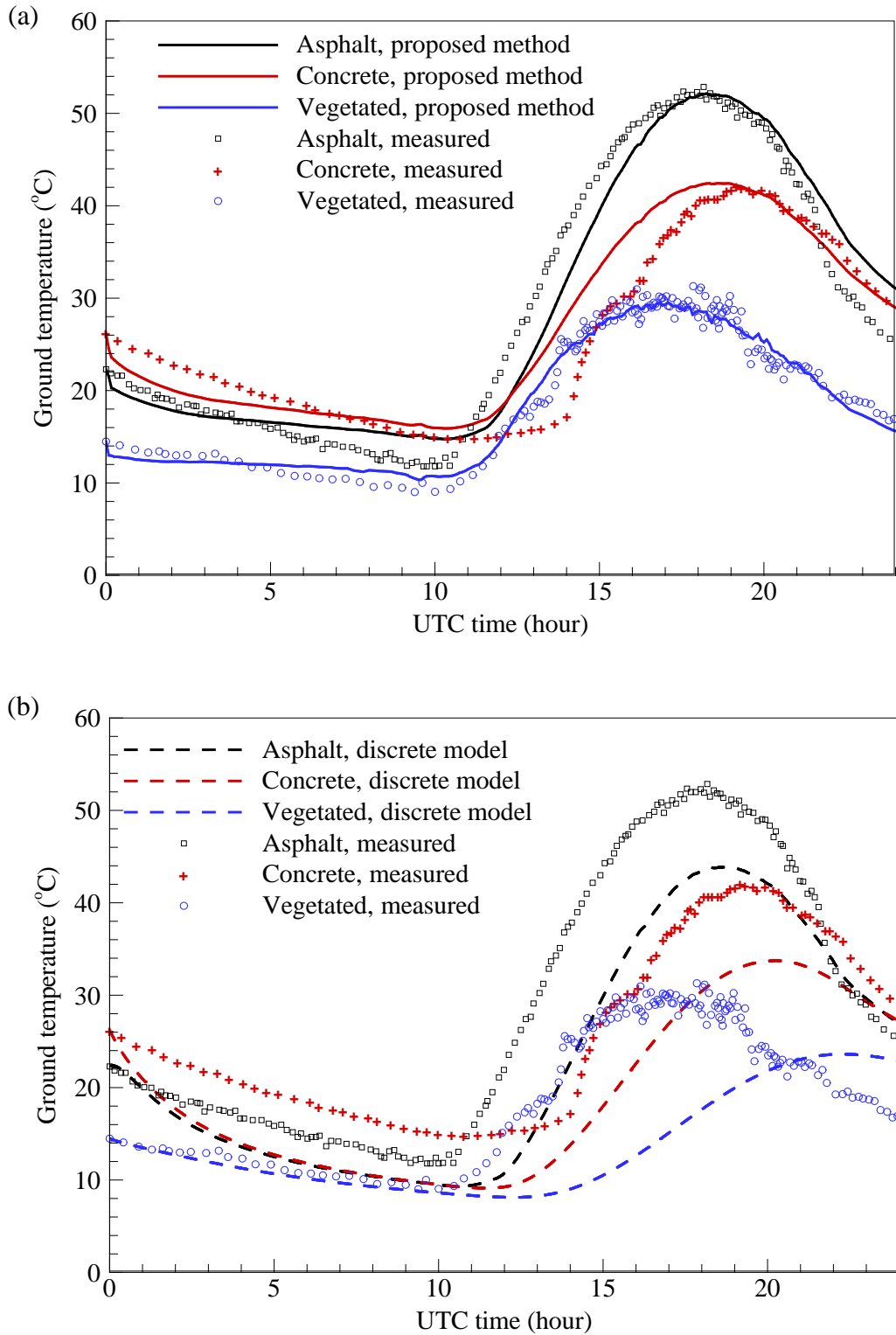
Figure 2.11: Comparison of ground surface temperature predicted by (a) the proposed

model and (b) the fully discrete model against measurements

In general, with all the simplifications in surface parameters and inherent uncertainty of turbulent parameterization in urban canopy models, the spatially-analytical scheme presented in this chapter is capable of predicting the evolution of the diurnal surface temperatures with reasonable accuracy. It is numerically inexpensive and more accurate as compared to the discrete model used in current UCM. Moreover, the temperature and the conductive heat flux fields inside the soil are analytically tractable, which provides better insight into the energy exchange process in the solid media.

2.3. Concluding remarks

In this chapter, we presented a spatially-analytical scheme for the evaluation of soil temperatures and conductive heat fluxes. The analytical scheme uses Green's function solutions of the diffusion equation, and is applicable to IBVP in general settings (i.e. non-homogenous mixed-type boundary conditions, finite, infinite, semi-finite problem domains, *etc*.). Time advancement is discretized since boundary conditions are usually available as discrete time series from model outputs or measurements. The new scheme is computationally inexpensive and overcomes numerical difficulties inherent in the fully discrete model. We also incorporate the analytical solution in the single-layer WRF-UCM, with sub-facet heterogeneity. The new UCM can then be used to predict the time evolution of the land surface parameters such as surface temperatures, conductive fluxes, turbulent heat fluxes, and radiative heat budget. Numerical predictions of the proposed method are compared to the conventional finite difference schemes currently used in all other urban canopy schemes and validated against the field measurements. The

results illustrate that the fully discrete schemes can have large errors that the semi-analytical scheme proposed here can successfully reduce or avoid. The comparison to field measurements from the SNOP in a low density urban canopy demonstrates that the new UCM with the proposed analytical algorithm is capable of predicting the surface parameters with good accuracy.

Chapter 3

Sensitivity analysis using advanced Monte Carlo simulation

In this chapter, we use an advanced Monte Carlo simulation tool, Subset Simulation (Au and Beck, 2001), to perform a sensitivity analysis for the uncertainties inherent in the surface parameters in offline WRF-UCM. Subset Simulation was originally developed to solve dynamic problems involving input stochastic processes and later found its applications in a broad range of engineering problems. This method is computationally efficient compared to the direct Monte Carlo method, particularly in investigating small probability events. Model sensitivity and characterization of individual surface parameters of the UCM are evaluated using the conditional samples generated in the Subset Simulation.

3.1. Subset Simulation

In the context of urban environmental study, the capability of assessing critical responses to the anthropogenic stressors is of paramount practical importance, e.g. extreme high urban center temperatures in summers, "hot spots" of surface sensible heat seen from the atmosphere, local concentration of pollutant and high frequency/intensity of local precipitation. Subset Simulation is an adaptive stochastic simulation procedure,

particularly efficient in capturing small tail probabilities (but very well adapted to long tail probabilities as well) associated with critical events (Au and Beck, 2001). It stems from the idea that a small exceedance probability can be expressed as a product of larger conditional exceedance probabilities for some intermediate exceedance events, thereby converting a rare event simulation problem into a sequence of more frequent ones. Here the exceedance probability $P(Y > y)$ is defined as the probability of a critical response Y (in our case for example surface temperature) exceeding a threshold value y.

During a simulation, conditional samples are generated from specially designed Markov chains so that they populate each intermediate exceedance region. The procedure illustrated in the schematic in Figure 3.1, is the following. At the initial phase (level 0), the choice of uncertainty parameters follows the prescribed probability distribution function (PDF), same as in the direct Monte Carlo method (Figure 3.1(a)). At the end of the initial stage, the first conditional level, defined as F_1 at which $P(Y > y_1)$, is determined in terms of a given conditional probability p_0 (Figure 3.1(b)). Conditional samples in the first level are then generated using the Markov Chain Monte Carlo (MCMC) procedure (Figure 3.1(c)) based on the parameter values that caused exceedance of y_1 in the initial stage simulations. The subsequent conditional levels are determined as exceedance events F_i at which $P(Y > y_i) = p_0^i$, $i = 1, 2, 3, ...$ respectively, and the algorithm continues until simulations reach the final target (rare) exceedance region (Figure 3.1(d)). Subset Simulation is robust, particularly for uncertain parameter space with high dimensionality, i.e. for problems with a large number of uncertain parameters.
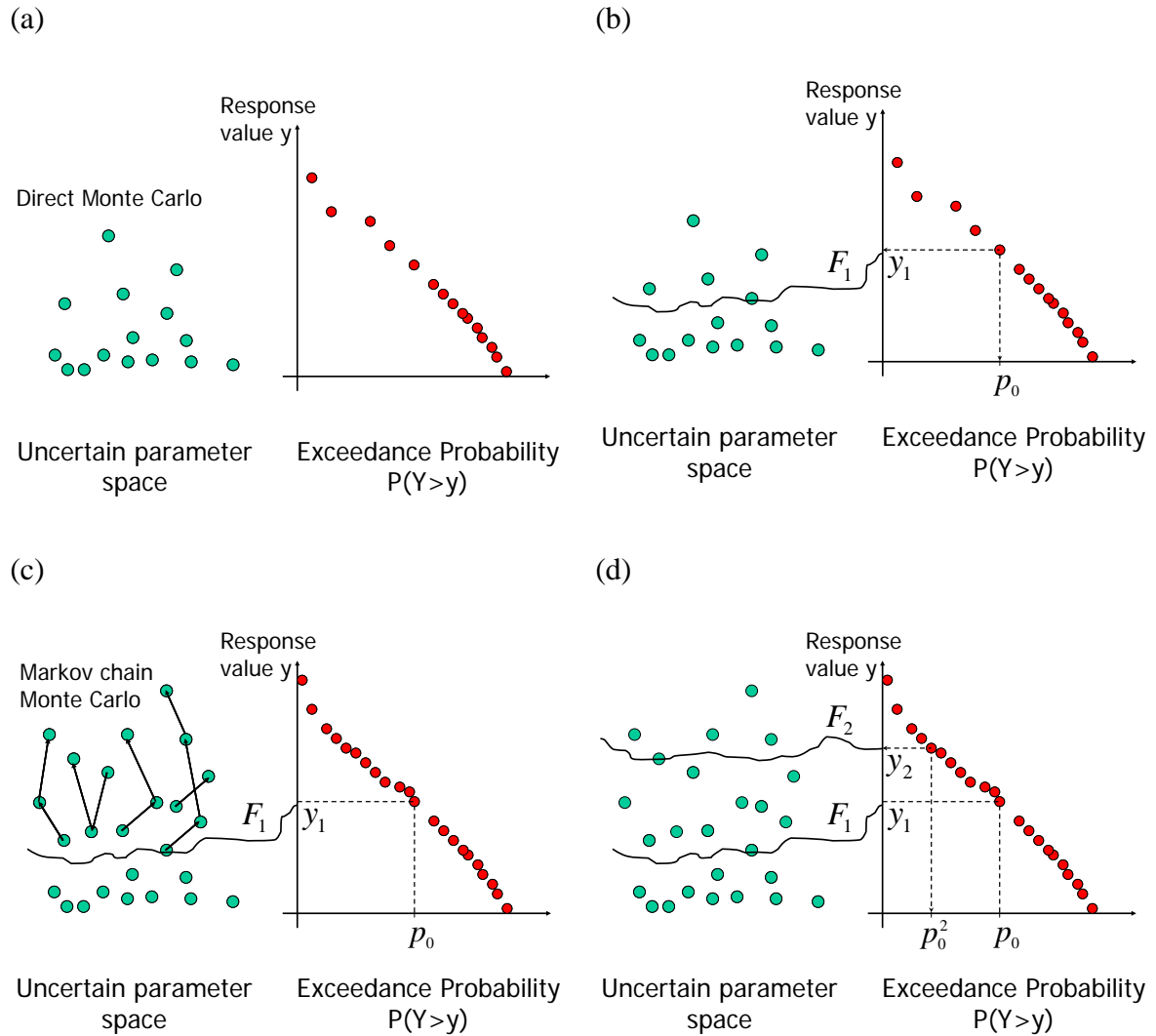
Figure 3.1: Schematic diagram of Subset Simulation procedure depicting: (a) level 0 (initial phase) direct Monte Carlo simulation; (b) determination of the first conditional level F_1 given conditional exceedance probability p_0; (c) populating conditional samples in the 1st conditional level by Markov Chain Monte Carlo procedure; and (d) forwarding algorithm to subsequent conditional levels

The efficient generation of conditional samples is highly-nontrivial but pivotal to the success of Subset Simulation. It is made possible through the machinery of a class of powerful Metropolis algorithms (Metropolis *et al.*, 1953; Hastings, 1970; Roberts and

Casella, 1999) on which the MCMC procedure is based. In MCMC, successive samples are generated from a specially designed Markov chain whose limiting stationary distribution tends to the target PDF as the length of the Markov chain increases. An essential aspect of the implementation of MCMC is the choice of the 'proposal distribution' which governs the generation of the next sample from the current one and consequently the efficiency of the algorithm. For application robustness, it is desirable to automate the choice of proposal distribution, at the expense of giving up possible gains in efficiency. For this purpose, it is found from previous experience that a *normal* distribution or a *uniform* distribution centered at the current sample gives reasonable accuracy (Au *et al.*, 2007; Molders and Kramm, 2009). These two classes of PDFs are therefore used in this study to enhance the statistical efficiency of Subset Simulations: normal distributions for surface thermal properties and uniform distributions for morphological surface parameters.

The UCM used in this study (c.f. Figure 2.3) is set up such that only evaporation from vegetated surfaces is considered here. The latent heat flux arising from a vegetated surface is parameterized using the actual evaporation given by

$$LE = C_e L_v E_e \qquad (3.1)$$

where L_v is the heat of evaporation, E_e the equilibrium evaporation rate, and $C_e = \alpha_e \beta_e$, with α_e the amplifying constant (on the order of 1.20-1.30) due to large-scale advection and β_e a reduction factor reflecting moisture availability. Depending on environmental conditions, C_e can vary from 0 (dry) to 1.26 (fully saturated) (Brutsaert, 2005). The equilibrium evaporation is calculated using the resistance method, as

$$E_e = \frac{\rho_a \left(q_s^* - q_a \right)}{\text{RES}_G} \qquad (3.2)$$

where RES is the aerodynamic resistance, q_a the specific humidity of the air, and q_s^* the saturated surface specific humidity computed using Clapeyron equation. We define the total sensible and latent heat fluxes over the urban area as:

$$H_u = rH_R + wH_{can} \qquad (3.3)$$

$$LE_u = rLE_R + wLE_{can} \qquad (3.4)$$

where subscript 'u' represent the entire urban area.

As a practical example, we run a typical Subset Simulation with the critical sensible heat flux H_u monitored as the model response, using a set of uncertain parameters in Table 3.1. In this study, we use 4 conditional levels and a conditional probability of $p_0 = 0.1$: this means that at each level simulations yielding the highest 10 percent of the monitored output values are considered to exceed the intermediate threshold. In Figure 3.2, the threshold values of the sensible heat H_u, corresponding to the exceedance probability of 10^{-1}, 10^{-2}, 10^{-3} at conditional levels 1, 2, and 3 are 183, 228 and 259 W m^{-2} respectively (these values are reflected in Figure 3.3 with $C_e = 0.6$ and will be discussed in the following Section). Typical histograms of conditional samples of uncertainty parameters, at different exceedance probability levels extracted from a typical simulation, are plotted in Figure 3.2. The distribution of the conditional samples at different levels is used to determine the sensitivity of the model to each individual uncertain parameter.
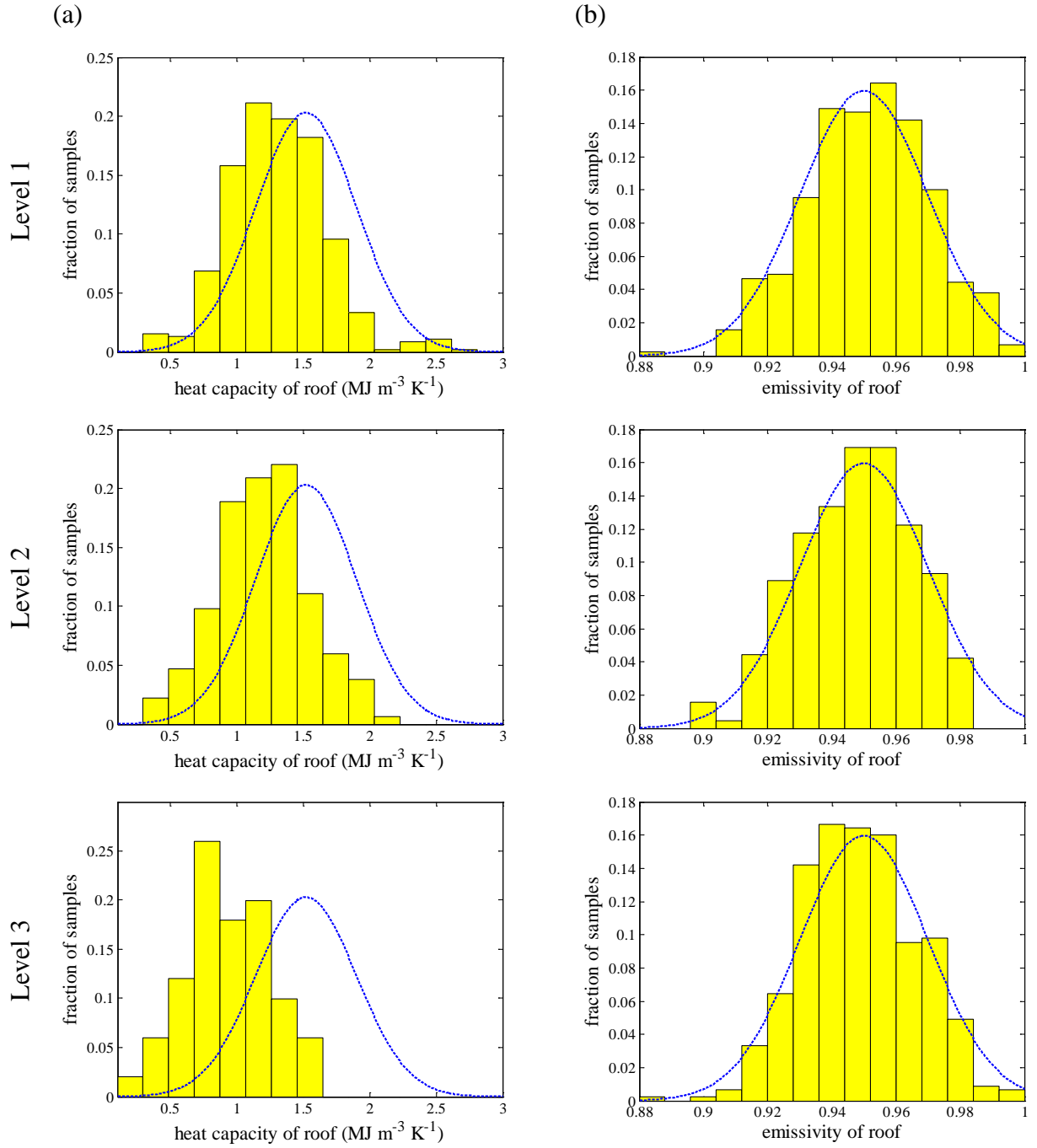
Figure 3.2: Histogram of conditional samples at different conditional levels for (a) a

parameter with high sensitivity, C_R; and (b) a parameter with low sensitivity, ε_R

As shown in Figure 3.2(a), the distribution of the conditional sample for a typical parameter with high sensitivity, experiences a significant deviation from the unconditional distribution (i.e. the predefined PDF, plotted as the dashed line). This indicates that, at higher exceedance probabilities, that parameter was skewed in one direction from its unconditional distribution and hence contributed to the exceedance. On the other hand, the histogram of an insensitive parameter (Figure 3.2(b)) at high exceedance probability levels exhibits insignificant deviation from the unconditional one; i.e. there is no significant relation between the distribution of the parameter and the exceedance rate.

3.2. Sensitivity study of surface parameters

In this section, we apply Subset Simulation to model the uncertainties in surface parameters of the UCM. Again, the meteorological forcing of the UCM is prescribed using measurements of a typical clear day (20 March 2010) from a standard eddy-covariance (EC) station (see section 2.2.3 for details). To enhance the statistical significance, in total we have run more than 1500 simulations (30 independent runs/simulations per monitored output), each having 1850 realizations of the set of 24 uncertain parameters (discussed below, Subset Simulation samples all the 24 uncertain parameters once based on the prescribed initial distributions during one realization).

Table 3.1: Statistics of uncertain parameters

Parameters	Unit	PDF	Min	Max	Mean	Std dev
a_W	-	normal	0	1	0.25	0.0625
a_R	-	normal	0	1	0.15	0.0375
a_{G_imp}	-	normal	0	1	0.27	0.0675
a_{G_veg}	-	normal	0	1	0.18	0.0450
ε_W	-	normal	0.8	1	0.930	0.020
ε_R	-	normal	0.8	1	0.950	0.020
ε_{G_imp}	-	normal	0.8	1	0.950	0.020
$\varepsilon_{G\ veg}$	-	normal	0.8	1	0.960	0.020
k_W	W m^{-1} K^{-1}	normal	0.20	2.00	1.30	0.325
k_R	W m^{-1} K^{-1}	normal	0.20	3.00	1.20	0.300
k_{G_imp}	W m^{-1} K^{-1}	normal	0.20	3.00	1.70	0.425
k_{G_veg}	W m^{-1} K^{-1}	normal	0.15	4.00	0.85	0.213
C_W	MJ m^{-3} K^{-1}	normal	0.10	4.00	1.26	0.315
C_R	MJ m^{-3} K^{-1}	normal	0.10	4.00	1.52	0.380
C_{G_imp}	MJ m^{-3} K^{-1}	normal	0.10	4.00	2.10	0.525
C_{G_veg}	MJ m^{-3} K^{-1}	normal	0.10	2.00	0.72	0.180
T_B	^{o}C	normal	20	28	24	1.0
h	-	uniform	0.2	3	-	-
r	-	uniform	0.3	0.8	-	-
f_{veg}	-	uniform	0	0.6	-	-
$z_{m,R}$	mm	uniform	0.1	5	-	-
$z_{m,can}$	mm	uniform	10	200	-	-
d_R	m	uniform	0.1	0.8	-	-
d_W	m	uniform	0.1	0.8	-	-

3.2.1. Parameter uncertainty

Both groups of inputs to the UCM, meteorological and surface parameters (c.f. Tables 2.1 and 2.2), are associated with uncertainties and their characterization is of fundamental importance. The meteorological forcing is subject to chaotic atmospheric dynamics and cloud formation processes with extremely high uncertainties. Thus the forcing uncertainties can be more appropriately modeled as a stochastic process. In this study, we focus on the uncertainties in surface parameters, which are (scalar-valued) random variables with their PDFs chosen to lie within a physically realistic range.

The statistics of surface parameter uncertainties are listed in Table 3.1, where only one type of impervious ground sub-facet is used here, as denoted by subscript 'imp'. Sources for the mean (representative) values and the range (maximum and minimum values) of thermal properties of engineered materials include: albedos from Sailor and Fan (2002); emissivities from USCB emissivity library (http://www.icess.ucsb.edu/modis/EMIS/html/em.html); thermal conductivities and heat capacities from ASHRAE handbook (2009). Thermal properties for vegetated surface are chosen so that the albedo and the emissivity are representative of grass (Brutsaert, 2005), while the thermal conductivity and the heat capacity are those of sublayer soils (Abu-Hamdeh and Reeder, 2000; Campbell *et al.*, 1991). All thermal properties are associated with a normal distribution and a standard deviation 25% of the mean values, except for emissivities, for which a smaller variance is used based on both physical (not to exceed practical limits) and statistical (larger standard deviation contaminates the normal distribution of emissivity) considerations. Uniform PDFs are assigned to normalized dimensional parameters (the normalized building height h, r, and f_{veg}), roughness lengths and

thickness of roofs and walls, weighing all possible values equally in the range listed in Table 3.1. The choice of the normalized dimensions for real urban areas is based on Grimmond and Oke (1999), with conversion from building block representation of urban areas to 1D infinite canyon. Note that the range of normalized building heights is wide, from 0.2 (town houses in sub-urban areas) to 3.0 (skyscraper in megacities). Moreover, we associate the uncertainties of roughness lengths of heat to the ones of momentum through $z_h = z_m / 10$, for both roofs and canyons (see Nadeau *et al.*, 2009 for a discussion of the relation of the two parameters for urban areas).

3.2.2. Conditional samples

Using the prescribed forcing, we run the UCM using Subset Simulation. One realization of the statistics of surface parameters in Table 3.1 yields a prediction of diurnal variation of heat fluxes (*H*, *LE* and *G*) and surface temperatures. We record the critical (peak) values of heat fluxes or temperatures during the diurnal cycle, which are then used, one at a time, as monitored responses to define exceedance probabilities. In all subsequent simulations, we use 4 levels, a conditional probability of $p_0 = 0.1$, and 500 samples per level. The statistical distributions of the set of input parameters associated with these simulations are then compared to original imposed distribution (see Figure 3.2). Here we define a quantitative index, called the "percentage sensitivity index" (PSI, expressed in percentage), to measure the relative sensitivity of each uncertain parameter

$$\text{PSI} = \frac{1}{N_{level}} \sum_{j=1}^{N_{level}} \frac{E\left[X|Y > y_j\right] - E\left[X\right]}{E\left[X\right]} \qquad (3.5)$$

54

where j = 1, 2,…, N_{level} is the index of conditional sampling level, with N_{level} the number of levels of exceedance probability (in this case, N_{level} = 4); $E[X]$ is the expected (statistical mean) value of the unconditional distribution (as in Table 3.1) of the uncertain parameter of interest X and $E[X \mid Y > y_j]$ is the expected value of X at conditional level j. Note that the magnitude of the PSI indicates the sensitivity (deviation of conditional means). In addition, the sign of PSI indicates the sign of correlation between the monitored output and the uncertain input parameter, e.g. a negative PSI implies that increasing the uncertain input value results in a decrease of the monitored model output, and *vice versa*.

Before proceeding to examine the results in detail, we need to emphasize here that this sensitivity study is on the UCM and its physical parameterization and application in meteorological models. The results discussed below represent the real physics of urban areas only to the extent that the model is faithful to these physics.

3.2.3. Sensitivity of heat fluxes

We monitored the critical values of 9 heat budgets including: 4 total sensible heat fluxes over the urban area H_u with C_e = 0.0, 0.3, 0.6, and 1.2, the sensible heat from the canyon H_{can}, the sensible heat from the roof H_R, the total latent heat over the urban area LE_u, the indoor conductive heat fluxes through the roof $G_{R,i}$ and the wall $G_{W,i}$, and the net radiative flux from over the urban area R_n. Note that C_e = 0 implies that evaporation is practically suppressed over the vegetated surface. For monitored heat flux other than H_u,

the evaporation from the vegetated surface is active with a moderate coefficient $C_e = 0.6$ by default, unless otherwise specified.

Plots of exceedance probabilities versus the selected peak/critical heat budgets during a diurnal cycle, each averaged over 30 simulations, are shown in Figures 3.3-3.5. Figure 3.3 shows that with the given uncertainty in the surface parameter space, there is a significant variation of the peak diurnal sensible heat fluxes, ranging from 50 W m^{-2} to 200 W m^{-2} (with 10% exceedance probability). This is the range that the simulation can produce when the parameters are varied within the limits we defined. Similar results are observed for other critical turbulent fluxes (peaks of diurnal H_{can}, H_R, and LE_u, $G_{R,i}$, $G_{W,i}$ and R_n). This illustrates the importance of uncertainty in the surface parameter space: significant errors in model prediction could arise from the inaccurate determination of surface parameters. Figure 3.3 also shows that if the vegetated surface is dry ($C_e = 0.0$), the critical sensible heat flux, over the entire urban area during a diurnal cycle, is higher than when the vegetated surfaces are evaporating. This is obvious since when evaporation is suppressed over the vegetated surface, more energy is available for release as sensible heat into the atmosphere from the underlying urban area. On the other hand, with evaporative vegetated surfaces, the critical H_u decreases with increasing C_e, but the decrease is not large. This suggests that latent heat is the least adequately parameterized scheme (as noted by Grimmond *et al.*, 2010) in the current UCM. The parameterization scheme for latent heat has relatively weak dependence on the surface temperature through the saturated humidity q_s^*. This implies that the monitored critical sensible heat (strongly modulated by the surface temperature) does not vary with the evaporation coefficient C_e

significantly (Figure 3.3), albeit a somehow stronger correlation is expected in real urban terrains.

Estimates of the PSI for the monitored turbulent fluxes are shown in Table 3.2. To facilitate visualization of these results, a bar graph for PSI (with $C_e = 0.6$ for H_u) estimates is also shown in Figure 3.6. For all the heat flux outputs, the canyon dimensions, i.e. normalized building height h and roof width r, are of general importance in modulating the fluxes, with PSI > 20% in most cases. This implies that the geometric configuration of street canyons plays an essential role in determining the urban-atmosphere energy exchange.
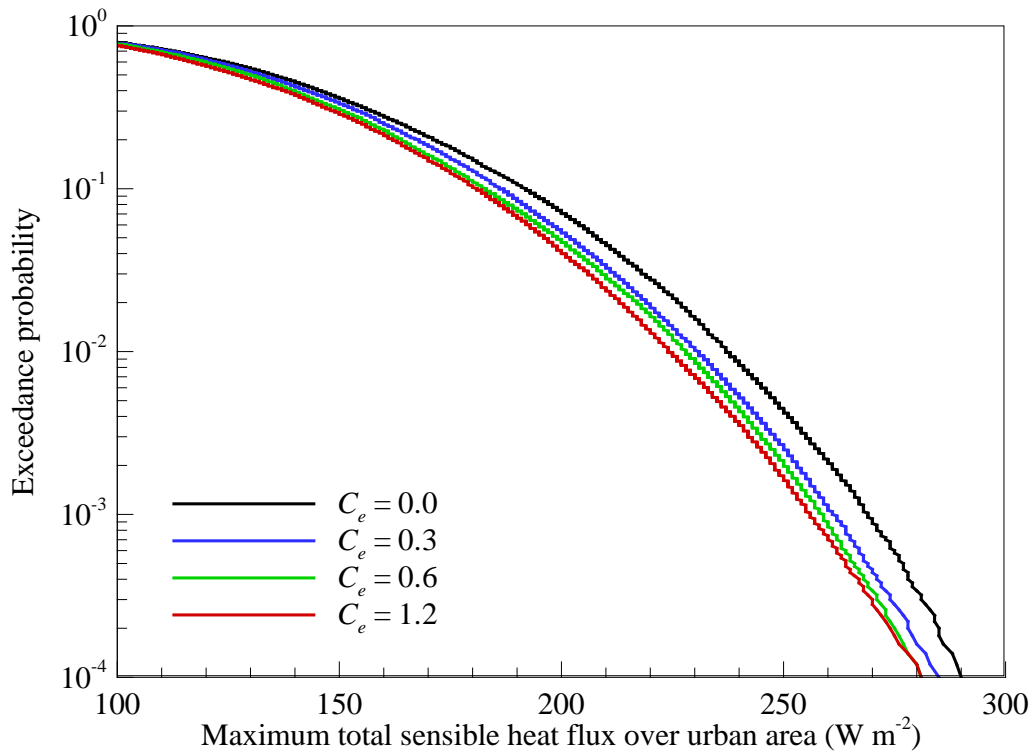
Figure 3.3: Estimates of exceedance probability versus maximum sensible heat over the urban area H_u, with the atmospheric forcing conditions of 20 March 2010 (clear day)
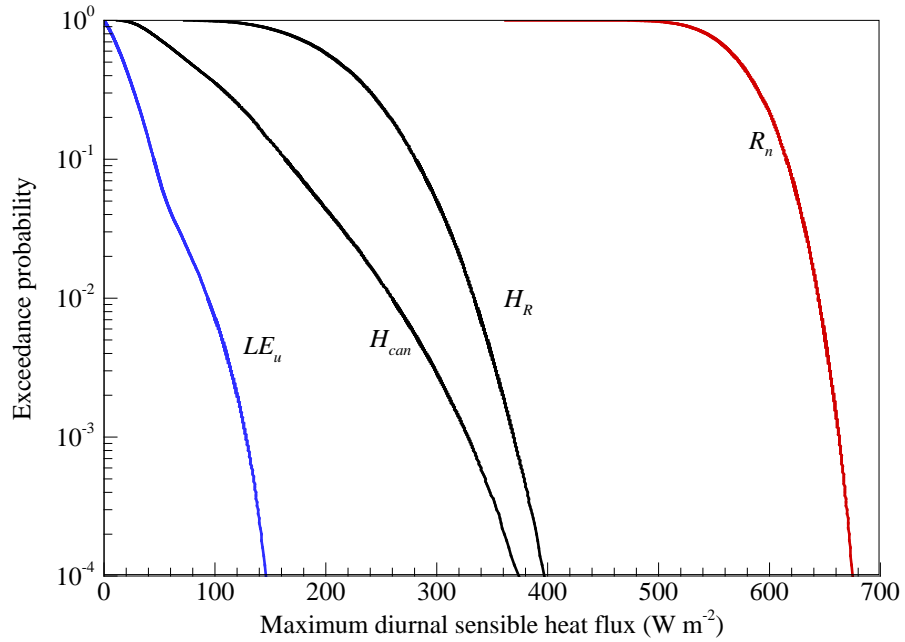
Figure 3.4: Estimates of exceedance probability versus maximum H_{can}, H_R, LE_u and R_n

with the atmospheric forcing conditions of 20 March 2010 (clear day)
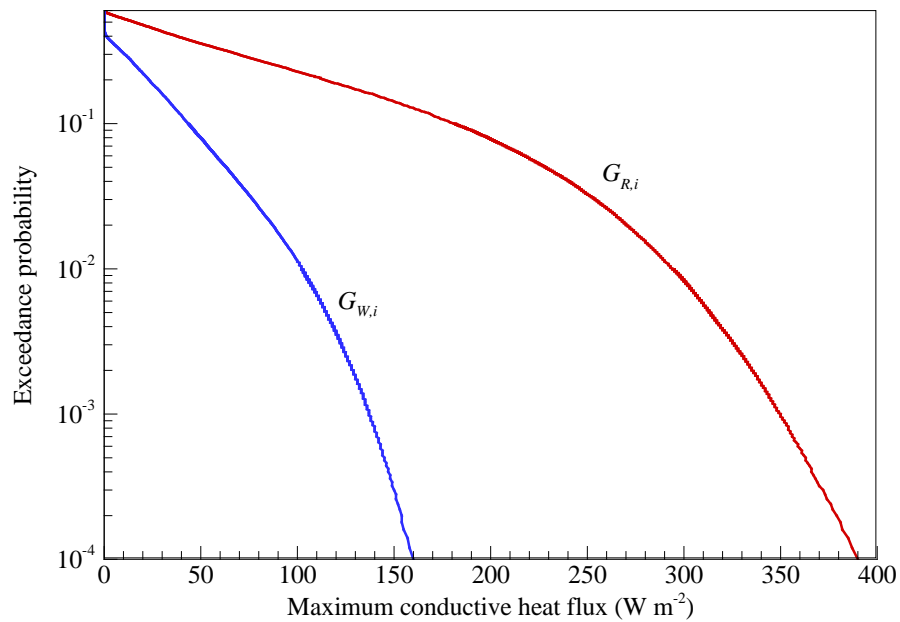
Figure 3.5: Estimates of exceedance probability versus maximum $G_{W,i}$ and $G_{R,i}$ with the

atmospheric forcing conditions of 20 March 2010 (clear day)

Table 3.2: Estimates of PSI for monitored critical (maximum) diurnal fluxes with the atmospheric forcing conditions of 20 March 2010 (clear day)

| Uncertain parameters | H_u | | | | H_{can} | H_R | LE_u | $G_{R,i}$ | $G_{W,i}$ | R_n |
	$C_e = 0.0$	0.3	0.6	1.2			$C_e = 0.6$			
a_W	-4.4	-5.3	-3.0	-3.2	0.2	-3.6	0.5	0.1	-8.7	-36.2
a_R	-15.6	-16.1	-17.7	-17.2	-1.8	-25.7	-0.5	-11.2	-0.5	-27.0
a_{G_imp}	-0.5	0.8	-0.9	-1.3	-0.4	-0.5	4.3	0.2	-0.3	-1.5
a_{G_veg}	-1.1	-0.9	-0.4	0.1	-0.6	0.1	-4.9	2.3	0.3	-3.8
ε_W	0.0	0.1	-0.3	0.1	0.0	-0.1	0.0	-0.1	-0.1	0.7
ε_R	-0.2	-0.4	-0.2	-0.5	0.1	-0.5	-0.2	-0.1	0.0	-0.3
ε_{G_imp}	0.1	0.0	-0.1	0.1	0.0	0.2	-0.1	0.0	0.0	-0.2
ε_{G_veg}	0.1	0.0	-0.3	-0.1	0.1	-0.2	0.0	0.1	0.0	-0.1
k_W	-3.7	-2.2	-2.3	-0.8	10.6	-0.1	-0.7	1.0	13.5	-5.0
k_R	-14.0	-17.3	-18.7	-16.9	1.0	-23.1	2.4	27.5	-2.1	2.2
k_{G_imp}	0.6	-1.4	-1.3	-2.2	-1.4	-2.1	0.2	-0.1	0.6	-1.2
k_{G_veg}	-1.5	-1.3	1.5	1.8	0.4	0.1	-0.8	0.7	-2.5	0.1
C_W	-19.0	-8.4	-12.0	-11.1	-3.4	0.3	-2.6	-1.0	-5.4	10.0
C_R	-24.8	-31.7	-27.5	-26.6	-1.0	-34.2	0.8	-6.6	-0.2	19.8
C_{G_imp}	-6.4	-4.2	-3.2	-5.0	-1.2	1.1	1.6	-1.7	-2.9	1.9
C_{G_veg}	-3.0	-0.9	-0.2	1.2	-0.5	1.9	-1.8	-0.1	-0.9	0.9
T_B	1.2	1.3	1.5	1.7	2.5	0.6	0.4	-0.6	-1.1	-0.4
h	-48.1	-26.1	-26.7	-21.0	49.6	18.1	-69.5	0.2	-61.0	34.6
r	6.8	23.5	24.0	27.1	26.8	-21.2	-32.7	4.8	-14.1	-24.1
f_{veg}	21.4	-1.0	-15.0	-16.9	-8.3	0.6	83.3	-2.4	-13.5	-5.8
$z_{m,R}$	48.9	55.3	53.9	56.3	0.0	59.8	-0.2	-30.5	1.6	2.2
$z_{m,can}$	25.7	10.2	14.4	10.9	52.6	-1.5	-0.1	1.5	-13.4	-1.2
d_R	-25.5	-26.5	-31.1	-34.2	-0.2	-25.9	1.5	-74.0	1.4	35.4
d_W	-35.9	-32.6	-35.8	-34.4	-65.6	6.7	-12.2	0.4	-70.6	10.1

Moreover, critical sensible heat fluxes also have strong correlations with the roughness lengths ($z_{m,R}$ for the roof and the total sensible heat flux, $z_{m,can}$ for canyon sensible heat flux) with PSI around 50%, and with the thickness of roofs and walls with PSI around 30%. As far as the evaporation from the urban area is concerned, the critical latent heat is mainly controlled by the presence of vegetated surfaces. It is not surprising that the critical latent heat is most sensitive to the fraction of vegetated surface f_{veg}. Otherwise, the dimensions of the canyon (h and $r = 1 - w$) determine the local turbulence intensity inside the canyon and therefore have high impact on the model since they control the efficiency of turbulent transport of heat from the street canyon. One interesting observation from Table 3.2 is that an increase of h is associated with increase in both H_R and H_{can} (with positive PSI) but leads to decrease in H_u (negative PSI). This is an intriguing result that is probably due to the complex interactions of the model parameters and their effects on the output. For example, increase in r (with positive PSI for H_u) leads to decrease in H_R but increase in H_{can}. This could partially compensate the effect of reduction in H_{can} and H_R due to decrease in h in maximizing H_u. The negative correlation between h and H_u is in agreement with Loridan *et al.* (2010), albeit they did not investigate the correlation for the components H_R and H_{can}.

Now consider the thermal parameters. For total sensible heat over urban areas, the roof properties control the maximum energy transport, with a_R, k_R, C_R, having PSI values greater than 15% (compared to those of the walls and paved and vegetated ground surfaces with PSI < 5%). The only exception is the heat capacity of the wall C_W (PSI around 10~20%). This is also clear from Figure 3.4, where for the entire range of

exceedance probability, the sensible heat from the roof is always greater than the one from the canyon. The generic conductive fluxes $G_{R,i}$ and $G_{W,i}$, which are representative of the heating/cooling loads required in this buildings, are modulated by the thermal properties of roof and wall respectively. H_{can} is exclusively controlled by k_W (the effects of the other thermal properties in the canyon are speculated to counter-interact one another to yield low PSI). The same set of parameters control H_R and $G_{R,i}$, but with the opposite signs in the PSI of k_R indicating the competition between the conduction and convection processes over the roof layer. It is noteworthy that all the heat fluxes, either from the canyon or the roof, are relatively insensitive to the thermal properties of ground surfaces, be it paved (impervious) or natural (vegetated).

Emissivities, with the given uncertainty statistics, have minimal significance for the model output (all PSI < 0.5%). For most engineered and natural materials, the mean emissivity over a range of wavelength is approximately 0.9~0.95 (c.f. Table 3.1). With the upper and lower limits of 1.0 and 0.8 respectively, the absolute maximum magnitude of PSI that can be achieved by variation of emissivity is 11%. Numerical experiments (not presented here) show that for emissivity to achieve comparable range of PSI of other uncertain parameters, the conditional samples at higher levels (2 or 3) will be deviated and distributed in the range $0 < \varepsilon < 0.5$. This is clearly not a realistic range for real materials. Similarly, maintaining the temperature inside the building in the comfort range [20 ^{o}C, 28 ^{o}C] results in the uncertainty in T_B being insignificant for model predictions (PSI < 2%).
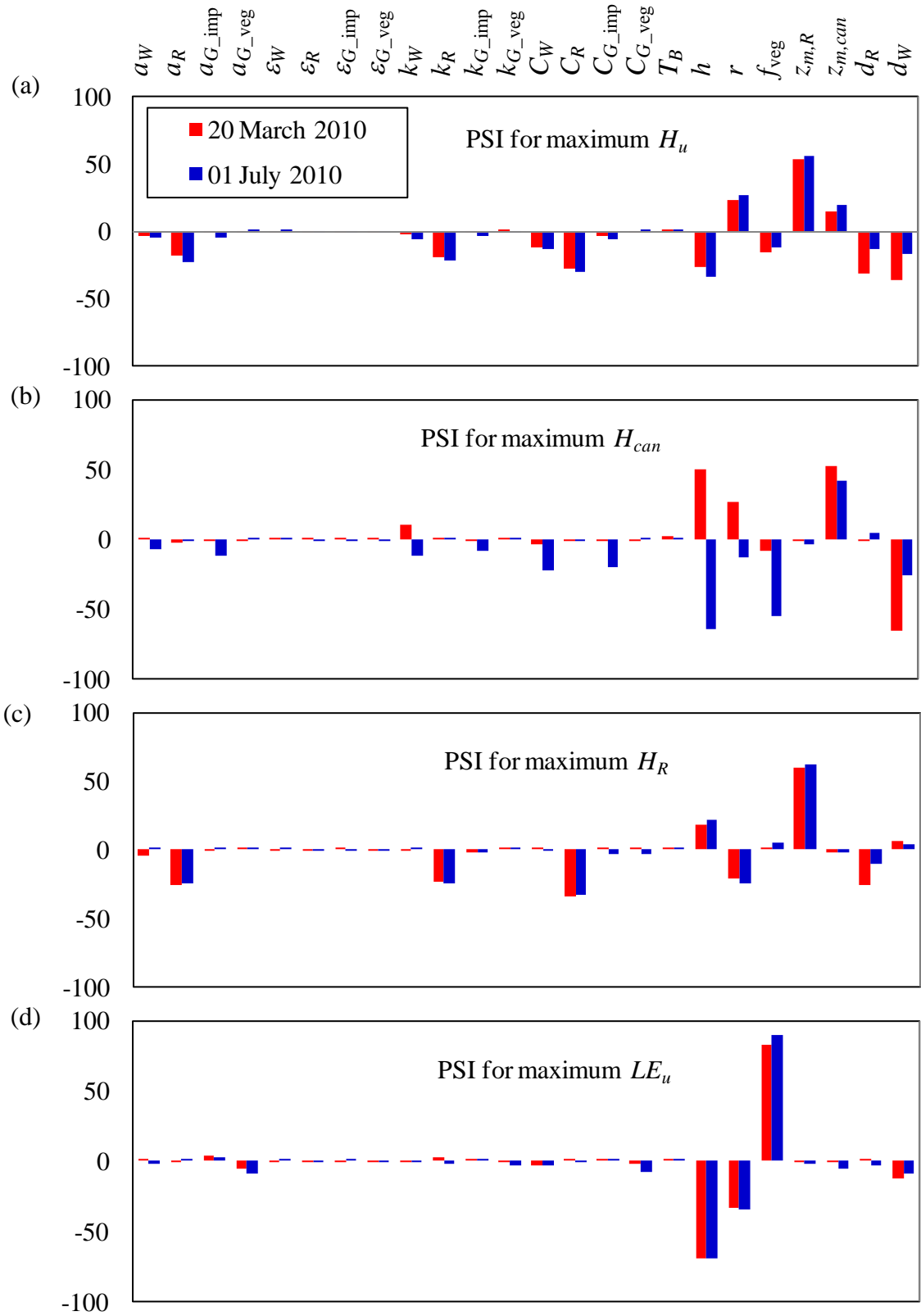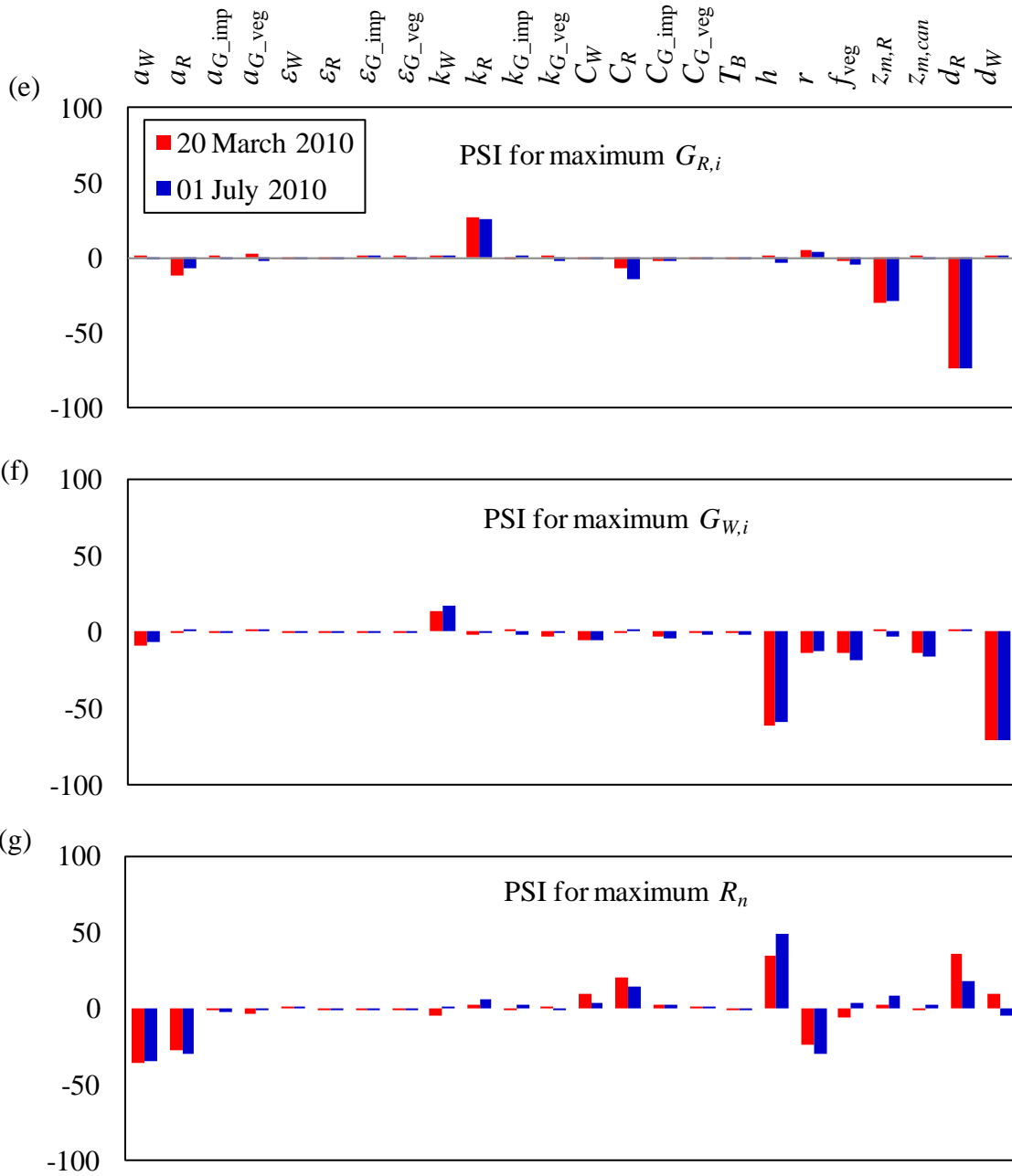
Figure 3.6: Estimates of PSI for monitored critical (maximum) diurnal fluxes of (a) H_u, (b) H_{can}, (c) H_R, (d) LE_u, (e) $G_{R,i}$, (f) $G_{W,i}$, and (g) R_n under both clear (20 March 2010) and cloudy conditions (01 July 2010), all with the default $C_e = 0.6$

A closer examination of the PSI of uncertain parameters for critical H_u responses, apparently suggests that the critical sensible heat exchange between the urban canopy and the atmosphere is primarily modulated by the buildings rather than by the paved or vegetated ground surfaces. Conceivably, buildings affect the turbulent (sensible) energy transport arising from urban areas in the following ways:

(1) Use of engineered materials (nearly impervious), particularly in the roof, yields excessive heating of the surface and transport of energy back to the atmosphere primarily as sensible heat (Fernando 2010);

(2) Radiative trapping inside the street canyon by building arrays reduces the effective albedo of the urban surface;

(3) Heating of the atmosphere due to the energy use inside buildings to maintain comfort range of internal temperature (either by indoor heating and conduction/leakage to the outside or by the rejection of the heat gained through the building envelope through heat pumps used for cooling); and

(4) Increase in roughness length due to the presence of buildings, with enhanced vertical energy transport.

The importance of the building parameters to UCM predictions is also demonstrated in the PSI for maximum net radiation (Figure 3.6). While critical R_n is highly sensitive to albedos of the roof and wall, its sensitivity to thermal properties of ground surfaces (be it vegetated or impervious) is rather insignificant. The parameter sensitivity is similar for vegetated surfaces having different evaporative power, ranging from $C_e = 0$ to 1.2 with critical H_u monitored. One interesting difference between these

cases is the role of vegetated surface. The PSI of f_{veg} is positive if evaporation from the vegetated surface is suppressed ($C_e = 0$), but negative otherwise. This reflected the fact that as the vegetated surface evaporation increases, sensible heat necessarily decreases. Therefore, an increase in the fraction of vegetated surface reduces the total sensible heat exchange between urban areas and the atmosphere (negatively correlated). However, if the vegetated surface does not evaporate, it has a higher contribution to sensible heat (positively correlated) than a paved ground surface due to its low heat storage capacity.

3.2.4. Sensitivity of surface temperatures

Estimates of exceedance probability versus critical roof, wall and ground surface temperatures are plotted in Figures 3.7 and 3.8. Note that with meteorological forcing of 20 March 2010 (clear day), there is a log-concavity in the exceedance probability versus maximum ground surface temperature for both the impervious and the vegetated surfaces. The log-concavity found in T_{G_veg} is also responsible for the similar pattern observed in Figure 3.4 for LE_u. The existence of a log-concavity in exceedance probability suggests that the model response of ground surface temperature is dictated by the radiative trapping inside the canyon, which exhibits distinct features under different regions of normalized building height h. The higher ground surface temperature range corresponds to smaller values h, *vice versa*. The log-concavity demarks the switching between these two influence regions, as illustrated in Figure 3.9. As verification, for a cloudy day (on 01 July 2010), where radiative trapping effect is not as significant as that in a clear day, the log-concavity of surface temperature response disappears as expected (Figure 3.8).
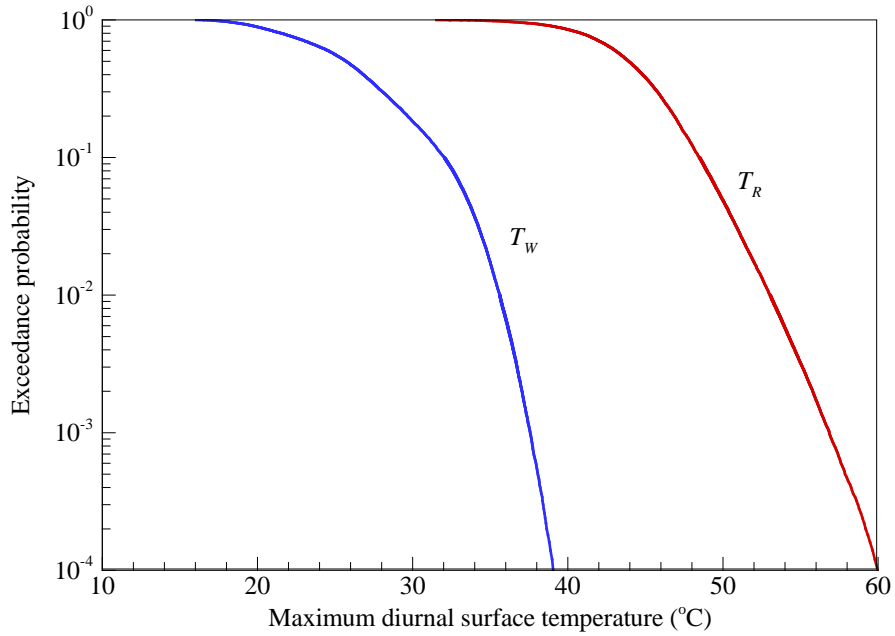
Figure 3.7: Estimates of exceedance probability versus maximum T_R and T_W with the atmospheric forcing conditions of 20 March 2010 (clear day)
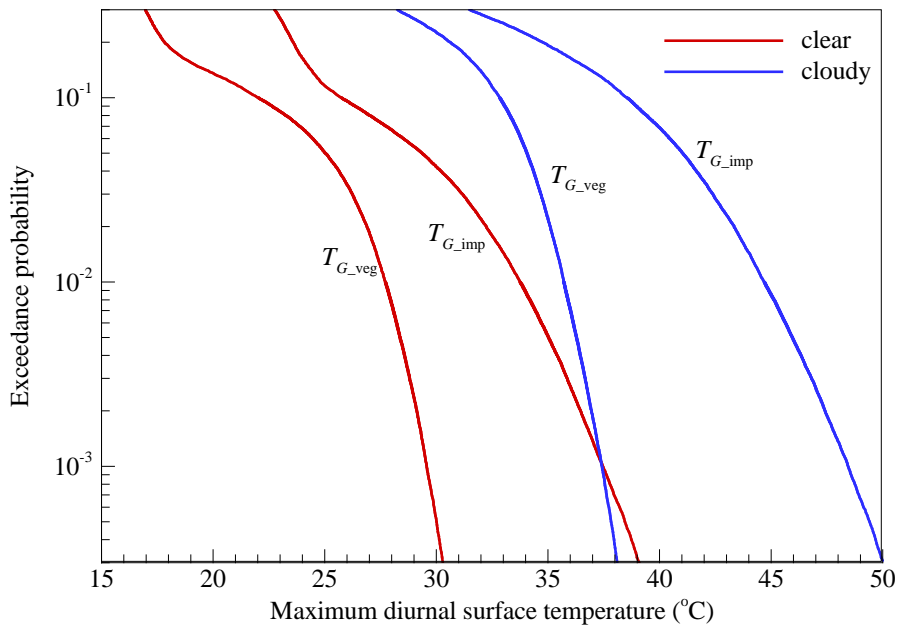
Figure 3.8: Estimates of exceedance probability versus maximum T_{G_imp}, and T_{G_veg} with the atmospheric forcing of 20 March 2010 (clear day) and 01 July 2010 (cloudy day)
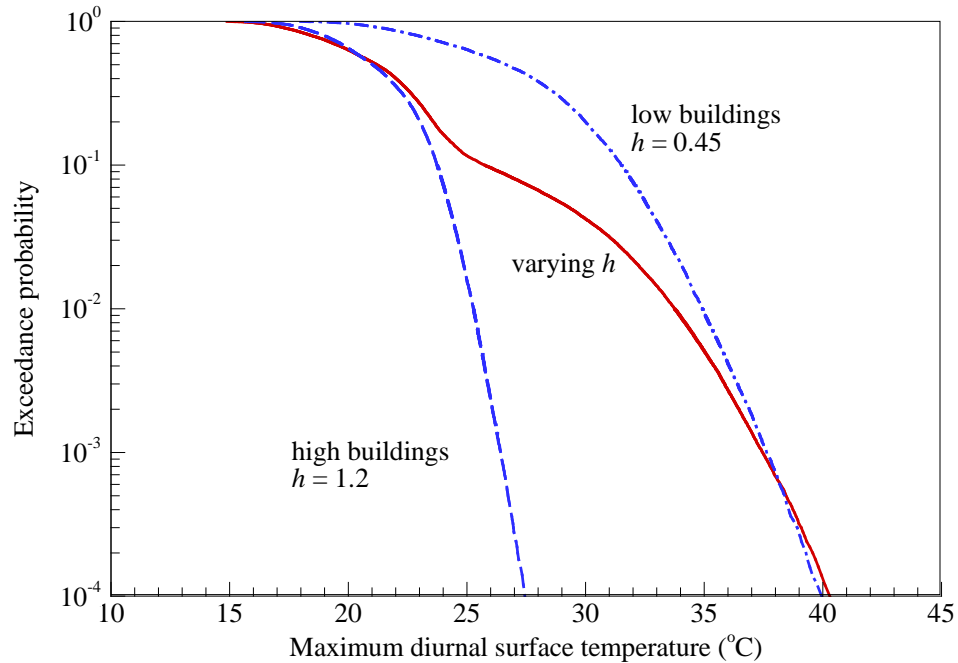
Figure 3.9: Illustration of the impact of different regions of normalized building height h

on T_{G_imp} with distinct radiative trapping features in a clear day (20 March 2010)

PSI estimates for the critical temperature of different surfaces are listed in Figure 3.10 and Table 3.3. As expected, critical temperatures are dictated by the thermal properties of the corresponding surfaces. The influence of emissivities and interior building temperatures, given the physical range of variation is insignificant compared to other thermal properties. Again, canyon dimensions, particularly the canyon height h, strongly modulate surface temperatures. Roughness lengths of the roof and the canyon influence the surface temperature of roof and canyon surfaces respectively. The surface temperature of the building enclosure (roof and wall) is also determined by the thickness of the enclosure (d_R and d_W). The moderate sensitivity of critical ground surface temperatures to d_W, on the other hand, is likely to be the result of the complex interactions of model parameters, or due to multiple radiative reflection inside the street canyon.

Table 3.3: Estimates of PSI for monitored critical (maximum) diurnal surface temperatures with the atmospheric forcing conditions of 20 March 2010 (clear day)

Uncertain parameters	Monitored critical response			
	T_R	T_W	T_{G_imp}	T_{G_veg}
a_W	-0.1	-20.1	-0.3	0.1
a_R	-19.2	-0.9	0.9	1.8
a_{G_imp}	3.7	1.5	-12.9	2.3
a_{G_veg}	-2.7	0.0	-1.5	-12.4
ε_W	0.0	0.1	0.0	0.0
ε_R	-0.1	-0.2	-0.2	-0.1
ε_{G_imp}	0.0	-0.2	-0.1	-0.2
ε_{G_veg}	0.0	-0.1	0.0	-0.2
k_W	0.7	-13.6	3.1	-4.0
k_R	-22.5	1.5	0.4	-1.6
k_{G_imp}	-0.7	-4.1	-8.6	1.9
k_{G_veg}	-2.4	0.7	-2.9	-5.7
C_W	-1.6	-27.5	-6.1	-1.7
C_R	-38.3	-1.1	0.7	1.3
C_{G_imp}	-0.5	-9.2	-19.8	1.0
C_{G_veg}	0.4	1.5	2.8	-5.8
T_B	0.7	1.0	0.1	0.1
h	-0.8	-73.5	-80.9	-82.1
r	5.2	-16.8	-21.8	-23.7
f_{veg}	-0.7	-17.3	-7.0	30.2
$z_{m,R}$	-71.8	0.8	-3.2	0.5
$z_{m,can}$	-3.5	-17.9	-13.4	-24.1
d_R	-24.7	2.6	0.8	-0.1
d_W	4.4	-26.4	-18.7	-6.5
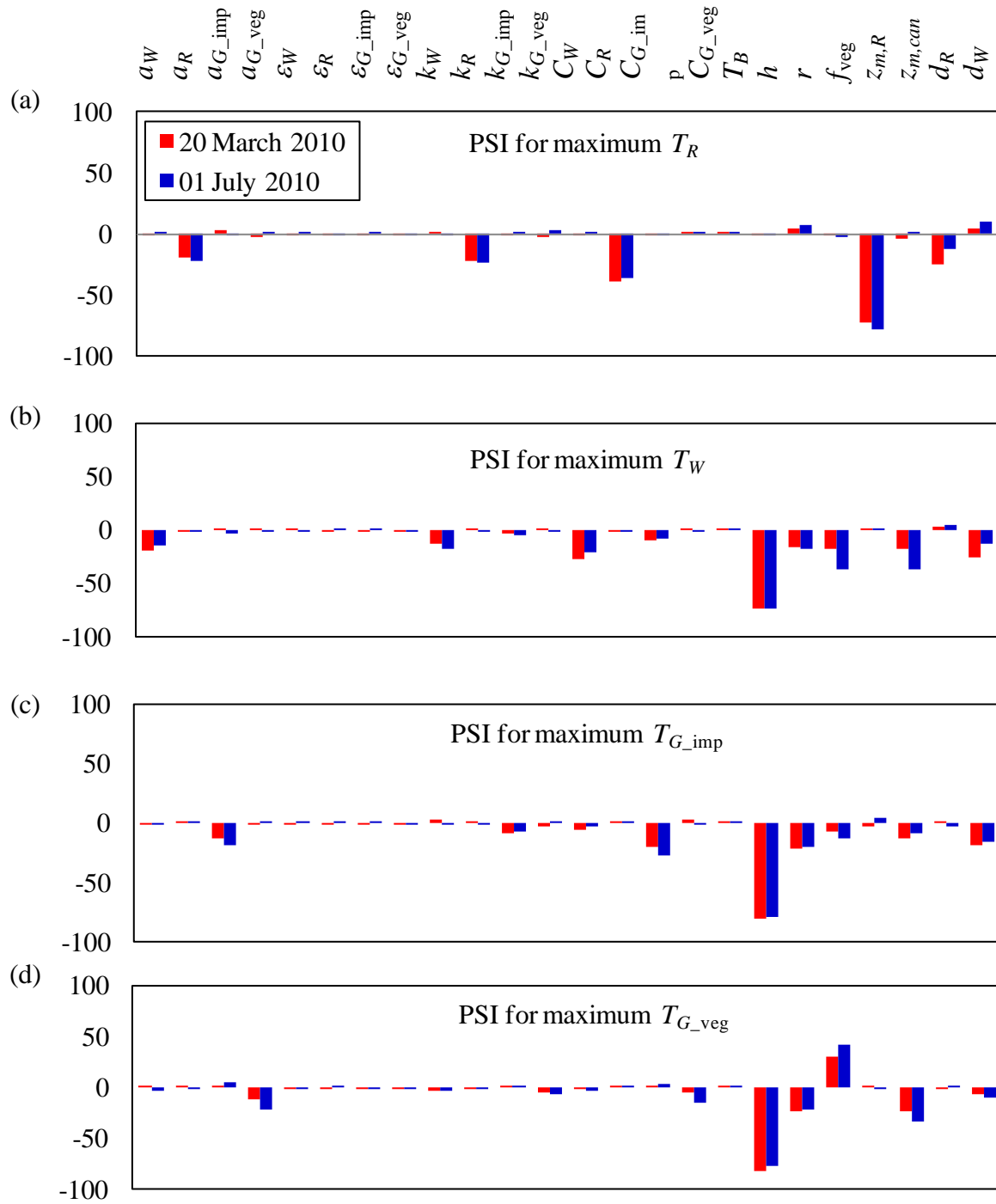
Figure 3.10: Estimates of PSI for monitored maximum (a) T_R, (b) T_W, (c) T_{G_imp} and (d) T_{G_veg} under both clear sky conditions (20 March 2010) and cloudy conditions (01 July 2010), all with the default $C_e = 0.6$

69

3.2.5. Effect of weather conditions

To investigate the effect of different weather conditions on the sensitivity study, we ran a second set of simulations driven by meteorological forcing on 01 July 2010 (characterized by the presence of large cloud-cover fraction and high air temperatures). PSI estimates for monitored critical responses of heat flux and surface temperature are listed in Tables 3.4 and 3.5, respectively. Comparing Tables 3.2 and 3.3 against Tables 3.4 and 3.5, it is found that the sensitivity of surface parameters, for both the critical heat flux and the critical surface temperature response of the model, is generally independent of the meteorological forcing. Plots of PSI bars in Figures 3.6 and 3.10 exhibit very similar trend, under either clear or cloudy weather conditions. One prominent difference is the PSI of the three important canyon dimensional parameters: h, r and f_{veg}, when maximum H_{can} is monitored. Both h and r have positive PSI for the H_{can} response in the diurnal variation of a clear day (20 March), while their PSI was negative for the cloudy day. This indicates that the extremely high sensible heat flux arising from the canyon is likely to happen in areas with high building density (larger h and r values) during a clear day. In contrast, for a cloudy day (negative PSI), the model prediction of extreme H_{can} response is likely to happen in suburban areas. Also note that the response of H_{can} is highly sensitive to f_{veg} during a cloudy day but relatively insensitive during a clear day, showing that the vegetated surface plays an important role in regulating H_{can} when it is cloudy. In addition, it is noteworthy that the response of critical total sensible heat has higher sensitivity to the thickness d_W and d_R during a clear day.

Table 3.4: Estimates of PSI for monitored critical (maximum) diurnal fluxes with the

atmospheric forcing conditions of 01 July 2010 (cloudy day)

Uncertain	H_u				H_{can}	H_R	LE_u	$G_{R,i}$	$G_{W,i}$	R_n
parameters	$C_e = 0.0$	0.3	0.6	1.2			$C_e = 0.6$			
a_W	-6.9	-5.0	-4.8	-2.9	-7.3	0.6	-2.1	-1.0	-6.6	-34.7
a_R	-12.7	-20.2	-22.9	-21.3	-0.9	-24.8	0.8	-6.7	1.5	-29.6
a_{G_imp}	-2.2	-0.7	-4.1	-1.2	-11.4	0.8	2.5	-1.1	-0.9	-2.4
a_{G_veg}	-5.4	-2.5	1.4	2.2	1.3	1.9	-9.2	-1.6	0.0	-1.4
ε_W	0.0	0.0	0.1	-0.1	0.0	0.1	0.1	-0.1	-0.2	0.6
ε_R	-0.2	-0.3	-0.1	-0.2	-0.2	-0.5	-0.1	-0.2	0.0	-0.3
ε_{G_imp}	0.0	0.0	-0.1	-0.1	-0.1	0.0	0.0	0.1	0.0	-0.1
ε_{G_veg}	0.1	0.0	0.0	-0.1	-0.1	-0.1	-0.2	-0.1	-0.1	-0.2
k_W	-5.8	-6.0	-5.7	-2.7	-12.2	1.1	-0.6	0.2	17.0	0.8
k_R	-14.8	-19.4	-21.0	-19.4	0.2	-23.8	-2.0	26.3	-0.7	6.2
k_{G_imp}	-4.1	-0.7	-3.8	-2.3	-8.4	-2.0	1.9	1.2	-1.2	2.4
k_{G_veg}	-0.6	1.4	-0.9	-1.9	0.1	2.1	-3.2	-1.5	-0.4	-1.2
C_W	-13.8	-11.7	-12.4	-8.9	-22.2	-0.6	-2.7	-1.1	-5.3	3.9
C_R	-23.8	-31.0	-29.7	-30.9	-0.1	-33.1	-0.4	-14.0	1.7	14.3
C_{G_imp}	-4.0	-5.6	-5.7	-2.5	-19.9	-2.8	0.5	-1.8	-4.0	2.7
C_{G_veg}	-4.1	-3.1	1.8	-1.7	0.0	-2.7	-7.1	-0.2	-2.3	0.5
T_B	1.2	1.3	0.9	0.8	1.5	0.4	0.1	-0.3	-1.2	-0.6
h	-60.1	-33.9	-33.8	-28.1	-63.6	22.0	-68.8	-3.8	-59.2	49.0
r	-0.4	23.3	27.5	27.1	-12.4	-24.0	-33.9	3.6	-12.1	-29.6
f_{veg}	30.3	-6.5	-11.4	-16.0	-54.2	5.2	89.7	-5.0	-18.4	3.2
$z_{m,R}$	45.2	56.6	55.9	58.2	-3.5	62.1	-1.4	-28.5	-2.8	8.7
$z_{m,can}$	30.2	22.3	19.5	16.4	42.1	-2.0	-5.4	-0.8	-16.1	2.7
d_R	-6.9	-10.3	-12.7	-8.8	4.9	-10.5	-2.9	-73.7	0.9	17.9
d_W	-12.6	-12.9	-17.1	-12.0	-25.2	4.2	-8.1	0.4	-71.0	-5.3

Table 3.5: Estimates of PSI for monitored critical (maximum) diurnal surface

temperatures with the atmospheric forcing conditions of 01 July 2010 (cloudy day)

Uncertain	Monitored critical response			
parameters	T_R	T_W	T_{G_imp}	T_{G_veg}
a_W	0.8	-14.1	-0.7	-3.6
a_R	-22.4	-0.4	1.7	-0.9
a_{G_imp}	-1.1	-3.2	-19.4	5.5
a_{G_veg}	1.8	-0.6	1.7	-22.1
ε_W	0.2	0.0	0.0	-0.2
ε_R	-0.2	0.2	0.1	0.0
ε_{G_imp}	0.1	0.1	0.1	-0.2
ε_{G_veg}	0.0	-0.1	-0.2	-0.1
k_W	-0.2	-17.3	-0.3	-4.0
k_R	-23.4	-0.6	-1.3	-2.2
k_{G_imp}	0.8	-4.4	-7.7	2.2
k_{G_veg}	2.7	-2.5	0.8	-6.6
C_W	0.1	-21.6	-3.4	-3.4
C_R	-36.0	-1.3	1.0	0.5
C_{G_imp}	-1.5	-7.5	-26.7	3.8
C_{G_veg}	1.9	-1.2	-2.2	-14.4
T_B	0.7	1.2	0.1	0.2
h	-1.2	-73.3	-78.8	-77.4
r	8.0	-18.2	-20.4	-22.0
f_{veg}	-2.4	-37.5	-12.4	42.2
$z_{m,R}$	-78.0	0.8	3.7	-2.4
$z_{m,can}$	1.0	-36.5	-9.1	-33.6
d_R	-12.0	3.8	-2.9	2.0
d_W	10.5	-13.1	-16.2	-10.8

3.2.6. Statistical error

Subset Simulation is much more numerically efficient compared to classic Monte Carlo simulation (MCS). In this section, we investigate the statistical error by computing the coefficient of variation (c.o.v. = standard deviation/mean, a normalized measure of the dispersion of the PDF) of exceedance probability estimates using 30 independent simulations. The results are plotted in Figure 3.11. The number of samples used for the estimate of exceedance probability at different levels, viz. $P(F) = 10^{-1}, 10^{-2}, 10^{-3}, 10^{-4}$ are $N_T = 500, 950, 1400, 1850$, respectively. For comparison, the c.o.v. of exceedance probability estimate produced by direct MCS is given by $\delta = \sqrt{(1-P_F)/(P_F N_T)}$, which is also plotted in Figure 3.11. We see that the c.o.v of direct MCS grows drastically with decreasing exceedance probability, indicating that the statistical error for small exceedance probability is high. In contrast, the c.o.v. of Subset Simulation increases much more slowly as the exceedance probability decrease. It is clear that using the same number of samples, Subset Simulation yields much lower statistical error for exceedance probability estimation, as compared to direct MCS.

3.2.7. Practical implication of parameter sensitivity

A direct consequence of anthropogenic stressors on urban areas, as manifested by the turbulent energy exchange and urban surface temperatures, is the so called "urban heat island" (UHI) effect (Oke, 1982). One important implication of this sensitivity study is related to the determination of strategies to mitigate urban heat island intensity. Oleson *et al.* (2010) investigated the effects of white roofs on UHI mitigation. They found that

the annual mean heat island decreased by 33%, averaged over all urban areas, and pointed out that "changing roof albedo should have the largest impact on near-surface urban climate". Their conclusion is confirmed by our study in the sense that the energetics of urban areas are indeed dominated by the presence of buildings (in particular, roofs), rather than impervious pavements. Options also include application of increasingly popular designs of "green" roofs with evaporative potential. Practically, however, increasing the albedo using white roofs can be done with relative ease as compared to other options (e.g. green roofs), because it only involves changing the material skin property.

The results of the sensitivity study can also be extended to provide guidelines for parametric studies and calibration of surface parameter involving UCM. As field measurement of all surface parameters are rarely available for particular application of UCM, knowing the model sensitivity relative to parameter uncertainties can greatly reduce the effort in parameter calibration procedure to yield better model predictions. The sensitivity analysis in this study is "global", in the sense that the uncertain parameter space covers the entire range of physically-possible values, weighted by density distribution functions and not limited to any specific urban morphology or climate. In addition, the statistical sampling of any given uncertainty parameter in Subset simulation is independent of the rest of the parameter space. It is noteworthy however that our broad conclusions are in agreement with Loridan *et al.* (2010), for example both studies indicate that roof properties are significantly more important that canyon properties.
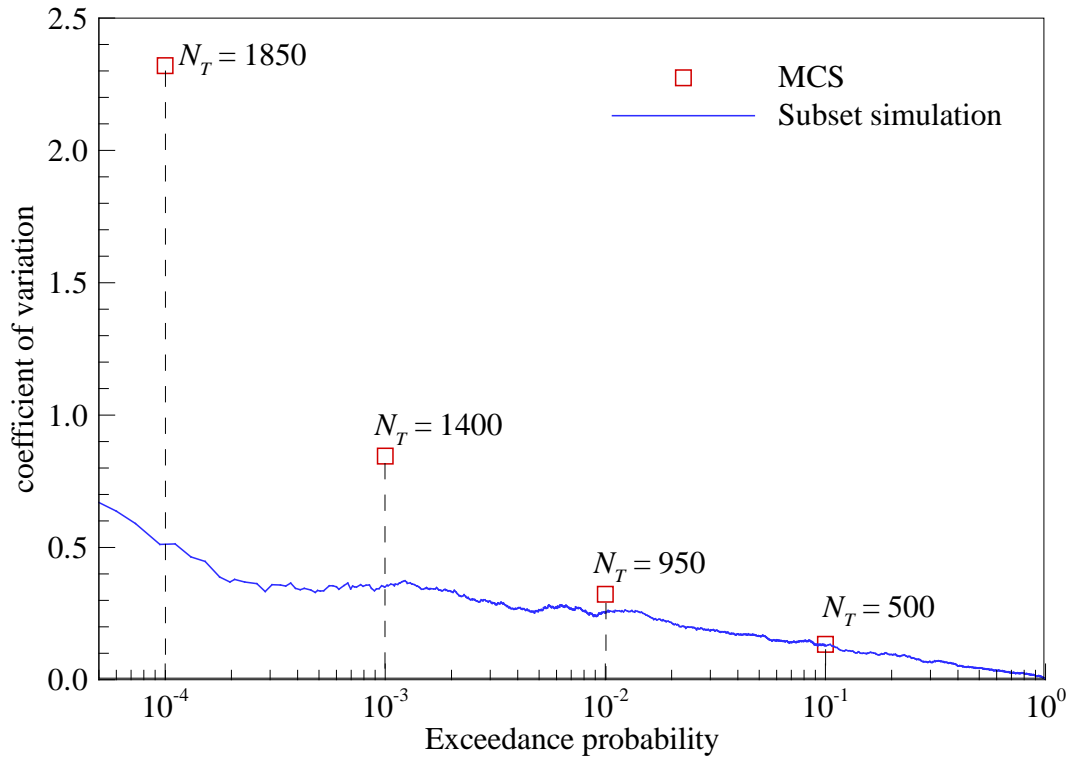
Figure 3.11: Coefficient of variation (c.o.v.) of exceedance probability estimates, c.o.v. is a normalized measure of the dispersion of probability distributions

3.3. Concluding remarks

Subset Simulation, an advanced Monte Carlo procedure, is used to statistically quantify the sensitivity of surface parameter uncertainty in a modified offline version of WRF-UCM. To evaluate the sensitivity of individual parameters, we devise a percentage sensitivity index that measures the deviation of means of conditional samples from the means of the predefined distribution. Results show that critical heat exchange between urban areas and the atmosphere is largely dictated by the presence of buildings and their thermal properties, while impervious pavement or vegetated ground have a relatively

lower impact. Model output of both critical heat fluxes and surface temperature are highly sensitive to the uncertainties in urban geometry, characterized by the normalized building height and roof width. Uncertainties in thermal parameters and thickness of building enclosures (roofs and walls) largely modulate the model output from the corresponding surfaces. Variations in roughness lengths of roof and canyon also have a significant effect on the transport of energy and surface temperatures in urban areas. In contrast, surface emissivities and building interior temperatures, given the physically realistic range of variation, exhibit minimal influence on the UCM predictions.

In general, the meteorological forcing in the UCM, which depends on weather conditions, has a relatively low impact on the characterization of parameter uncertainties. However, the results indicate that the sensitivity of the model to building morphology (h and r) is very different on cloudy or clear days. It is also noteworthy that the anthropogenic heat, not explicitly included in this study, has an important impact on the urban surface energy balance. Its inclusion is similar to a local source term inside urban canopies and may subject to variation of other canopy parameters. It is recommended that for the result of this study to be applied to any specific site, it is preferable to evaluate the local anthropogenic heat whenever conditions permit. There are many foreseeable practical applications of this sensitivity study, e.g. guidance to parametric studies involving UCM and improving UHI mitigation strategies.

Chapter 4

Parameterization schemes for coupled energy and water transport

Here we present detailed parameterization schemes for the new surface exchange model coupling the transport of energy and water budgets inside urban canopies. To briefly recapitulate, the model resolves surface heterogeneity of each urban facet (sub-facet heterogeneity). We also implement detailed urban hydrological models for both natural and engineered materials. Predictions by the model are again validated against field measurements through SNOP. Results from the comparison highlight the importance of coupling the hydrological model for capturing of the subsurface hydrological processes and for more accurate prediction of evaporation, particularly from vegetated surfaces. The new model is also applied to a case study investigating the effect of green roofs in the mitigation of UHI effect.

4.1. Surface exchange of energy budgets

4.1.1. Radiation budgets

The energy balance equation solved by the UCM for the whole atmospheric layer occupied by buildings is given in Eq. (1.1). The presence of buildings has a significant effect on the distribution and redistribution of radiation inside the urban canyon, due to

shading and radiative trapping (reflection). Although an infinite number of radiative reflections can be analytically resolved in a street canyon with homogeneous facets (Harman *et al.*, 2004), extension of the algorithm to urban canyon with sub-facet heterogeneity (see Figure 2.3) is not trivial and involves expensive matrix operations with large dimensions. It has been verified that a 2-reflection model is sufficient for typical urban surface temperatures and thermal properties (Wang, 2010) and is adopted here.

Inside the urban canyon, we define the normalized shadow length l_{shadow} as (Kusaka *et al.*, 2001):

$$l_{shadow} = \begin{cases} h \tan\theta_z \sin\theta_n & l_{shadow} < w \\ w & l_{shadow} \geq w \end{cases} \tag{4.1}$$

where h and w are the normalized building height and ground width respectively, r is the normalized roof width, with $r + w = 1$; θ_n is the difference between the solar azimuth angle and canyon orientation; θ_n is the difference between the solar azimuth angle θ_{sun} and canyon orientation θ_{can}, with

$$\cos\theta_{sun} = \left(\cos\theta_z \sin\phi - \sin\delta\right)\csc\theta_z \sec\delta \tag{4.2}$$

and θ_z is the solar zenith angle (Stull, 1998)

$$\cos\theta_z = \sin\phi\sin\delta - \cos\phi\cos\delta\cos\omega_t \tag{4.3}$$

Here ϕ is latitude (positive north), δ the solar declination and ω_t the solar hour angle (24 hour period), and

$$\omega_t = \frac{\pi t_{UTC}}{12} - \lambda; \qquad \delta = \phi_r \cos\left[\frac{2\pi(d_n - d_r)}{d_y}\right] \qquad (4.4)$$

where λ is the longitude (positive west); t_{UTC} is the Coordinated Universal Time in hours; ϕ_r is the latitude of the Tropic of Cancer ($22.45^\circ = 0.409\,\text{radians}$); d_n is the number of days of year (since 01 January); d_r is the day of the summer solstice (173); and d_y is the average number of days per year (365.25).

Assuming all surfaces are Lambertian (with isotropic scattering and reflection), for each urban facet, be it roof, wall or ground, the net shortwave radiation at each sub-facet is computed as:

$$S_{R,k} = \left(1 - a_{R,k}\right)\left(S_D + S_Q\right) \qquad (4.5)$$

$$S_{W,k} = \left(1 - a_{W,k}\right)\left(\begin{array}{l} S_D \dfrac{l_{\text{shadow}}}{2h} + S_Q F_{WS}\left(1 - a_{W,k}\right) + S_D \dfrac{w - l_{\text{shadow}}}{w} \overline{a}_G F_{WG} \\[2mm] + S_Q F_{WG} + S_D \dfrac{l_{\text{shadow}}}{2h} a_{W,k} F_{WW} + S_Q F_{WS} F_{WW} a_{W,k} \end{array}\right) \qquad (4.6)$$

$$S_{G,k} = \left(1 - a_{G,k}\right)\left(S_D \dfrac{w - l_{\text{shadow}}}{w} + S_Q F_{GS} + S_D \dfrac{l_{\text{shadow}}}{2h} \overline{a}_W F_{GW} + S_Q F_{WS} \overline{a}_W F_{GW}\right) \qquad (4.7)$$

where S_D and S_Q are the direct and the diffuse solar radiation received by a horizontal surface respectively; a is the surface albedo; subscripts 'S', 'R', 'W' and 'G' denote sky, roof, wall and ground facet respectively; numeric subscript $k = 1, 2, 3,...$ denotes the index of each sub-surface of a facet; and F_{ij} are the sky view factors computed as (Harman *et al.*, 2004):

$$F_{SG} = F_{GS} = \sqrt{1 + \left(\frac{h}{w}\right)^2} - \frac{h}{w} \qquad (4.8)$$

$$F_{WW} = \sqrt{1 + \left(\frac{w}{h}\right)^2} - \frac{w}{h} \qquad (4.9)$$

$$F_{GW} = 0.5\left(1 - F_{GS}\right) \qquad (4.10)$$

$$F_{WG} = F_{WS} = 0.5\left(1 - F_{WW}\right) \qquad (4.11)$$

Note that in Eqs. (4.6) and (4.7), the quantities $\bar{a}_G$ and $\bar{a}_W$ are the equivalent albedos of ground and wall facet respectively. Derivation of the equivalent albedos is as follows. Consider diffuse solar radiation, Ω_{ij}, originating from facet j and reflected off facet i (indices i, j can represent wall, ground, roof and sky). If facet j is heterogeneous and consists of N sub-surfaces, it can be written as

$$\Omega_{ij} = \left(1 - a_i\right)\left(\sum_{k=1}^{N} f_k a_{j,k}\right) F_{ji} S_Q = \left(1 - a_i\right)\bar{a}_j F_{ji} S_Q \qquad (4.12)$$

Therefore $\bar{a}_G = \sum_{k=1}^{N} f_k a_{G,k}$ and $\bar{a}_W = \sum_{k=1}^{N} f_k a_{W,k}$ where f_k is the area fraction of the kth sub-surface in a given facet G or W. Hereafter an equivalent quantity with an overbar is defined in the same manner as $\bar{a}_G$, unless otherwise specified. It is also noteworthy that in Eq. (4.12), all the N sub-surfaces are assumed to be uniformly distributed in space, such that the view factor F_{ji} is the same for each sub-facet of facet j, relaxing this assumption would significantly complicated the problem.

Similarly, using 2 reflections between urban facets, the net longwave radiation for each sub-surface can be calculated as:

$$L_R = \varepsilon_R \left(L^\downarrow - \sigma T_R^4 \right) \tag{4.13}$$

$$
\begin{aligned}
L_{W,k} &= \varepsilon_{W,k} \left(F_{WS} L^\downarrow + \overline{\varepsilon}_G F_{WG} \sigma \overline{T}_G^4 + \varepsilon_{W,k} F_{WW} \sigma T_{W,k}^4 - \sigma T_{W,k}^4 \right) \\
&+ \varepsilon_{W,k} \left(1 - \overline{\varepsilon}_G \right) F_{GS} F_{WG} L^\downarrow + 2 \left(1 - \overline{\varepsilon}_G \right) \varepsilon_{W,k} F_{GW} F_{WG} \sigma T_{W,k}^4 \\
&+ \varepsilon_{W,k} \left(1 - \varepsilon_{W,k} \right) F_{WS} F_{WW} L^\downarrow + \left(1 - \varepsilon_{W,k} \right) \overline{\varepsilon}_G F_{WG} F_{WW} \sigma \overline{T}_G^4 \\
&+ \varepsilon_{W,k} \varepsilon_{W,k} \left(1 - \varepsilon_{W,k} \right) F_{WW} F_{WW} \sigma T_{W,k}^4
\end{aligned}
\tag{4.14}
$$

$$
\begin{aligned}
L_{G,k} &= \varepsilon_{G,k} \left(F_{GS} L^\downarrow + 2 \overline{\varepsilon}_W F_{GW} \sigma \overline{T}_W^4 - \sigma T_{G,k}^4 \right) \\
&+ 2 \varepsilon_{G,k} \left(1 - \overline{\varepsilon}_W \right) F_{WS} F_{GW} L^\downarrow + \left(1 - \overline{\varepsilon}_W \right) \varepsilon_{G,k} F_{GW} F_{WG} \sigma T_{G,k}^4 \\
&+ 2 \varepsilon_{G,k} \overline{\varepsilon}_W \left(1 - \overline{\varepsilon}_W \right) F_{WW} F_{GW} \sigma \overline{T}_W^4
\end{aligned}
\tag{4.15}
$$

where ε is the emissivity, and σ the Stephan-Boltzmann constant.

4.1.2. Wind profile in urban canyon

Turbulent transport of energy depends largely on the wind profile in urban canopies. Above the roof mean wind profile follows the common log-law but varies exponentially within the canyon (Masson, 2000). The horizontal (along canyon) and vertical wind speed, integrated over 2π to average over all possible wind-canyon relative orientations, are determined by

$$U_{can} = \frac{2}{\pi} \exp\left(-\frac{1}{4} \frac{h}{w} \right) \frac{\ln\left(\dfrac{h/3}{z_{0,town}} \right)}{\ln\left(\dfrac{\Delta z + h/3}{z_{0,town}} \right)} \left| \mathbf{U}_a \right| \tag{4.16}$$

81

$$W_{can} = \sqrt{C_d}\,\left|\mathbf{U}_a\right| \qquad\qquad (4.17)$$

where $\mathbf{U}_a$ is the wind velocity, usually measured at the first atmospheric model level, $z_{0,town}$ is the roughness length of the urban area, $\Delta z = z_a - z_R$ is the height of the first atmospheric model level above the roof (or measurement height for offline implementations), with z_a the height of the atmospheric model level and z_R the height of the roof. The drag coefficient C_d, is computed from the temperature and humidity in and above the canyon (to account for stability following the formulation of Mascart *et al.* (1995), and from $z_{0,town}$. Note in Eq. (4.16) that integration over 360° is performed to eliminate the dependence of U_{can} on the wind direction of $\mathbf{U}_a$, assuming that the chance of occurrence of all wind directions is equally probable. Fig. 4.1 shows a histogram of wind direction distribution in the atmospheric layer during the period of 04-09 May 2010 (our first test period, as discussed in Section 4.3), measured by a Young wind monitor. It is clear that during this period, the prevailing wind direction is from the west and south-west (200°-300° with $0^o/360^o$ corresponding to north). While a preferable approach might be to develop a model for U_{can} that has a functional dependence on the wind direction in the atmospheric layer, especially for short and specific studies like the one we present here, this wind direction dependence is not included in any of the current urban canopy schemes. We keep this 360° averaging in our model since, practically, when the UCM is employed to study a relatively long period or a period with no prevailing wind direction, or a mix of canyons with random orientations, this integration is justified and needed.
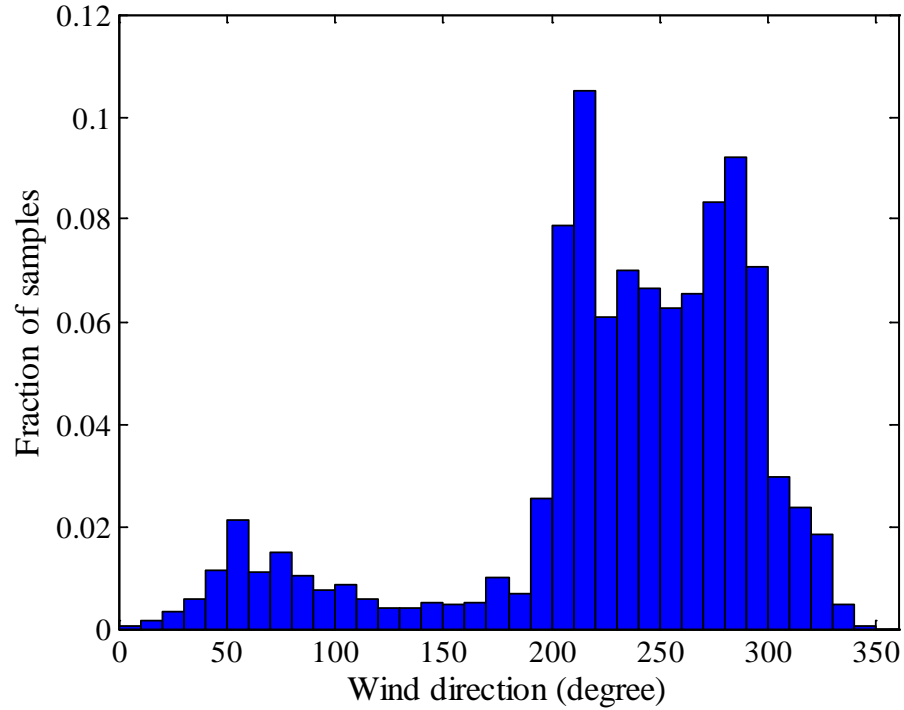
Figure 4.1: Histogram of wind direction distribution in the atmospheric layer during the

period of 04-09 May 2010, measured by Young wind monitor, with $0^{o}/360^{o}$

corresponding to the north

4.1.3. Turbulent fluxes in urban canyon

It can be seen from Figure 2.3 that there are two resistance networks for exchange of turbulent fluxes inside urban canopies: one inside the canyon where canyon facets (walls and ground) exchange energy with the canyon air and the other from the roof/canyon-top to the atmospheric layer. Inside the canyon, sensible heat for each sub-surface is parameterized as

$$H_{G,k} = \frac{c_p \rho_a \left(T_{G,k} - T_{can} \right)}{\text{RES}_G} \qquad (4.18)$$

$$H_{W,k} = \frac{c_p \rho_a \left(T_{W,k} - T_{can} \right)}{RES_W}$$ (4.19)

where RES is the aerodynamic resistance and c_p the specific heat of air.

Parameterization of latent heat flux inside the urban canyon is more complex. First of all, we assume that the contribution to latent heat from the wall is negligible since the water holding capacity of wall is insignificant, i.e.

$$LE_{W,k} = 0$$ (4.20)

Next consider the ground facet consisting of porous pavements with water holding capacity, bare soil and vegetation. For engineered (concrete, brick or asphalt) pavements,

$$LE_{G,eng} = \begin{cases} 0 & \text{for } \delta_w = 0 \\ \dfrac{\rho_a L_v \left(q^*_{G,eng} - q_{can} \right)}{RES_G} & \text{for } \delta_w > 0 \end{cases}$$ (4.21)

where q is the specific humidity, superscript star denotes the saturated specific humidity at given surface temperature and δ_w is the actual depth of retained water film/layer on the engineered surfaces for which a prognostic equation, presented later, is solved. Note that Masson (2000) developed specific evaporation schemes for roofs and ground surfaces partially covered with snow, similar to the formulation for water-holding pavements in Eq. (4.21) but not included in the single-layer WRF-UCM by Kusaka *et al.* (2001).

For natural surfaces, viz. bare soil or vegetation, the parameterization scheme for latent heat follows Brutsaert (2005):

$$LE_{nat} = L_v \beta_e E_{p,nat}$$ (4.22)

where β_e is a reduction factor as a function of soil water content. For vegetation, $\beta_e = 1.0$ and for bare soil:

$$\beta_e = \begin{cases} 1.0 & \text{for } \theta > \theta_s \\ (\theta - \theta_r)/(\theta_s - \theta_r) & \text{for } \theta \le \theta_s \end{cases} \tag{4.23}$$

with θ the volumetric soil water content, θ_s the soil water content at saturation and θ_r the reference soil water content at which evaporation is suppressed. And the potential evaporation rate is again given by the resistance method, as

$$\begin{aligned} E_{p,nat} &= \frac{\rho_a \left(q_{G,nat}^* - q_{can} \right)}{\mathrm{RES}_G} && \text{for bare soil} \\ E_{p,nat} &= \frac{\rho_a \left(q_{G,nat}^* - q_{can} \right)}{\mathrm{RES}_G + R_s} && \text{for vegetation} \end{aligned} \tag{4.24}$$

where R_s is the stomatal resistance of vegetation. Here we use the parameterization scheme derived based on meteorological approach (cf. physiological approach), by relating the stomatal resistance to meteorological variables including solar radiation, soil water availability, vapor pressure deficit and air temperature (Noilhan and Planton, 1989; Niyogi and Raman, 1997):

$$R_s = R_{s,\min} F_{SR} F_\theta F_e F_T / \mathrm{LAI} \tag{4.25}$$

where $R_{s,\min}$ is the minimum stomatal resistance depending on the vegetation type, LAI is the leaf area index, and F_{SR}, F_q, F_e and F_T are the adjusting factors for the solar radiation, soil water content, vapor pressure deficit and temperature, respectively.

The aerodynamic resistance between canyon facets and air is given by (Masson, 2000):

85

$$RES_G = RES_W = \left(11.8 + 4.2\sqrt{U_{can}^2 + W_{can}^2}\right)^{-1} \qquad (4.26)$$

4.1.4. Fluxes from canyon and rooftop to the atmosphere

From the canyon air to the atmospheric layer, turbulent fluxes are given by

$$H_{can} = \frac{c_p \rho_a \left(T_{can} - T_a\right)}{RES_{can}} \qquad (4.27)$$

$$LE_{can} = \frac{L_v \rho_a \left(q_{can} - q_a\right)}{RES_{can}} \qquad (4.28)$$

and from the roof top to the atmospheric layer the turbulent heat exchange is given by:

$$H_R = \frac{c_p \rho_a \left(T_R - T_a\right)}{RES_R} \qquad (4.29)$$

$$LE_R = \beta_e \frac{L_v \rho_a \left(q_R^* - q_a\right)}{RES_R} \qquad (4.30)$$

The coefficient β_e follow Eq. (4.21) for conventional roofs and Eq. (4.23) for green roofs. Aerodynamic resistances RES_R and RES_{can} are computed using Monin-Obukhov similarity theory. To reduce the computation cost needed for numerical iterations, here we use a set of closed-form flux-profile relation derived by Mascart *et al.* (1995), as shown in Appendix B.

4.1.5. Total turbulent fluxes and canyon temperature and humidity

The total turbulent heat fluxes from the urban area to the atmospheric layer, are then given by the summation of turbulent heat fluxes from roofs and canyons,

$$
H_u = r \sum_{k=1}^{N_R} f_{R,k} H_{R,k} + w H_{can} \tag{4.31}
$$

$$
LE_u = r \sum_{k=1}^{N_R} f_{R,k} LE_{R,k} + w LE_{can} \tag{4.32}
$$

where N_R is the number of sub-surfaces on the roof facet. The canyon temperature and humidity, T_{can} and q_{can} are computed by the energy and humidity balance inside the canyon, by enforcing that

$$
H_{can} = \frac{2h}{w} \sum_{k=1}^{N_W} f_{W,k} H_{W,k} + \sum_{k=1}^{N_G} f_{G,k} H_{G,k} \tag{4.33}
$$

$$
LE_{can} = \sum_{k=1}^{N_G} f_{G,k} LE_{G,k} \tag{4.34}
$$

where N_W and N_G are the number of sub-surfaces of wall and ground, respectively. Combining with Eqs. (4.27), (4.28) and the parameterizations of turbulent fluxes inside the urban canyon, Eqs. (4.33) and (4.34) can be solved as

$$
T_{can} = \frac{T_a / \text{RES}_{can} + (2h/w)(\bar{T}_W / \text{RES}_W) + \bar{T}_G / \text{RES}_G}{1 / \text{RES}_{can} + (2h/w)(1 / \text{RES}_W) + 1 / \text{RES}_G} \tag{4.35}
$$

$$
q_{can} = \frac{q_a / \text{RES}_{can} + \bar{q}_G / \text{RES}_G}{1 / \text{RES}_{can} + 1 / \text{RES}_G} \tag{4.36}
$$

In addition to the above parameterization schemes, the spatially-analytical scheme using Green's function approach, present in Chapter 2 and Appendix A, is adopted for evaluating the surface temperatures and conductive heat flux for each urban sub-facet individually.

4.2. Urban hydrological model

Evaporation and transport of water/moisture have been inadequately resolved in existing urban canopy models (Grimmond *et al.*, 2010). This can be attributed to the lack of incorporation of simple but adequate urban hydrological models. In particular, evaporation from engineered pavements, such as asphalt and concrete, and its cooling effect have long been ignored in most urban models (Nakayama and Fujita, 2010), albeit some models account for it in alternative ways, e.g. Masson (2000) included snow cover on impervious pavements. In this section, we detail the integration of hydrological models for both natural (bare soil and vegetation) and engineered (concrete, asphalt, gravel, *etc.*) surfaces in the UCM.

4.2.1. Prognostic equation for volumetric water content

In the hydrological model of natural surfaces, the prognostic equation for the volumetric soil moisture content θ is given in the 1D vertical diffusive form of Richard's equation, derived from Darcy's law (Hanks, 1992):

$$\frac{\partial \theta_{nat}}{\partial t} = \frac{\partial}{\partial z}\left(D\frac{\partial \theta_{nat}}{\partial z} + K + F_\theta \right) \tag{4.37}$$

where D is the soil water diffusivity; K is the hydraulic conductivity; F_θ represents source and sink terms, i.e. $F_\theta = P + Q_F - R - E$, with precipitation P, evaporation E for bare soil or evapotranspiration ET for vegetation, surface runoff R and anthropogenic water Q_F. Soil moisture is solved by vertically discretizing the soil layer, see Figure 4.2(a) and rewriting Eq. (4.37) in the form:

$$\frac{\partial \theta_1}{\partial t} = \frac{1}{d_1}\left(P + Q_F - E - R - Q_{w,1\to 2} \right) \qquad \text{for layer 1} \tag{4.38}$$

$$\frac{\partial \theta_k}{\partial t} = \frac{1}{d_k}\left(Q_{w,k-1\to k} - Q_{w,k\to k+1} \right), \qquad \text{for layer } k > 1 \tag{4.39}$$

where d_k, $k = 1, 2, 3,\ldots$ is the thickness of the kth sublayer. $Q_{w,k\to k+1}$ is the water infiltration through the interface between k^{th} and $(k + 1)^{\text{th}}$ soil layers:

$$Q_{w,k\to k+1} = \bar{D}_{k,k+1}\frac{\theta_k - \theta_{k+1}}{(d_k + d_{k+1})/2} + \bar{K}_{k,k+1}, \qquad 1 \le k < N \tag{4.40}$$

with averaged hydraulic properties defined as

$$\bar{D}_{k,k+1} = \frac{d_k + d_{k+1}}{d_k / D_k + d_{k+1} / D_{k+1}}, \quad \bar{K}_{k,k+1} = \frac{d_k + d_{k+1}}{d_k / K_k + d_{k+1} / K_{k+1}} \tag{4.41}$$

And the lower boundary condition is assumed to be a zero-flux surface

$$Q_{w,N\to N+1} \equiv 0 \tag{4.42}$$

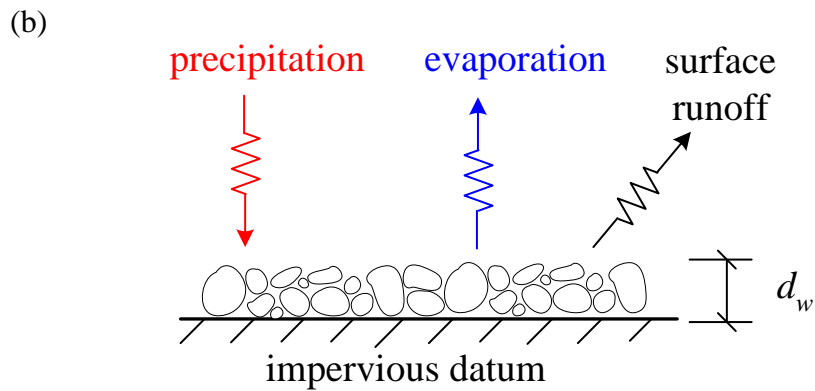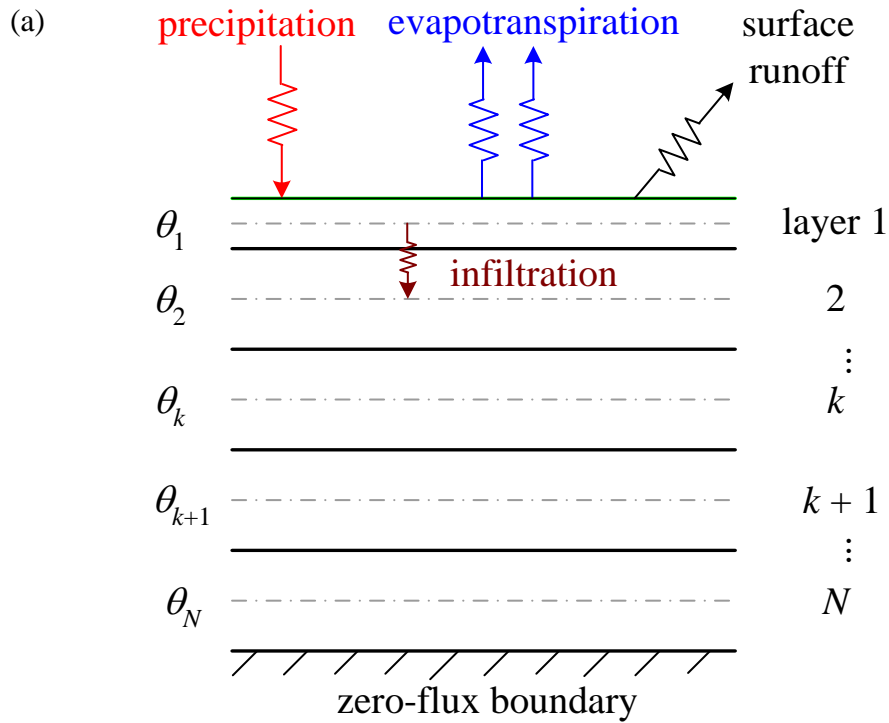where N is the total number of discrete sublayers.

Figure 4.2: Schematic hydrological models for (a) natural surfaces, and (b) engineered pavements in urban areas. The soil in (a) is vertically discretized to capture the variation of hydraulic properties of unsaturated soils. In (b), d_w is the maximum water-holding depth of porous engineered materials

The surface evaporation term in Eq. (4.38) can be evaluated from the latent heat defined in the previous section for each urban sub-facet consisting of bare soil or vegetation. Note that in Section 4.1, the evaporation (latent heat) is expressed as a function of soil moisture content, thus these two quantities are strongly coupled and the solutions of the two equations require numerical iteration.

For engineered pavements, it is assumed that there exists a water-holding layer above the impervious datum, as shown in Figure 4.2(b). The prognostic equation for the actual depth of water retention δ_w can be written as

$$\phi_{eng} \frac{\partial \delta_w}{\partial t} = P - E_p - R \tag{4.43}$$

where ϕ_{eng} is the surface porosity of engineered materials and E_p is the potential evaporation rate, which can be computed from Eq. (4.21).

4.2.2. Hydraulic properties for unsaturated soils

Determination of water infiltration within the soil layer, as shown in Eq. (4.40), is dictated by the soil water diffusivity D and the hydraulic conductivity K, which are highly nonlinearly related to soil moisture. Both D and K can vary several orders of magnitude even for very small change in soil moisture, particularly when the unsaturated soil is relatively dry (van Genuchten, 1980). The high nonlinearity of unsaturated hydraulic properties, together with the large variation of soil moisture from soil surface to the flux-free boundary, precludes analytically tractable solutions to the prognostic

equation in (4.37), compared to the analytical procedures in Chapter 2 for temperatures and heat fluxes.

It was shown by Cuenca *at al.* (1996) that for bare soils, the parameterization of soil water has significant effect on the partitioning of surface energy into sensible and latent heat. While there are numerous existing and ongoing research efforts focusing on the determination of the functional relation between the soil water content and the unsaturated soil hydraulic properties, in this study, we adopt the widely-used empirical model developed by Clapp and Hornberger (1978) and Cosby *et al.* (1984)

$$K(\theta) = K_s \left(\frac{\theta}{\theta_s} \right)^{2b+3} \tag{4.44}$$

$$D(\theta) = -K(\theta) \frac{\partial \psi}{\partial \theta} \tag{4.45}$$

$$\psi(\theta) = \psi_s \left(\frac{\theta_s}{\theta} \right)^b \tag{4.46}$$

where K_s is the saturation hydraulic conductivity, ψ the soil tension function, ψ_s the saturation soil suction, and b a fitting parameter dependent on soil type.

4.2.3. Anthropogenic heat and water

Urban models involve unique sources of heat and moisture due to human activities. The so called "anthropogenic stressors" (Fernando, 2010) result from sources of emission including human metabolism, HVAC systems in buildings, industry and power plants. Anthropogenic heat and moisture inputs vary significantly both in space

and time, of which measurements are not readily available in most cities. Grimmond *et al.* (2010), based on the results of international urban energy balance models comparison project, concluded that the omission of anthropogenic water have great contribution to the inadequacy of current urban canopy models in predicting evaporation and latent heat budget. Masson (2000) argued that anthropogenic heat release does not directly modify the surface energy balance, but rather affects the atmospheric budgets.

A review of methods for estimating anthropogenic heat and moisture in the urban environment indicated that a combination of inventory method and simplified building energy method is needed at the current stage of practice (Sailor, 2011). Due to limited measurement data available, we do not explicitly incorporate the anthropogenic components H_F and Q_F component in the energy balance and hydrological equations, respectively. Inclusion of these terms is relatively similar to an increase in a local forcing term in urban canopies, and is effect is implicitly lumped into the measurement of meteorological forcing terms such as the atmospheric temperature and specific humidity by eddy covariance stations.

4.3. Model validation

In this section, we validate the new UCM with coupled energy and hydrology models, again using field measurements by SNOP. For quality control of the EC data, here we restrict our analysis to wind angle within ±150 degrees from the sonic axis to avoid measurements influenced by the mast.

Lists of input parameters for canyon dimension and material properties are shown in Tables 2.1 and 2.2, respectively. The soil hydraulic properties in Table 2.2 are adopted from Chen and Dudhia (2001) for sandy loams, which are typical for soils used in urban lawns. Values of thermal properties in Table 2.2 are calibrated to give optimal output for the 24 hour period on 05 May 2010 (See Chapter 2, Section 2.2.3). Once determined, the same set of thermal parameters is fixed for the rest of the test period to assess the robustness of the model and the calibrated values.

The first validation test consists a period of 6 days: 04 to 09 May 2010, which covers different weather conditions, including clear (05 and 07 May), cloudy (04 and 06 May), overcast (09 May) and light rainy (08 May) days. Results of comparison between UCM predictions and measurements of surface temperatures, net radiation, turbulent fluxes and soil water content are shown in Figures 4.3 to 4.7. It is clear from Figure 4.3 that the new UCM, with sub-facet resolution and an advanced scheme of computation surface temperature (Wang *et al.*, 2011a) is able to capture the differences in surface temperature evolution for heterogeneous urban sub-facets. The UCM predicts surface temperatures for 4 sub-facets with significantly different material thermal properties, viz. gravel roof, asphalt pavement, concrete pavement and lawn, with good accuracy as compared to the field measurements. Figure 4.4 shows that it also reproduces the net radiation over the roof well. This is not surprising since the radiative balance depends on the surface albedo, emissivity and skin temperatures, which are either well calibrated (albedo and emissivity) or well predicted by the UCM (skin temperatures, c.f. Figure 4.3).
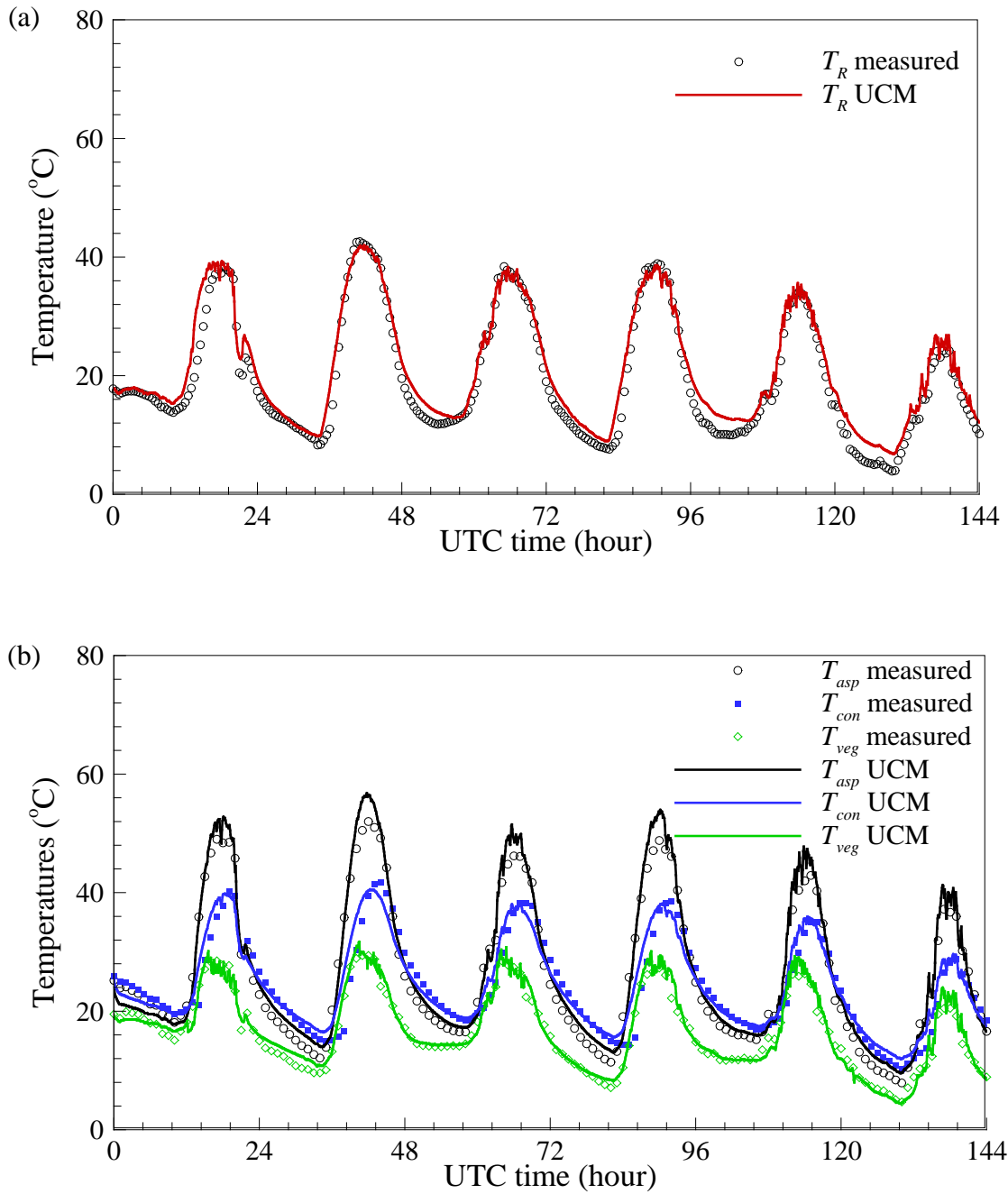
Figure 4.3: Comparison of UCM prediction and measurement of surface temperatures for

(a) gravel roof, and (b) heterogeneous ground with asphalt and concrete pavements and

vegetation, on 04-09 May 2010
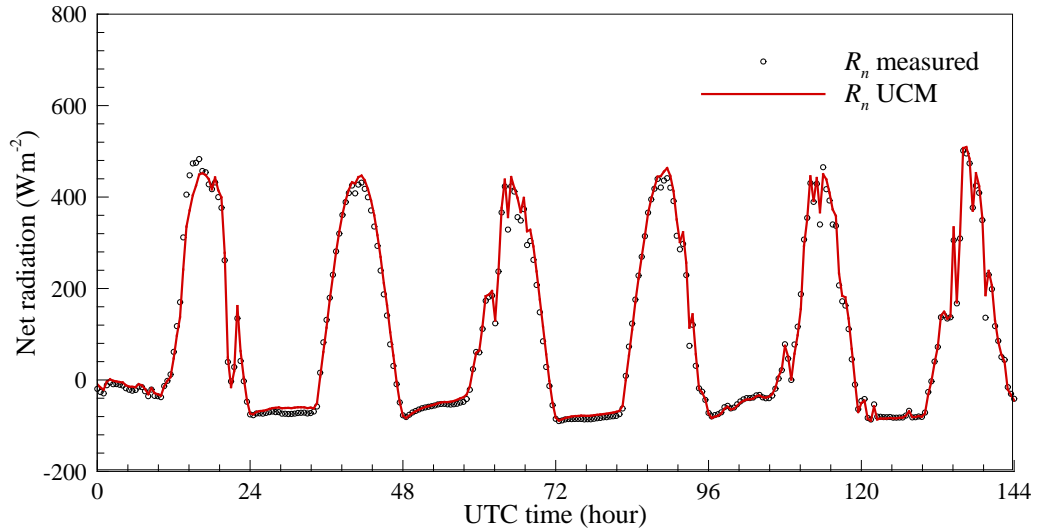
Figure 4.4: Comparison of UCM prediction and measurement of net radiation, on 04-09

May 2010

Turbulent heat fluxes, on the other hand, are much more challenging to be accurately parameterized, in particular, the latent heat flux associated with evaporation from urban surfaces. In addition, accurate measurements of these fluxes in urban areas can also be affected by surface heterogeneity, the presence of a roughness sublayer (typically 2 to 3 times the building height), heavy precipitation, and other factors. The EC station used in this study is located 4.33 m above the rooftop (the highest rooftop in the adjacent built area), which is not extended sufficiently high to be above the roughness sublayer. As a consequence of possible bias due to roughness elements, the measurement accuracy might not be very high. On the other hand, there is an advantageous aspect to this setup since the low EC measurements have a small footprint and are only representative of the immediate surrounding of our test site. Thus as a trade-off of the reduced accuracy, measured turbulent fluxes are mainly affected by the area of the campus whose parameters are used in the model, which is desirable. In Figure 4.5, for the

test period of 6 days, the prediction of sensible and latent heat fluxes by the UCM is in general in good agreement with measured data, albeit the discrepancy is understandably larger than the temperature and net radiation results. It is noteworthy that at around 114 hours there was a small rain event (0.25 mm) and the model captures the relatively high latent heat flux maintained during and after the precipitation, mostly due to evaporation from engineered pavements (70% of the total ground surface area).

We emphasize again that the main source of discrepancy in the comparisons of turbulent fluxes is related to the low elevation of the EC station and the differences between the EC footprint and the study area represented by our model. Changing the EC measurement height will improve one of these aspects while deteriorating the other; but the trends are comparable and their agreement is convincing. In addition, the accuracy of turbulent EC measurements is not very good when the measured sensible or latent heat is low. Comparison of the Bowen ratio (H/LE) between UCM prediction and EC measurements is shown in Figure 4.6, where blue circles represent data points with measured H or LE less than 10 W m^{-2}, and the remaining data points are in red. It is clear that, despite the scatter, the UCM predictions and "good" EC measurements of the Bowen ratio follow the 1-to-1 line trend reasonably well, while points with measured H or LE less than 10 W m^{-2} are further off the 1-to-1 line.

Figure 4.5: Comparison of UCM prediction and measurement of (a) sensible heat and (b)

latent heat fluxes, on 04-09 May 2010
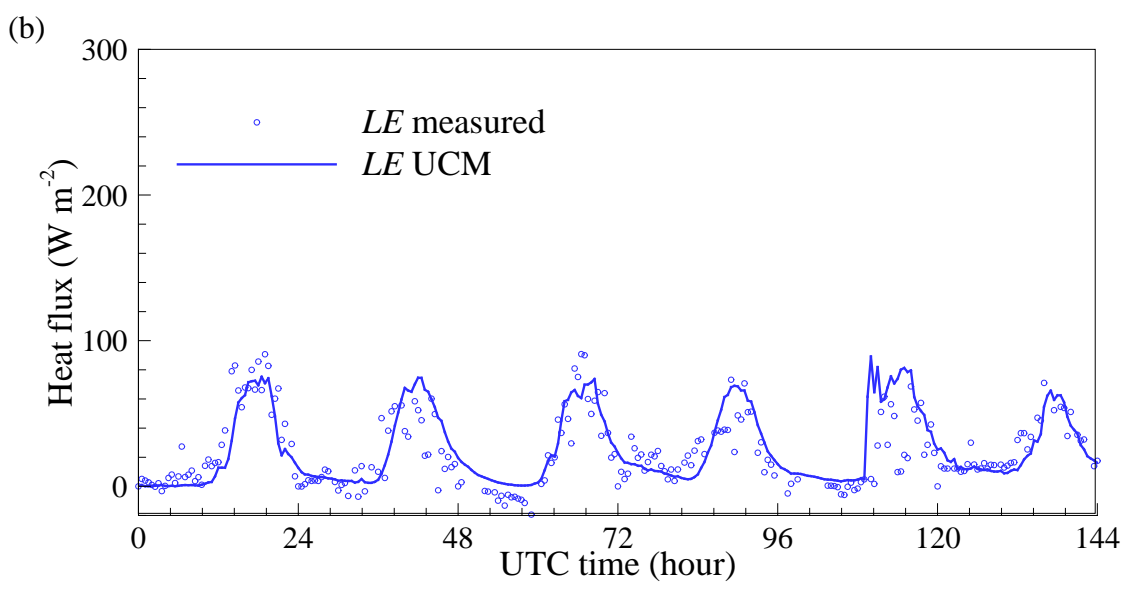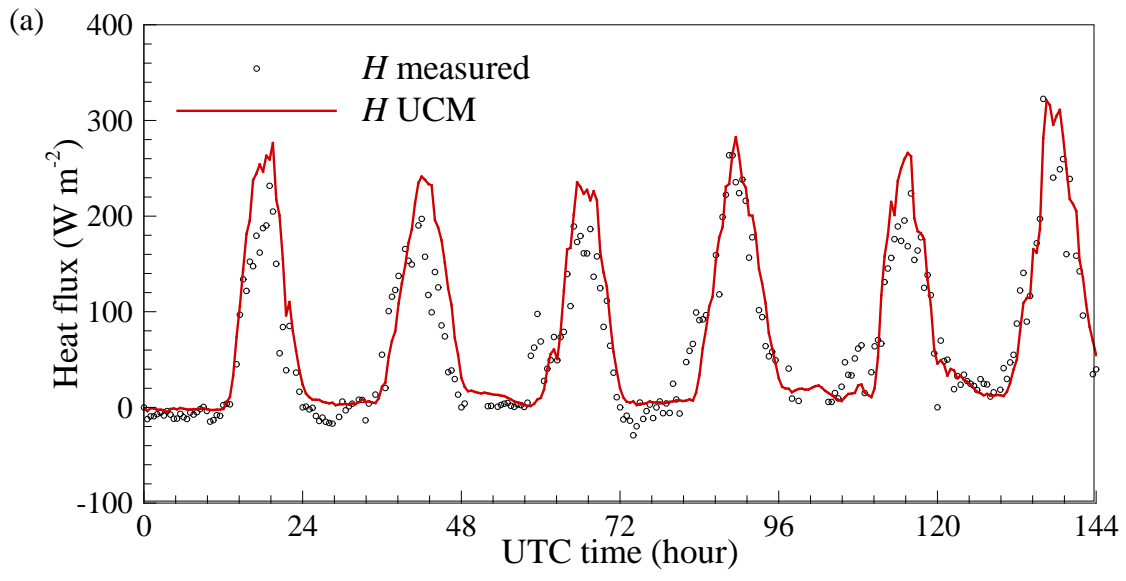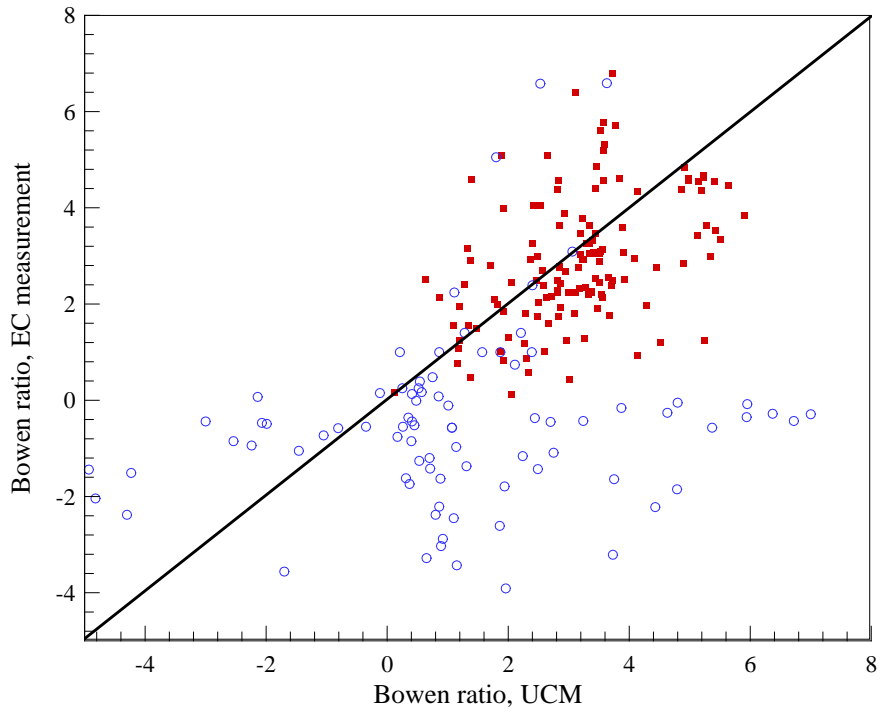
Figure 4.6: Comparison of UCM prediction and measurement of Bowen ratio, on 04-09

May 2010
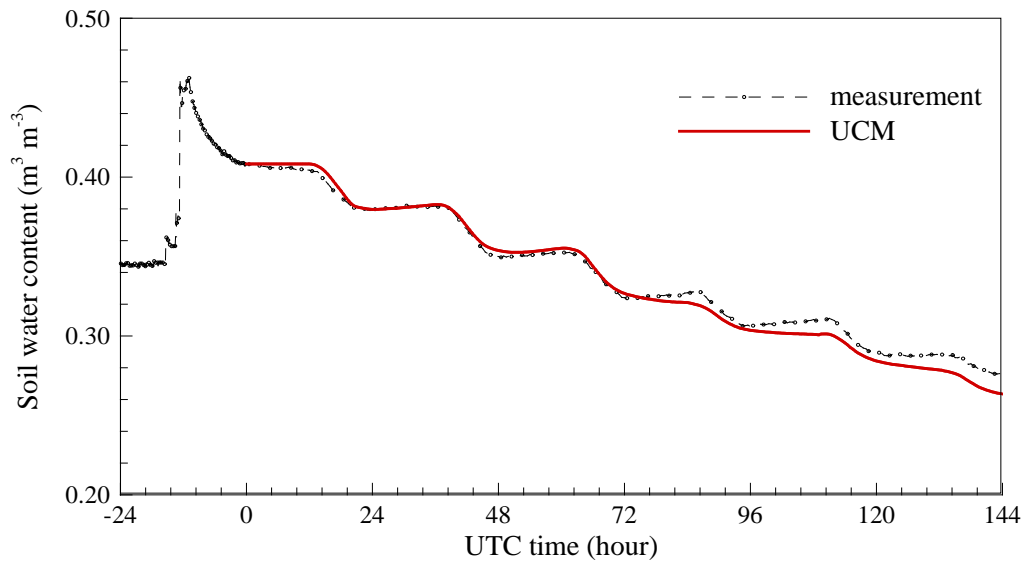
Figure 4.7: Comparison of UCM prediction and measurement of volumetric soil water

content, on 04-09 May 2010

The soil volumetric water content (VWC) was measured as a lumped value along the first 5 cm of the soil using EC-TM probes manufactured by Decagon Devices, Inc. The measured soil moisture is sensitive to variation of soil temperature. Thus VWC measurements are corrected by multiple regression analysis using 3 days' data (with each day from May, July and October of 2010 respectively to cover seasonal variability) (Cobos and Campbell, 2007). The corrected VWC is given by:

$$\theta_{corrected} \ (\text{in } \%) = 0.943\theta_{measured} - 8.502 \times 10^{-2} T_{soil} + 3.936 \qquad (4.47)$$

The R^2 value for the linear regression is 0.95, indicating a good quality of the statistical analysis. In Figure 4.7, the model prediction of the volumetric soil water content is compared with the measurements by the wireless stations. Note that there was a precipitation event on 03 May 2010, i.e. on the day immediately before our study period. The soil moisture was hence replenished prior to the test period. For the first 3 days, 04-06 May 2010, when the soil saturation was relatively high (> 60%), the model predicts the soil moisture with good accuracy. During the last 3 days, when the soil was relatively drier, UCM slightly overestimated the evaporation (c.f. Figure 4.5, especially on days 4 and 5) and thus predicts lower soil moisture content as compared to measured values. This observation apparently suggests that the discrepancy source could be an overestimation of the evaporation which dries the soil, rather than an overestimation of downward water flux in the soil layers. Note that in the current setting, we have only one lumped measurement of the soil moisture of urban lawns through the first few centimetres of the soil surface layer. To further validate the urban hydrology model

proposed here, it is desirable to have a vertical measurement of the soil moisture profile from surface through an adequate depth of the soil, preferably down to, say 2 m deep.
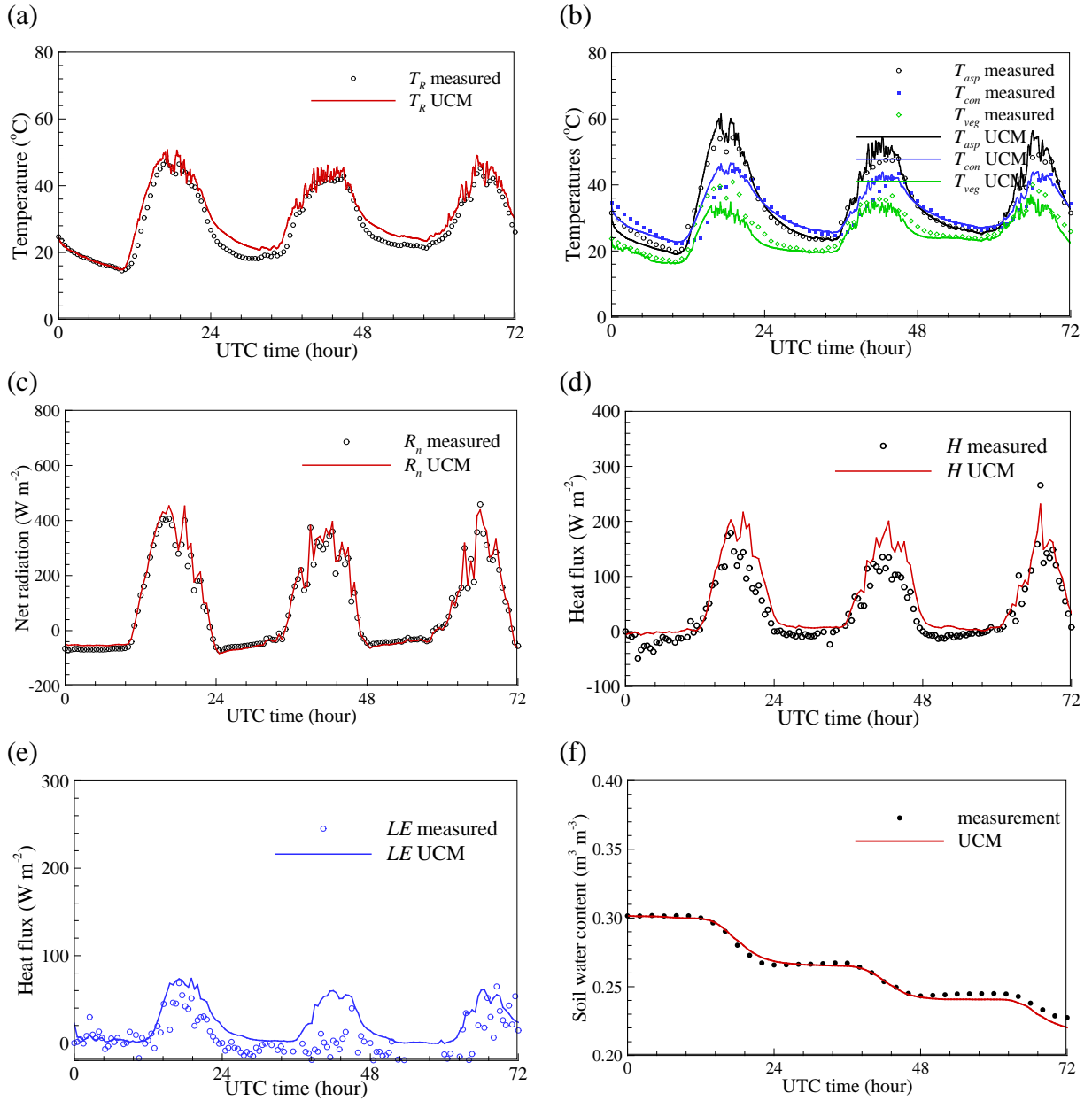
Figure 4.8: Comparison of UCM prediction and measurement of (a) roof temperature, (b) ground surface temperatures, (c) net radiation over the roof, (d) sensible heat, (e) latent heat, and (f) volumetric soil water content, on 27-29 July 2010

The validation above illustrates the good performance of the new UCM for a period of 6 days under different weather conditions, including clear, cloudy, overcast and light rainy days. To investigate the applicability of the model to different seasons, a second test period was selected for a 3 relatively hotter and drier days, viz. 27-29 July 2010. Input parameters, identical to those used in the first test period in May, were applied to this case study. Results of comparison between UCM predictions and measurements of surface temperatures, net radiation, turbulent fluxes and soil water content are shown in Figure 4.8. It can be seen that the accuracy of UCM predictions, when applied to a different season and meteorological conditions, are maintained for all the quantities compared to field measurements. The latent fluxes remain the least adequately predicted output for the same reasons discussed above. A large extent of relatively homogeneous urban canopy is needed to overcome the difficulty with turbulent flux validation, in which an EC station can then be setup at higher elevation and can measure a larger footprint with better statistically convergence.

4.4. Case study for UHI mitigation

A useful feature of the UCM, coupled with urban hydrological model, lies in its ability to assess different strategies for mitigation of the well-known UHI effect in cities, such as green (i.e. vegetated) roofs or white (highly reflective) roofs . Since our new UCM is able to capture sub-facet heterogeneity of building roofs, together with the hydrological model for urban soils, it can be readily extended to study the effect of increasing surface albedo (white roof) versus evaporative cooling (green roof) in

reducing roof surface temperatures as well as in redistributed partitioning of energy fluxes for UHI mitigation. Here we present a case study comparing such option for our first validation period.

In Figure 4.9(a), roof temperatures are evaluated using various surface albedos, i.e. a_R = 0.1, 0.5 and 0.9 respectively. Increase of surface albedo induced significant reduction in roof surface temperatures, under all weather conditions. Temperature reduction as large as 30 ^{o}C around noon can be accomplished by increasing a_R from 0.1 to 0.9. This implies that white roofs, with high surface albedo, is effective in reducing UHI by reducing sensible heat transfer from roof to the atmosphere and reduced heat storage inside the urban canopies. This also have a positive impact on the cooling loads of the building since a significant fraction of the incoming solar radiation is simply reflected back in this case. On the other hand, a green roof, with a relatively low surface albedo a_R = 0.15, can effectively reduce surface temperature (c.f. a_R ~ 0.2-0.4 for conventional roof) through evaporative cooling. Note that the results in Figure 4.9 were obtained by taking the atmospheric forcing and surface parameters for 04-09 May 2010, same as in our first case study. An interesting observation is that during simulation of the first 3 days, soil moisture retained by roof vegetation was relatively high, thus sufficient evaporation occurred and kept the roof surface temperature of the green roof lower than that of a roof with a_R = 0.5. During the last 3 days, when soil moisture dwindled rapidly, the effectiveness of green roof in reduction of roof temperature was significantly reduced. Particularly in the last 48 hours, surface temperature of green roof is comparable to a roof with a_R = 0.1, indicating that the evaporative cooling effect of green roof is nearly suppressed for dry soil. However one can also study the effect of irrigated green roofs

using the same framework. An alternative way to assess the UHI mitigation though evaporative cooling is through the partitioning of latent, sensible and conductive fluxes, e.g. using the Bowen ratio H/LE for the entire urban area (not limited to the roof fraction). In Figure 4.9(b), time series of Bowen ratio was plotted by comparing a green roof with a conventional roof with $a_R = 0.3$. Again it is clear that for the first 4 days of simulation, the green roof is effective in reducing Bowen ratio, by redistributing sensible heat to latent heat through evaporative cooling effect. As the soil moisture content approaches the residual value, evaporation through green roof is greatly reduced through increase in stomatal resistance and the lower albedo of the green roof in this comparison results in higher sensible heat fluxes towards the end of the our study period.

The simple case study presented in this section highlighted a couple of interesting features of the new UCM developed in this study. First, by coupling a relatively detailed urban hydrological model to the energy balance model, the new UCM is capable of physically simulating urban surface exchange processes, in particular, those associated with vegetated surfaces in urban areas. Therefore, it is applicable to assess different primary UHI mitigation strategies, such as green versus white roofs. Secondly, vegetated surfaces, not limited to green roof, are in general very effective in reducing urban surface temperature and redistributing turbulent heat transport through evaporative cooling, provided they are well irrigated. Otherwise, the relatively low surface albedo of green grass and other short vegetation (0.15-0.25, according to Brutsaert, 2005) increases heat absorbing and has a potential adverse effect on UHI. This is partially illustrated also in our measurements where towards the end of the first test period, the differences in peak temperatures between the vegetated and concrete ground surfaces is significantly reduced

as the soil moisture and evaporation from the green surfaces are reduced, though ground vegetated surfaces maintain more available moisture compared to the usually thin green roof covers.
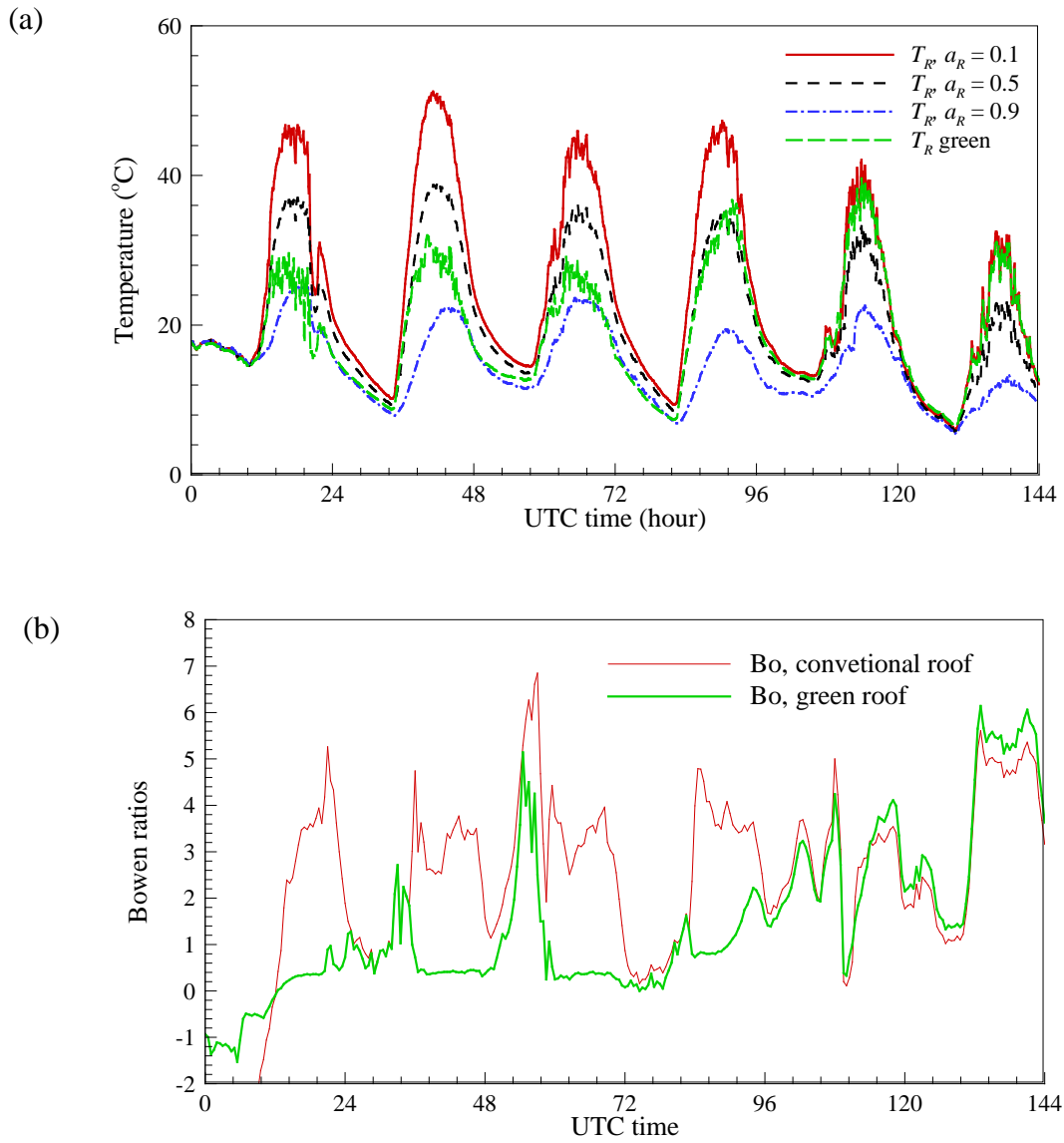
(a)

(b)

Figure 4.9: Comparison of (a) roof surface temperatures with various surface albedos and green roof ($a_R = 0.15$), and (b) Bowen ratio with conventional ($a_R = 0.3$) and green roof, both cases driven by the atmospheric forcing on 04-09 May 2010

4.5. Concluding remarks

Physically-based surface exchange schemes for mass and energy transport in urban canopies are complex due to the wide range of processes controlling urban land surface-atmosphere interactions. Accurate parametrization of the latent heat exchanges are particularly difficult due to the lack of adequate parameterizations of urban hydrological processes. As urban field measurements and modelling studies increasingly confirm the importance of the inclusion of vegetation cover in urban canopy schemes for improving model performance (Grimmond *et al.*, 2011), the coupling of water/moisture transport schemes from urban surfaces to the energy transport schemes remains a big modeling challenge. The widely used urban canopy schemes, for example those adopted in the WRF model (including both single-layer and multi-layer ones), are still not very realistic in terms of their physical representation of these coupled transport processes, despite the continuous improvement in model parameterizations and the increasing model complexity in the last decade. The only exception is the vegetated UCM developed by Lee and Park (2008) and Lee (2011), which included a very brief description of the hydrological modeling for tall trees and grass surface inside urban canyon while leaving the subsurface transport of water invalidated.

In this chapter, we attempted to address some practical difficulties by developing a new urban surface exchange scheme with coupled energy transport and hydrological model. The new UCM also improves upon current urban models through the inclusion of simple but sufficient hydrological processes, not only for urban vegetation cover (e.g. as in Lee and Park, 2008; Lee, 2011), but also for bare soils and porous engineered surfaces.

The skill of the new scheme was tested against experimental data collected through a wireless sensor network deployed over the campus of Princeton University. Surface temperatures as well as net radiation measurements over the roof were captured very well since they largely depend on surface parameters that we calibrated for. Surface fluxes were more challenging to capture with high accuracy, probably due mainly to footprint mismatch, but the trends were reproduced by the model rather well. The model performance was found to be robust and insensitive to changes in weather conditions or seasonal variability. Predictions of the volumetric soil water content were also in good agreement with field measurements. It highlighted the model capability of capturing subsurface water transport for urban lawns, though some divergence towards the end of the modelling period suggests that weekly re-initialization of the soil moisture either through measurements or automatically after a storm might be beneficial. Also note that here we mainly focused on short urban vegetation, i.e. lawns and green roofs. In the future development of this model, effect of tall trees on energy balance (shading effect in urban canyon) as well as hydrological processes will be incorporated.

With this new and improved scheme, it is possible to apply the model to many applications in urban environmental studies with different problem settings. One interesting example, as we illustrated through a case study, is the assessment of potential mitigation strategies of UHI using green or white roofs. Our case-study illustrates that the while white roofs are consistently beneficial, green roofs need to be watered regularly to keep their cooling effect active.

Chapter 5

Conclusions and perspectives

We presented in this dissertation a comprehensive effort focused on the development, validation and application of new surface exchange schemes for energy and water/moisture in urban canopies. Research tools used in this study involve analytical procedures, numerical modeling, statistical simulations as well as experimental measurements. The single-layer urban canopy model used in WRF is adopted in this study for representation of building arrays, for its simplicity and capacity to capture the essential physics of transport of energy and water/moisture in urban canopies. To develop better parameterization schemes in UCM, we first generalized the canyon representation to incorporate sub-facet heterogeneity in each urban facet, be it roof, wall or ground surface. Due to the fact that urban surface is highly non-homogeneous, resolution of the sub-facet heterogeneity is crucial for improving the model performance, in particular for capturing the exchange processes occurring over urban vegetation more accurately.

Next we derived a spatially-analytical algorithm for computation of surface temperatures and conductive heat fluxes through solid media. Detailed comparison of this analytical procedure against ideal and real cases showed its advantage over the conventional fully discrete (finite difference) schemes and its applicability in UCM. The analytical procedure can be readily extended to reconstruct the ground heat flux at soil surfaces via measurements at a depth inside soils and without relying on the knowledge

of soil temperature profiles. This extension has practical implication in contributing to solve the famous surface energy balance closure problem over bare soil surfaces.

While uncertainty is ubiquitous in parameter space of any numerical model, it is of paramount importance for us to quantify the model sensitivity to the uncertainty inherent in the input parameters. We adopted an advanced Markov Chain Monte Carlo (MCMC) procedure, the Subset Simulation, to analyze the sensitivity of the single-layer UCM statistically. Results show that critical heat exchange between urban areas and the atmosphere is largely modulated by the presence of buildings and their thermal properties, while impervious pavement or vegetated ground have a relatively lower impact. Model output of both critical heat fluxes and surface temperature are highly sensitive to the uncertainties in urban geometry, characterized by the normalized building height and roof width.

In Chapter 4, we presented detailed parameterization schemes for the transport of both energy and water/moisture inside urban canopies. In addition to solving the energy balance equation, our UCM resolved the transport of water/moisture for both vegetated and water-holding engineered surfaces. We developed urban hydrological models for individual sub-facets and solved prognostic equations for subsurface water transport. The focus was to couple the surface exchange of energy and water through the evapotranspiration process and the latent heat, a major component of the energy balance dependent on the water availability, which is in turn dictated by the subsurface transport of moisture in porous media. Numerical predictions by the new UCM highlighted the importance of coupling urban hydrological models with energy exchange schemes. The new UCM proved suitable and accurate in resolving the urban land-atmosphere

interactions and can be readily extended to many practical applications. Examples include evaluation of the existing mitigation strategies of urban heat island through adopting white roofs or green roofs and study of urban climatology based on the daily average prediction of the UCM.
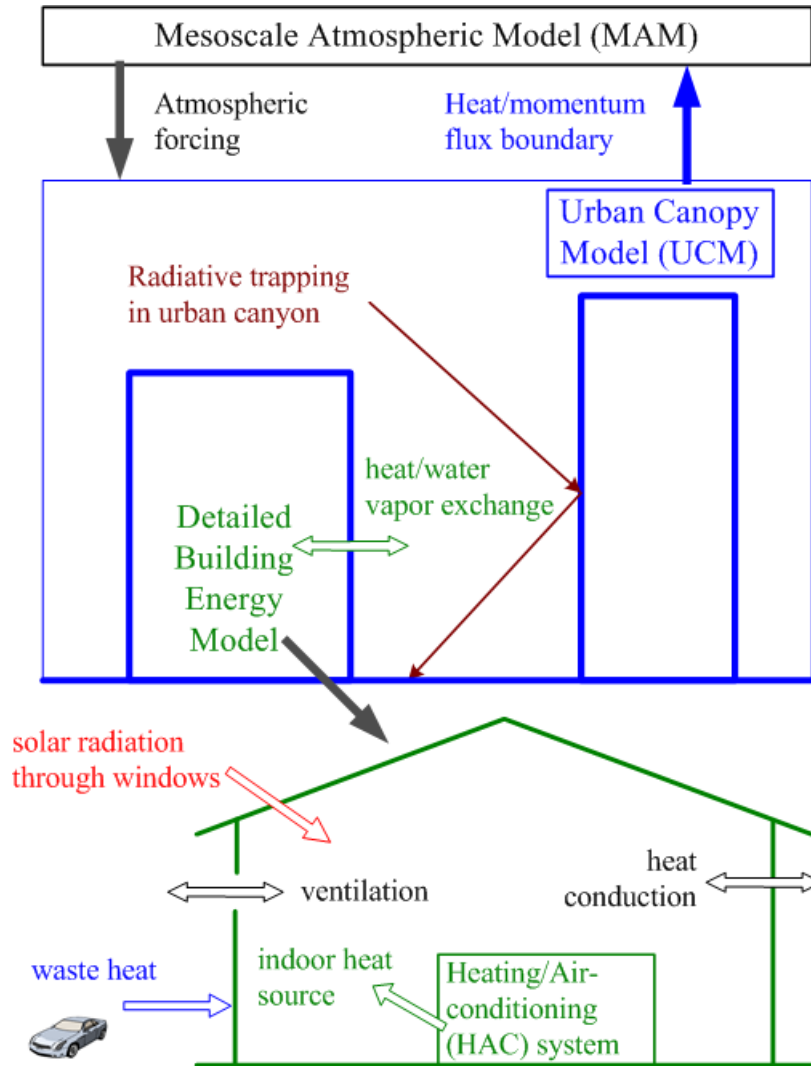

Figure 5.1: Schematic of numerical modeling in characterizing the effect of urbanization on land-atmosphere interactions through coupling of multi-scale models, including the building energy model, the urban canopy model and the mesoscale atmospheric model

The urban canopy model hitherto developed for surface exchange of energy and water is one piece of the jigsaw in a larger framework of multi-scale modeling (see Figure 5.1), which bridges the gap between the building energy model (BEM) and the mesoscale atmospheric model (MAM). Thanks to the rapidly increasing research effort devoted to UCM, including this one, we have a relatively robust tool to resolve the physics of flow and transport phenomena at the local (from neighborhood to city) scale for urban land-atmosphere interactions; whereas the building-resolving scale BEM is relatively under-developed. Resolving the physics occurring inside individual buildings requires more detailed parameterization schemes for capturing processes such as the compartment turbulent flow and the operation of heating, ventilation and air-conditioning (HVAC) systems. Despite its intensive computational costs, incorporation of BEM into UCM has apparent advantages to: (a) better quantify the building energy consumption through explicit modeling of the HVAC operation, heat conditions and interior radiation redistribution; and (b) to directly identify the anthropogenic impacts on the long-term urban sustainability, such as waste heat/water sources and emission and transport of pollutant across building enclosures.

Another perspective of future development of the current framework is to couple the UCM to numerical models of the atmospheric boundary layer (ABL) processes, in a one-dimensional setting. 1D ABL simulations including slab or column models assume horizontal homogeneity and resolve the vertical transport of heat and moisture, where the UCM prediction of surface fluxes serves as the lower boundary conditions.

It is also noteworthy that this dissertation has been focused on the surface exchange of scalars (energy and moisture) exclusively. Flow dynamics and transport of

111

momentum in urban canopies involve 3D wind components (vectors) and are not dealt in this study. Despite the proved applicability of UCM in capturing scalar transport, the current framework, including its multi-layer counterparts, with physically-based numerical parametrization schemes achieved little success in predicting flow patterns inside urban canopies. One apparent reason of this failure is due to the unpredictable nature of turbulent flow. In addition, in urban areas, modeling of the turbulent flow is further complicated by the presence of buildings (as bluff roughness elements) through wake interaction, distortion and enhancement, to a formidable degree. Modeling of the dynamics of flow over urban landcover and any process associated with the 3D wind vector, e.g. mixing and dispersion in street canyons, remains an important research challenges.

Appendix A: Implementation of spatially-analytical algorithm

Step 1: Starting from the Stieltjes integral in Eq. (2.12), $x \in [0, d]$, denote $\theta(x,t) = T(x,t) - T_0$, $\theta_1(t) = T(0,t) - T_0$ and $\theta_2(t) = T(d,t) - T_0$. Note that the subscripts '1' and '2' denote the surface indices: 1 for $x = 0$, and 2 for $x = d$. Also denote $F_x(t) = g_1(x,t)$, $F_1(t) = g_1(0,t)$, $F_2(t) = g_1(d,t)$. A plot of $F_x(t)$ for the case study in Sec 2.3.1, with dimensionless time and space variables, is shown in Figure A1. It is easy to obtain

$$\theta(x,t) = \int_0^t q_1(t - \tau) dF_x(\tau) - \int_0^t q_2(t - \tau) dF_{d-x}(\tau). \tag{A.1}$$

Here we used the reciprocal relation $g_1(x,t) = -g_2(d - x, t)$. In particular, we have

$$\theta_1(t) = \int_0^t q_1(t - \tau) dF_1(\tau) - \int_0^t q_2(t - \tau) dF_2(\tau), \tag{A.2}$$

and

$$\theta_2 = \int_0^t q_1(t - \tau) dF_2(\tau) - \int_0^t q_2(t - \tau) dF_1(\tau). \tag{A.3}$$

Step 2: Discretize the temporal interval of interest as $\{t_j = j\Delta t : j = 0,1,...,N\}$ where Δt is the sampling time and the solutions are to be computed at each time step t_j. For brevity, let $f(n) = f(t_n)$ be any time-varying function. Apply the trapezoidal rule to (A.1), at step n (data for all the previous steps from 1 to n-1 are known):

$$\theta(x,n) = \frac{1}{2} \sum_{j=1}^n [q_1(n - j + 1) + q_1(n - j)] \Delta F_1(j)$$
$$- \frac{1}{2} \sum_{j=1}^n [q_2(n - j + 1) + q_2(n - j)] \Delta F_2(j) \tag{A.4}$$

with

$$\Delta F_i(j) = F_i(j) - F_i(j-1), i = 1, 2; j = 1, ..., N; \qquad \Delta F_i(0) = F_i(0). \quad \text{(A.5)}$$

Rearranging (A.4), we can obtain

$$\theta(x,t) = 0.5\Delta F_x(0)q_1(n) + S_n(q_1, \Delta F_x) - 0.5\Delta F_{d-x}(0)q_2(n) - S_n(q_2, \Delta F_{d-x}), \text{(A.6)}$$

where $S_n(q, \Delta F)$, with generic arguments υ and ΔF, is defined as:

$$S_n(q, \Delta F) = \frac{1}{2}q(n-1)\Delta F(1) + \frac{1}{2}\sum_{j=2}^{n}[q(n-j+1) + q(n-j)]\Delta F(j) \quad \text{(A.7)}$$

and can be easily implemented using the trapezoidal numerical integration, e.g. function '*trapz*' in MatLab, using q and ΔF arrays from all the previous steps from 1 to $n-1$ and integrating in the convolutional manner.

Step 3: To evaluate (A.6), $q_1(n)$ and $q_2(n)$ need to be obtained from the boundary conditions (BC). For example, if the boundary conditions are specified as in Eqs. (2.21) to (2.22) (T1Q2, following the notation by Cole *et al.* (2011), i.e. with Neumann boundary at the exterior surface and Dirichlet boundary in the building interior), q_1 is prescribed by meteorological forcing. The flux at the other surface q_2, can be obtained by numerically solving (A.3) as

$$q_2(n) = \frac{F_2(0)q_1(n) + 2[S_n(q_1, \Delta F_2) - S_n(q_2, \Delta F_1)]}{F_1(0)} \quad \text{(A.8)}$$

It is noteworthy that the Stieltjes integral incorporating the non-homogeneous forcing has been derived for other combination of boundary conditions, following Duhamel's principle (Cole *et al.*, 2011), other than the one in Eq. (2.12) (i.e. with BC Q1Q2). We just illustrated that Eq. (2.12) can be used in a general framework of Duhamel's integral,

towards which IBVP with other BCs (like T1Q2) can be solved under this framework without re-deriving the mathematical results.
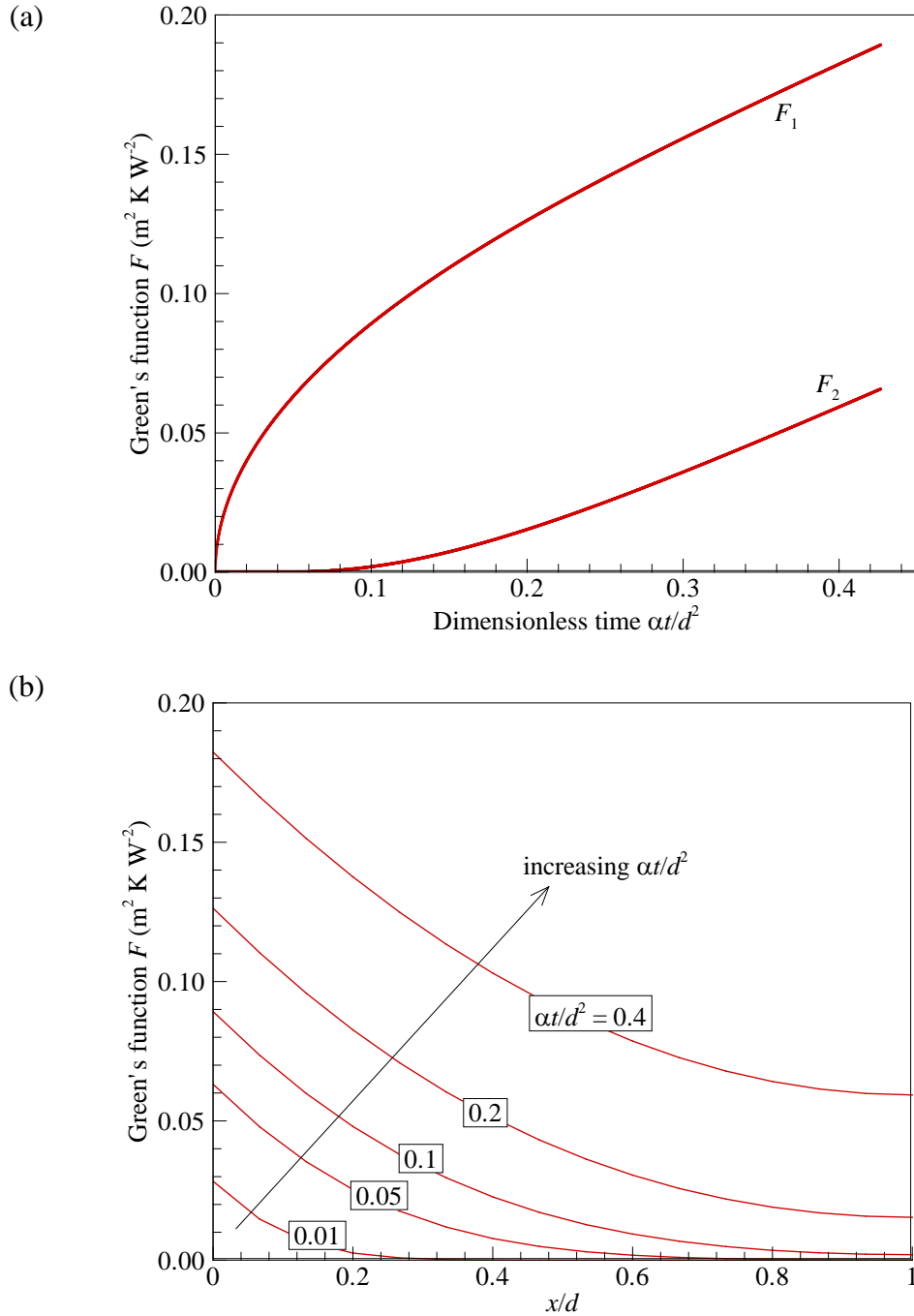

Figure A.1: Green's function solution for heat diffusion for a 1D wall: (a) F as a function of dimensionless time; (b) spatial variation of F

Appendix B: Closed-form formulas for aerodynamic resistance

The aerodynamic resistance is computed using Monin-Obukhov similarity theory, where the stability coefficients of Mascart *et al.* (1995) are adopted:

$$\text{RES}_R = \frac{C}{U_a a^2(z_R) F_h(z_R)}, \tag{B.1}$$

$$\text{RES}_{can} = \frac{C}{(U_a - U_{can}) a^2(z_R - z_T) F_h(z_R - z_T)}, \tag{B.2}$$

$$a^2(z) = \frac{\kappa^2}{\left[\ln(z/z_{0m})\right]^2}, \tag{B.3}$$

$$F_h(z) = \frac{\ln(z/z_{0m})}{\ln(z/z_{0h})} \times \begin{cases} \left(1 - \dfrac{b\text{Ri}_b}{1 + C_h\sqrt{\text{Ri}_b}}\right) & \text{if } \text{Ri}_b \leq 0 \\[2ex] \dfrac{1}{1 + b'\text{Ri}_b} & \text{if } \text{Ri}_b > 0 \end{cases}, \tag{B.4}$$

$$\mu = \ln(z_{0m}/z_{0h}), \tag{B.5}$$

$$C_h^* = 3.2165 + 4.3431\mu + 0.536\mu^2 - 0.0781\mu^3, \tag{B.6}$$

$$\mu = \ln(z_{0m}/z_{0h}), \tag{B.7}$$

$$p_h = 0.5802 - 0.1571\mu + 0.0327\mu^2 - 0.0026\mu^3, \tag{B.8}$$

$$C_h = a^2 b \frac{\ln(z/z_{0m})}{\ln(z/z_{0h})} C_h^* \left(\frac{z}{z_{0h}}\right)^{p_h}, \tag{B.9}$$

where κ is the Von Karman constant, $C = 0.74$, $b = 9.4$, $b' = 9.4$, and Ri_b is the bulk Richard number defined by

$$\text{Ri}_b(z) = \frac{gz\Delta T}{\bar{T}U^2(z)}. \tag{B.10}$$

References

[1]. Abahri, K., R. Belarbi, and A. Trabelsi (2011), Contribution to analytical and numerical study of combined heat and moisture transfer in porous building materials, *Build. Environ.*, *46*, 1354-1360.

[2]. Abu-Hamdeh, N. H., and R. C. Reeder (2000), Soil thermal conductivity: Effects of density, moisture, salt concentration, and organic matter, *Soil Sci. Soc. Am. J.*, *64*(4), 1285-1290.

[3]. Anandakumar, K. (1999), A study on the partition of net radiation into heat fluxes on a dry asphalt surface, *Atmos. Environ.*, *33*(24-25), 3911-3918.

[4]. Andersen, C. T., I. D. L. Foster, and C. J. Pratt (1999), The role of urban surfaces (permeable pavements) in regulating drainage and evaporation: Development of a laboratory simulation experiment, *Hydrol. Process.*, *13*(4), 597-609.

[5]. Arnfield, A. J. (2003), Two decades of urban climate research: A review of turbulence, exchanges of energy and water, and the urban heat island, *Int. J. Climatol.*, *23*(1), 1-26.

[6]. Arya, S. P. (2001), *Introduction to micrometeorology, 2nd ed.*, 420 pp., Academic Press, San Diego.

[7]. ASHRAE (2009), Chapter 26: Heat, air, and moisture control in building assemblies - material properties, in *ASHRAE handbook: fundamentals*, edited by M. S. Owen, pp. 26.21-26.22, American Society of Heating, Refrigerating and Air-Conditioning Engineers, Inc., Atlanta.

[8]. Au, S. K., and J. L. Beck (2001), Estimation of small failure probabilities in high dimensions by subset simulation, *Probab. Eng. Mech.*, *16*(4), 263-277.

[9]. Au, S. K., Z. H. Wang, and S. M. Lo (2007), Compartment fire risk analysis by advanced Monte Carlo simulation, *Eng. Struct.*, *29*(9), 2381-2390.

[10]. Baklanov, A., P. G. Mestayer, A. Clappier, S. Zilitinkevich, S. Joffre, A. Mahura, and N. W. Nielsen (2008), Towards improving the simulation of meteorological fields in urban areas through updated/advanced surface fluxes description, *Atmos. Chem. Phys.*, *8*(3), 523-543.

[11]. Berdient, P. B., and W. C. Huber (1992), *Hydrology and floodplain analysis*, second ed., 692 pp., Addison-Wesley, Reading.

[12]. Best, M. J. (1998), A model to predict surface temperatures, *Boundary-Layer Meteorol.*, *88*(2), 279-306.

[13]. Bettencourt, L., and G. West (2010), A unified theory of urban living, *Nature*, *467*(7318), 912-913.

[14]. Bhumralkar, C. M. (1975), Numerical experiments on computation of ground surface temperature in an atmospheric general circulation model, *J. Appl. Meteorol.*, *14*(7), 1246-1258.

[15]. Borselli, L., and D. Torri (2010), Soil roughness, slope and surface storage relationship for impervious areas, *J. Hydrol.*, *393*(3-4), 389-400.

[16]. Bou-Zeid, E., J. Overney, B. D. Rogers, and M. B. Parlange (2009), The effects of building representation and clustering in large-eddy simulations of flows in urban canopies, *Boundary-Layer Meteorol.*, *132*(3), 415-436.

[17]. Brown, M. J., and M. D. Williams (1998), An urban canopy parameterization for mesoscale meteorological models, in *AMS 2nd Urban Environment Symposium*, pp. 144-147, Albuquerque, NM.

[18]. Brutsaert, W. (2005), *Hydrology - An introduction*, 605 pp., Cambridge Press, New York.

[19]. Campbell, G. S., C. Calissendorff, and J. H. Williams (1991), Probe for measuring soil specific heat using a heat-pulse method, *Soil Sci. Soc. Am. J.*, *55*(1), 291-293.

[20]. Carslaw, H. S., and J. C. Jaeger (1959), *Conduction of heat in solids*, second ed., 510 pp., Oxford University Press, Oxford.

[21]. Champollion, C., P. Drobinski, M. Haeffelin, O. Bock, J. Tarniewicz, M. N. Bouin, and R. Vautard (2009), Water vapour variability induced by urban/rural surface heterogeneities during convective conditions, *Q. J. R. Meteorol. Soc.*, *135*(642), 1266-1276.

[22]. Chen, F., and J. Dudhia (2001), Coupling an advanced land surface-hydrology model with the Penn State-NCAR MM5 modeling system. Part I: Model implementation and sensitivity, *Mon. Weather Rev.*, *129*(4), 569-585.

[23]. Chen, F., H. Kusaka, R. Bornstein, J. Ching, C. S. B. Grimmond, S. Grossman-Clarke, T. Loridan, K. W. Manning, A. Martilli, S. Miao, D. Sailor, F. Salamanca, H. Taha, M. Tewari, X. M. Wang, A. Wyszogrodzki, and C. Zhang (2011), The integrated WRF/Urban modeling system: development, evaluation, and applications to urban environmental problems, *Int. J. Climatol.*, *31*, 273-288.

[24]. Chen, F., K. Mitchell, J. Schaake, Y. K. Xue, H. L. Pan, V. Koren, Q. Y. Duan, M. Ek, and A. Betts (1996), Modeling of land surface evaporation by four schemes and comparison with FIFE observations, *J. Geophys. Res.-Atmos.*, *101*(D3), 7251-7268.

[25]. Clapp, R. B., and G. M. Hornberger (1978), Empirical equations for some soil hydraulic properties, *Water Resour. Res.*, *14*(4), 601-604.

[26]. Coceal, O., T. G. Thomas, I. P. Castro, and S. E. Belcher (2006), Mean flow and turbulence statistics over groups of urban-like cubical obstacles, *Boundary-Layer Meteorol.*, *121*(3), 491-519.

[27]. Cole, K. D., A. Haji-Sheikh, J. V. Beck, and B. Litkouhi (2011), *Heat conduction using Green's functions, second edition*, 643 pp., Taylor & Francis, Boca Raton.

[28]. Corby, G. A., A. Gilchrist, and R. L. Newson (1972), A general circulation model of the atmosphere suitable for long period of integrations, *Q. J. R. Meteorol. Soc.*, *98*(418), 809-832.

[29]. Cosby, B. J., G. M. Hornberger, R. B. Clapp, and T. R. Ginn (1984), A statistical exploration of the relationships of soil moisture characteristic to the physical properties of soils, *Water Resour. Res.*, *20*(6), 682-690.

[30]. Courant, R., and D. Hilbert (1989), *Methods of mathematical physics: partial differential equations, Vol II*, 856 pp., Wiley, New York.

[31]. Cuenca, R. H., M. Ek, and L. Mahrt (1996), Impact of soil water property parameterization on atmospheric boundary layer simulation, *J. Geophys. Res.-Atmos.*, *101*(D3), 7269-7277.

[32]. De Bruin, H. A. R., and A. A. M. Holtslag (1982), A simple parameterization of the surface fluxes of sensible and latent heat during daytime compared with the Penman-Monteith concept, *J. Appl. Meteorol.*, *21*(11), 1610-1621.

[33]. Deardorff, J. W. (1978), Efficient prediction of ground surface temperature and moisture, with inclusion of a layer of vegetation, *J. Geophys. Res.*, *83*, 1889-1903.

[34]. Defraeye, T., B. Blocken, and J. Carmeliet (2010), CFD analysis of convective heat transfer at the surfaces of a cube immersed in a turbulent boundary layer, *Int. J. Heat Mass Transfer*, *53*(1-3), 297-308.

[35]. Doll, D., J. K. S. Ching, and J. Kaneshiro (1985), Parameterization of subsurface heating for soil and concrete using net radiation data, *Boundary-Layer Meteorol.*, *32*(4), 351-372.

[36]. Dupont, S., and P. G. Mestayer (2006), Parameterization of the urban energy budget with the submesoscale soil model, *J. Appl. Meteorol. Climatol.*, *45*(12), 1744-1765.

[37].   Dupont, S., T. L. Otte, and J. K. S. Ching (2004), Simulation of meteorological fields within and above urban and rural canopies with a mesoscale model (MM5), *Boundary-Layer Meteorol.*, *113*(1), 111-158.

[38].   Fernando, H. J. S. (2010), Fluid dynamics of urban atmospheres in complex terrain, *Annu. Rev. Fluid Mech.*, *42*, 365-389.

[39].   Flagg, D. D., and P. A. Taylor (2011), Sensitivity of mesoscale model urban boundary layer meteorology to the scale of urban representation, *Atmos. Chem. Phys.*, *11*(6), 2951-2972.

[40].   Foken, T. (2008), The energy balance closure problem: An overview, *Ecol. Appl.*, *18*(6), 1351-1367.

[41].   Fortuniak, K. (2008), Numerical estimation of the effective albedo of an urban canyon, *Theor. Appl. Climatol.*, *91*(1-4), 245-258.

[42].   Grimmond, C. S. B., M. Blackett, M. J. Best, J. J. Baik, S. E. Belcher, J. Beringer, S. I. Bohnenstengel, I. Calmet, F. Chen, A. Coutts, A. Dandou, K. Fortuniak, M. L. Gouvea, R. Hamdi, M. Hendry, M. Kanda, T. Kawai, Y. Kawamoto, H. Kondo, E. S. Krayenhoff, S. H. Lee, T. Loridan, A. Martilli, V. Masson, S. Miao, K. Olesen, R. Ooka, G. Pigeon, A. Porson, Y. H. Ryu, F. Salamanca, G. J. Steeneveld, M. Tombrou, J. A. Voogt, D. T. Young, and N. Zhang (2011), Initial results from phase 2 of the international urban energy balance model comparison, *Int. J. Climatol.*, *31*, 244-272.

[43].   Grimmond, C. S. B., M. Blackett, M. J. Best, J. Barlow, J. J. Baik, S. E. Belcher, S. I. Bohnenstengel, I. Calmet, F. Chen, A. Dandou, K. Fortuniak, M. L. Gouvea,

R. Hamdi, M. Hendry, T. Kawai, Y. Kawamoto, H. Kondo, E. S. Krayenhoff, S. H. Lee, T. Loridan, A. Martilli, V. Masson, S. Miao, K. Oleson, G. Pigeon, A. Porson, Y. H. Ryu, F. Salamanca, L. Shashua-Bar, G. J. Steeneveld, M. Tombrou, J. Voogt, D. Young, and N. Zhang (2010), The international urban energy balance models comparison project: First results from phase 1, *J. Appl. Meteorol. Climatol.*, *49*(6), 1268-1292.

[44]. Grimmond, C. S. B., H. A. Cleugh, and T. R. Oke (1991), An objective urban heat storage model and its comparison with other schemes, *Atmos. Environ.*, *25*(3), 311-326.

[45]. Grimmond, C. S. B., and T. R. Oke (1999), Aerodynamic properties of urban areas derived from analysis of surface form, *J. Appl. Meteorol.*, *38*(9), 1262-1292.

[46]. Grimmond, C. S. B., and T. R. Oke (2002), Turbulent heat fluxes in urban areas: Observations and a local-scale urban meteorological parameterization scheme (LUMPS), *J. Appl. Meteorol.*, *41*(7), 792-810.

[47]. Grimmond, S. (2007), Urbanization and global environmental change: local effects of urban warming, *Geograph. J.*, *173*, 83-88.

[48]. Hagishima, A., J. Tanimoto, and K. Narita (2005), Intercomparisons of experimental convective heat transfer coefficients and mass transfer coefficients of urban surfaces, *Boundary-Layer Meteorol.*, *117*(3), 551-576.

[49]. Hamdi, R., and G. Schayes (2007), Validation of Martilli's urban boundary layer scheme with measurements from two mid-latitude European cities, *Atmos. Chem. Phys.*, *7*(17), 4513-4526.

[50]. Hamdi, R., P. Termonia, and P. Baguis (2010), Effects of urbanization and climate change on surface runoff of the Brussels capital region: a case study using an urban soil–vegetation–atmosphere-transfer model, *Int. J. Climatol.*, DOI: 10.1002/joc.2207.

[51]. Hanks, R. J. (1992), *Applied soil physics: soil water and temperature applications*, second ed., 176 pp., Springer-Verlag, New York.

[52]. Harman, I. N., and S. E. Belcher (2006), The surface energy balance and boundary layer over urban street canyons, *Q. J. R. Meteorol. Soc.*, *132*(621), 2749-2768.

[53]. Harman, I. N., M. J. Best, and S. E. Belcher (2004), Radiative exchange in an urban street canyon, *Boundary-Layer Meteorol.*, *110*(2), 301-316.

[54]. Hastings, W. K. (1970), Monte Carlo sampling methods using Markov chains and their applications, *Biometrika*, *57*(1), 97-109.

[55]. House-Peters, L. A., and H. Cheng (2011), Urban water demand modeling: review of concepts, methods, and organizing principles, *Water Resour. Res.*, *47*, W05401.

[56]. Johnson, G. T., T. R. Oke, T. J. Lyons, D. G. Steyn, I. D. Watson, and J. A. Voogt (1991), Simulation of surface urban heat islands under 'ideal' conditions at night, Part I: theory and tests against field data, *Boundary-Layer Meteorol.*, *56*(3), 275-294.

[57]. Kalnay, E., and M. Cai (2003), Impact of urbanization and land-use change on climate, *Nature*, *423*(6939), 528-531.

[58]. Kanda, M. (2007), Progress in urban meteorology: A review, *J. Meteorol. Soc. Japan*, *85B*, 363-383.

[59]. Kanda, M., T. Kawai, M. Kanega, R. Moriwaki, K. Narita, and A. Hagishima (2005), A simple energy balance model for regular building arrays, *Boundary-Layer Meteorol.*, *116*(3), 423-443.

[60]. Kasahara, A., and W. M. Washington (1971), General circulation experiments with a six-layer NCAR model, including orography, cloudiness and surface temperature calculations, *J. Atmos. Sci.*, *28*(5), 657-701.

[61]. Kondo, H., Y. Genchi, Y. Kikegawa, Y. Ohashi, H. Yoshikado, and H. Komiyama (2005), Development of a multi-layer urban canopy model for the analysis of energy consumption in a big city: Structure of the urban canopy model and its basic performance, *Boundary-Layer Meteorol.*, *116*(3), 395-421.

[62]. Krayenhoff, E. S., and J. A. Voogt (2007), A microscale three-dimensional urban energy balance model for studying surface temperatures, *Boundary-Layer Meteorol.*, *123*(3), 433-461.

[63]. Kusaka, H., and F. Kimura (2004), Coupling a single-layer urban canopy model with a simple atmospheric model: Impact on urban heat island simulation for an idealized case, *J. Meteorol. Soc. Japan*, *82*(1), 67-80.

[64]. Kusaka, H., H. Kondo, Y. Kikegawa, and F. Kimura (2001), A simple single-layer urban canopy model for atmospheric models: Comparison with multi-layer and slab models, *Boundary-Layer Meteorol.*, *101*(3), 329-358.

[65]. Lee, S. H. (2011), Further development of the vegetated urban canopy model including a grass-covered surface parameterization and photosynthesis effects, *Boundary-Layer Meteorol.*, *140*, 315-342.

[66]. Lee, S. H., and S. U. Park (2008), A vegetated urban canopy model for meteorological and environmental modelling, *Boundary-Layer Meteorol.*, *126*(1), 73-102.

[67]. Lemonsu, A., S. Belair, and J. Mailhot (2009), The new Canadian urban modelling system: evaluation for two cases from the joint urban 2003 Oklahoma city experiment, *Boundary-Layer Meteorol.*, *133*(1), 47-70.

[68]. Liebethal, C., B. Huwe, and T. Foken (2005), Sensitivity analysis for two ground heat flux calculation approaches, *Agric. Forest Meteorol.*, *132*(3-4), 253-262.

[69]. Liu, Y., J. N. Chen, W. Q. He, Q. Y. Tong, and W. F. Li (2010), Application of an uncertainty analysis approach to strategic environmental assessment for urban planning, *Environ. Sci. Technol.*, *44*(8), 3136-3141.

[70]. Loosvelt, L., V. R. N. Pauwels, W. M. Cornelis, G. J. M. De Lannoy, and N. E. C. Verhoest (2011), Impact of soil hydraulic parameter uncertainty on soil moisture modeling, *Water Resour. Res.*, *47*, W03505.

[71]. Loridan, T., C. S. B. Grimmond, S. Grossman-Clarke, F. Chen, M. Tewari, K. Manning, A. Martilli, H. Kusaka, and M. Best (2010), Trade-offs and responsiveness of the single-layer urban canopy parametrization in WRF: An offline evaluation using the MOSCEM optimization algorithm and field observations, *Q. J. R. Meteorol. Soc.*, *136*(649), 997-1019.

[72]. Martilli, A. (2007), Current research and future challenges in urban mesoscale modelling, *Int. J. Climatol.*, *27*(14), 1909-1918.

[73]. Martilli, A., A. Clappier, and M. W. Rotach (2002), An urban surface exchange parameterisation for mesoscale models, *Boundary-Layer Meteorol.*, *104*(2), 261-304.

[74]. Mascart, P., J. Noilhan, and H. Giordani (1995), A modified parameterization of flux-profile relationship in the surface layer using different roughness values for heat and momentum, *Boundary-Layer Meteorol.*, *72*(4), 331-344.

[75]. Masson, V. (2000), A physically-based scheme for the urban energy budget in atmospheric models, *Boundary-Layer Meteorol.*, *94*(3), 357-397.

[76]. Masson, V. (2006), Urban surface modeling and the meso-scale impact of cities, *Theor. Appl. Climatol.*, *84*(1-3), 35-45.

[77]. McCarthy, M. P., M. J. Best, and R. A. Betts (2010), Climate change in cities due to global warming and urban effects, *Geophys. Res. Lett.*, *37*, L09705.

[78]. Metropolis, N., A. W. Rosenbluth, M. N. Rosenbluth, A. H. Teller, and E. Teller (1953), Equations of state calculations by fast computing machines, *J. Chem. Phys.*, *21*(6), 1087-1092.

[79]. Mitchell, V. G., H. A. Cleugh, C. S. B. Grimmond, and J. Xu (2008), Linking urban water balance and energy balance models to analyse urban design options, *Hydrol. Process.*, *22*(16), 2891-2900.

[80]. Molders, N., and G. Kramm (2009), Permafrost modeling in weather forecasts and climate projections, in *New permafrost and glacier research*, edited by M. I. Krugger and H. P. Stern, pp. 51-88, Nova Science Publishers, Inc., New York.

[81]. Nadeau, D. F., W. Brutsaert, M. B. Parlange, E. Bou-Zeid, G. Barrenetxea, O. Couach, M. O. Boldi, J. S. Selker, and M. Vetterli (2009), Estimation of urban sensible heat flux using a dense wireless network of observations, *Environ. Fluid Mech.*, *9*(6), 635-653.

[82]. Nakayama, T., and T. Fujita (2010), Cooling effect of water-holding pavements made of new materials on water and heat budgets in urban areas, *Landscape Urban Plan.*, *96*, 57-67.

[83]. Niceno, B., A. D. T. Dronkers, and K. Hanjalic (2002), Turbulent heat transfer from a multi-layered wall-mounted cube matrix: a large eddy simulation, *Int. J. Heat Fluid Flow*, *23*(2), 173-185.

[84]. Nickerson, E. C., and V. E. Smiley (1975), Surface layer and energy budget parameterizations for mesoscale models, *J. Appl. Meteorol.*, *14*(3), 297-300.

[85]. Niyogi, D. S., and S. Raman (1997), Comparison of four different stomatal resistance schemes using FIFE observations, *J. Appl. Meteorol.*, *36*(7), 903-917.

[86]. Noilhan, J., and S. Planton (1989), A simple parameterization of land surface processes for meteorological models, *Mon. Weather Rev.*, *117*(3), 536-549.

[87]. Nunez, C. M., E. A. Varas, and F. J. Meza (2010), Modelling soil heat flux, *Theor. Appl. Climatol.*, *100*(3-4), 251-260.

[88]. Nunez, M., and T. R. Oke (1976), Long-wave radiative flux divergence and nocturnal cooling of the urban atmosphere, *Boundary-Layer Meteorol.*, *10*, 121-135.

[89]. Nunez, M., and T. R. Oke (1977), The energy balance of an urban canyon, *J. Appl. Meteorol.*, *16*(1), 11-19.

[90]. Oke, T. R. (1982), The energetic basis of the urban heat island, *Q. J. R. Meteorol. Soc.*, *108*(455), 1-24.

[91]. Oke, T. R., and H. A. Cleugh (1987), Urban heat storage derived as energy balance residuals, *Boundary-Layer Meteorol.*, *39*(3), 233-245.

[92]. Oke, T. R., G. T. Johnson, D. G. Steyn, and I. D. Watson (1991), Simulation of surface urban heat islands under ideal conditions at night, Part 2: diagnosis of causation, *Boundary-Layer Meteorol.*, *56*(4), 339-358.

[93]. Oleson, K. W., G. B. Bonan, and J. Feddema (2010), Effects of white roofs on urban temperature in a global climate model, *Geophys. Res. Lett.*, *37*, L03701.

[94]. Panofsky, H. A., and G. W. Brier (1958), *Some applications of statistics to meteorology*, 224 pp., The Pennsylvania University, University Park.

[95]. Pataki, D. E., C. G. Boone, T. S. Hogue, G. D. Jenerette, J. P. McFadden, and S. Pincetl (2011), Ecohydrology bearings-invited commentary socio-ecohydrology and the urban water challenge, *Ecohydrology*, *4*(2), 341-347.

[96]. Porson, A., I. N. Harman, S. I. Bohnenstengel, and S. E. Belcher (2009), How many facets are needed to represent the surface energy balance of an urban area?, *Boundary-Layer Meteorol.*, *132*(1), 107-128.

[97]. Refsgaard, J. C., J. P. van der Sluijs, A. L. Hojberg, and P. A. Vanrolleghem (2007), Uncertainty in the environmental modelling process - A framework and guidance, *Environ. Modell. Softw.*, *22*(11), 1543-1556.

[98]. Roache, P. J. (1998), *Fundamentals of computational fluid dynamics*, 648 pp., Hermosa, New Mexico.

[99]. Roberts, C., and G. Casella (1999), *Monte Carlo statistical methods*, 680 pp., Springer, New York.

[100]. Roberts, S. M., T. R. Oke, C. S. B. Grimmond, and J. A. Voogt (2006), Comparison of four methods to estimate urban heat storage, *J. Appl. Meteorol. Climatol.*, *45*(12), 1766-1781.

[101]. Salamanca, F., A. Krpo, A. Martilli, and A. Clappier (2010), A new building energy model coupled with an urban canopy parameterization for urban climate

simulations-part I. formulation, verification, and sensitivity analysis of the model, *Theor. Appl. Climatol.*, *99*(3-4), 331-344.

[102]. Santiago, J. L., and A. Martilli (2010), A dynamic urban canopy parameterization for mesoscale models based on computational fluid dynamics Reynolds-averaged Navier-Stokes microscale simulations, *Boundary-Layer Meteorol.*, *137*(3), 417-439.

[103]. Sailor, D. J. (2011), A review of methods for estimating anthropogenic heat and moisture emissions in the urban environment, *Int. J. Climatol.*, *31*(2), 189-199.

[104]. Sailor, D. J., and H. L. Fan (2002), Modeling the diurnal variability of effective albedo for cities, *Atmos. Environ.*, *36*(4), 713-725.

[105]. Schlunder, E. U. (1988), On the mechanism of the constant drying rate period and its relevance to diffusion controlled catalytic gas phase reactions, *Chem. Eng. Sci.*, *43*, 2685-2688.

[106]. Shokri, N., P. Lehmann, P. Vontobel, and D. Or (2008), Drying front and water content dynamics during evaporation from sand delineated by neutron radiography, *Water Resour. Res.*, *44*(6), W06418.

[107]. Strub, F., J. Castaing-Lasvignottes, M. Strub, M. Pons, and F. Monchoux (2005), Second law analysis of periodic heat conduction through a wall, *Int. J. Therm. Sci.*, *44*(12), 1154-1160.

[108]. Stull, R. B. (1988), *An introduction to boundary layer meteorology*, 670 pp., Kluwer Academic Publishers, Dordrecht, the Netherlands.

[109]. Taha, H. (1997), Urban climates and heat islands: Albedo, evapotranspiration, and anthropogenic heat, *Energy Build.*, *25*(2), 99-103.

[110]. van Genuchten, M. T. (1980), A closed-form equation for predicting the hydraulic conductivity of unsaturated soils, *Soil Sci. Soc. Am. J.*, *44*, 892-898.

[111]. Vercauteren, N., E. Bou-Zeid, H. Huwald, M. B. Parlange, and W. Brutsaert (2009), Estimation of wet surface evaporation from sensible heat flux measurements, *Water Resour. Res.*, *45*, W06424.

[112]. Wang, J., and R. L. Bras (1999), Ground heat flux estimated from surface soil temperature, *J. Hydrol.*, *216*(3-4), 214-226.

[113]. Wang, Z. H. (2010), Geometric effect of radiative heat exchange in concave structure with application to heating of steel I-sections in fire, *Int. J. Heat Mass Transfer*, *53*(5-6), 997-1003.

[114]. Wang, Z. H., S. K. Au, and K. H. Tan (2005), Heat transfer analysis using a Green's function approach for uniformly insulated steel members subjected to fire, *Eng. Struct.*, *27*(10), 1551-1562.

[115]. Wang, Z. H., and E. Bou-Zeid (2011), Comment on "Impact of wave phase difference between soil surface heat flux and soil surface temperature on soil surface energy balance closure" by Z. Gao, R. Horton, and H. P. Liu, *J. Geophys. Res.-Atmos.*, *116*, D08110.

[116]. Wang, Z. H., E. Bou-Zeid, and J. A. Smith (2010), Application of a sensor network to study the energy budget in urban canopies, in *15th Symposium on meteorological observation and instrumentation*, 8 pp, Atlanta.

[117]. Wang, Z. H., E. Bou-Zeid, and J. A. Smith (2011a), A spatially-analytical scheme for surface temperatures and conductive heat fluxes in urban canopy models, *Boundary-Layer Meteorol.*, *138*(2), 171-193.

[118]. Wang, Z. H., E. Bou-Zeid, S. K. Au, and J. A. Smith (2011b), Analyzing the sensitivity of WRF's single-layer urban canopy model to parameter uncertainty using advanced Monte Carlo simulation, *J. Appl. Meteorol. Climatol.*, in press.

[119]. Yaghoobian, N., J. Kleissl, and E. S. Krayenhoff (2010), Modeling the thermal effects of artificial turf on the urban environment, *J. Appl. Meteorol.*, *49*(3), 332-345.

[120]. Yamanaka, T., A. Takeda, and F. Sugita (1997), A modified surface-resistance approach for representing bare-soil evaporation: Wind tunnel experiments under various atmospheric conditions, *Water Resour. Res.*, *33*(9), 2117-2128.